

FINAL  
IN 34-CR  
247654

Final Report  
for  
NASA Contract NAS8-38862  
**An Experimental Study of Characteristic Combustion-Driven Flow For CFD  
Validation**

By

Robert J. Santoro

Propulsion Engineering Research Center  
and  
Department of Mechanical Engineering  
The Pennsylvania State University  
University Park, PA

~~CN31S  
TURNER 0/PUBLICATION  
MARSHALL SPACE FLIGHT CENTER  
HUNTSVILLE AL.  
DELETIONS OR CHANGES 544-4494  
RETURN ADDRESS CN31D  
2444  
Document Code: 2444~~

October, 1997



## Table of Contents

Abstract		iv
I	Introduction	1
II	Experimental Facility	3
	2.1 Cryogenic Combustion Laboratory	3
	2.2 Optically-Accessible Rocket Chamber	3
III	Gaseous Oxygen/Hydrogen Shear Coaxial Injector Studies	6
	3.1 Experimental Setup	6
	3.1.1 Injector Geometry	6
	3.1.2 Flow Conditions	7
	3.2 Experimental Diagnostic Techniques	8
	3.2.1 Planar Laser Induced Fluorescence	9
	3.2.2 Laser Doppler Velocimetry	14
	3.2.3 Planar Laser Light Scattering	16
	3.2.4 Raman Spectroscopy (Line)	18
	3.2.5 Injector Thermocouple Instrumentation	20
	3.3 Results and Discussion	21
	3.3.1 OH-Radical Results	22
	3.3.2 Injector Tip Temperature Results	29
	3.3.3 Velocity Field Results	30
	3.3.4 Mixing Studies	35
	3.3.5 Raman Spectroscopy Measurements	43
IV	Flame Holding Studies of Shear Coaxial Injectors	47
	4.1 Experimental Setup	47
	4.1.1 Injector geometry	47
	4.1.2 Flow Conditions	48
	4.1.3 Raman Spectroscopy (Planar)	49
	4.2 Results and Discussion	51
	4.2.1 Raman Spectroscopy	51
	4.2.2 Injector Tip Temperature Measurements	68
V	Injector Flowfield Characterization For Gas/Gas Injector Technology (GGIT) Program	72
	5.1 First Phase of Experimentation	73
	5.1.1 Experimental Setup	74

5.1.1.1	Flow Conditions	74
5.1.1.2	O-F-O Triplet Element	74
5.1.1.3	F-O-F Triplet Element	76
5.1.1.4	Swirl Coaxial Element	78
5.1.2	Experimental Diagnostics	82
5.1.2.1	Raman Spectroscopy (Line)	82
5.1.2.2	Injector Face Thermocouple Instrumentation	84
5.1.3	Results and Discussion	84
5.2	Second Phase of Experimentation	92
5.2.1	Experimental Setup	92
5.2.1.1	Flow Conditions	92
5.2.1.2	Shear Coaxial Elements	92
5.2.2	Raman Spectroscopy Setup	92
5.2.3	Results and Discussion	95
VI	Liquid Oxygen/Gaseous Hydrogen Shear Coaxial Injector Studies	97
6.1	Experimental Setup	99
6.1.1	Injector Geometry	99
6.1.2	Flow Conditions	99
6.2	Experimental Diagnostics	101
6.2.1	Drop Mie Scattering	101
6.2.2	Phase Doppler Interferometry	101
6.3	Results and Discussion	103
6.4	Summary	108
VII	References	109
VIII	Published Papers	113
IX	Meetings	115
X	Personnel	118
XI	Awards	119

## ABSTRACT

A series of uni-element rocket injector studies were completed to provide benchmark quality data needed to validate computational fluid dynamic models. A shear coaxial injector geometry was selected as the primary injector for study using gaseous hydrogen/gaseous oxygen and gaseous hydrogen/liquid oxygen propellants. Emphasis was placed on the use of non-intrusive diagnostic techniques to characterize the flowfields inside an optically-accessible rocket chamber. For the case of gaseous hydrogen/gaseous oxygen propellants, measurements of the velocity and species fields were obtained using laser velocimetry and Raman spectroscopy, respectively. Based on the species measurements, temperature field determinations were obtained assuming ideal gas behavior. Qualitative flame shape information was also obtained using laser-induced fluorescence excited from OH radicals and laser light scattering studies of aluminum oxide particle seeded combustions. These latter measurements also provided species concentration and propellant mixing information for comparison with the Raman spectroscopy measurements. The gaseous hydrogen/liquid oxygen propellant studies for the shear coaxial injector focused on breakup mechanisms associated with the liquid oxygen jet under sub-critical pressure conditions. Laser sheet illumination techniques were used to visualize the core region of the jet and a Phase Doppler Particle Analyzer was utilized for drop velocity, size and size distribution characterization.

As an extension of the shear coaxial injector investigation for gaseous hydrogen/gaseous oxygen propellants, a series of gas/gas injector studies were conducted in support of the X-33 Reusable Launch Vehicle program. For these studies, a Gas/Gas Injector Technology team was formed consisting of the Marshall Space Flight Center, the NASA Lewis Research Center, Rocketdyne and Penn State. Injector geometries studied under this task included shear and swirl coaxial configurations as well as an impinging jet injector. The major diagnostic technique employed in these studies was Raman spectroscopy which was used to evaluate the mixing characteristics of the various injectors.

The results of the gaseous hydrogen/gaseous oxygen propellant studies indicated that the shear coaxial geometry configuration was a relatively poor injector in terms of mixing. The oxygen core was observed to extend well downstream of the injector and a significant fraction of the mixing occurred in the near nozzle region where measurements were not possible to obtain. Chamber pressure measurements indicated high performance was achieved with  $c^*$

efficiencies typically exceeding 98%. Detailed velocity and species measurements were obtained to allow CFD model validation and this set of benchmark data represents the most comprehensive data set available to date. Comparison between the species concentration measurements obtained using laser light scattering data from particle seeded flows with those obtained from Raman spectroscopy were generally good. However, the Raman approach is considered to be the preferred technique as simultaneous hydrogen, oxygen and water species measurements can be obtained with this approach. A major success of the program was the development and refinement of the Raman measurement technique for application to rocket engines.

Studies conducted with the Gas/Gas Injector Technology team were also highly successful. For these studies injector face heat transfer was also monitored via a mounted thermocouple. The results of these studies showed that the shear coaxial injector had the most benign thermal environment as compared to the swirl and impinging jet injectors. However as noted above, the shear coaxial geometry was the least effective mixing element for the conditions investigated. The face heat transfer characteristics for the swirl injector were found to be a strong function of the swirl angle with increased heat transfer as the swirl angle was increased. These studies clearly showed that highly efficient gas/gas injector configurations could be designed in terms of propellant mixing and high performance. However, face heat cooling strategies will need to be addressed if robust, long lifetime injectors are to result.

The gaseous hydrogen/liquid oxygen studies for the shear coaxial injector indicated that the atomization process is highly unsteady and that only a small fraction of the liquid oxygen was present as spherical drops. The laser sheet imaging indicated that a substantial fraction of the liquid oxygen jet initially broke up into large liquid ligaments that subsequently fragmented to small drops and ligaments. For comparison, some studies of swirl coaxial injectors were also undertaken and indicated that a larger fraction of the liquid formed drops directly from the liquid sheet breakup that typifies swirl injectors. Both the shear and swirl coaxial injector studies provided useful baseline results from which to benchmark computational fluid dynamic models. Furthermore, these studies established a basis from which to assess future directions regarding the characterization of rocket injectors.

# I INTRODUCTION

The current development activities with respect to launch vehicle technology emphasize low cost, high performance, operable systems. All these objectives are significantly impacted by the propulsion system. A critical step in meeting the overall system cost and performance goals involves the ability to efficiently design injector elements that provide the desired performance, combustion stability, face heat transfer, combustion chamber wall compatibility and fabrication characteristics. A particularly promising approach to achieving more robust, cost effective design methodologies involves the development of Computational Fluid Dynamic (CFD) approaches that integrate the combustion, fluid mechanics and heat transfer elements of the problem into a single design tool. Achievement of such a CFD-based methodology will require a concurrent experimental research effort. This effort should aim to provide, in a coordinated manner, the timely development of data for validation of a CFD model using detailed measurements of reacting flows under conditions representative of a rocket engine environment.

This report presents the results of a recent program conducted at the Penn State Propulsion Engineering Research Center to provide a comprehensive benchmark data set suitable for validation of CFD codes. The injector selected for study was the shear coaxial injector that was investigated under uni-element conditions. Both gaseous hydrogen/gaseous oxygen and gas hydrogen/liquid oxygen propellants were studied. The work also emphasized the application and development of suitable diagnostic approaches for obtaining the required data under actual rocket engine conditions. Many of the measurements obtained, particularly those involving laser-based techniques, represent the first time such measurements have been obtained for rocket chamber conditions.

The approach adopted in addressing the development of benchmark data for rocket conditions was arrived at in close cooperation with the CFD modeling community. The rocket chamber geometry, measurements to be obtained and boundary conditions to be employed were distributed to a number of workers for comments and suggestions. This input, obtained before any testing began, was critical to the direction of the current program with respect to the chamber design and experimental conditions studied.

In the sections that follow the results of several studies are reported. The initial work emphasized gaseous propellants and comprises the most extensive set of data obtained during this contract. Studies of gas/liquid propellants were also undertaken and are discussed in terms

of the atomization mechanism and drop size field observed for the shear coaxial injector. In the latter stages of the program interest in gas/gas injectors with respect to the Reusable Launch Vehicle (RLV) required that the program be realigned to directly investigate concepts of potential importance to this program. As a result, a coordinated group of researchers from the NASA Marshall Space Flight Center, NASA Lewis Research Center, Rocketdyne and Penn State were asked to form a Gas Gas Injector Technology team. An intensive series of studies was undertaken by this group in support of the full-flow staged-combustion cycle under development at Rocketdyne. From that work a series of gas/gas injectors was designed and tested. Some of the injector designs were proprietary to Rocketdyne, however, a series of "team" injectors was also considered. The results of those tests are contained in this report.

The results of the studies have been reported in journals and conferences periodically during the course of the program. All of that material is presented in this report. The remainder of the report is divided into a series of topical chapters dealing with the major elements of the program and the significant results obtained.

## **II EXPERIMENTAL FACILITY**

All rocket chamber combustion experiments were carried out at Penn State's Cryogenic Combustion Laboratory (CCL). This laboratory was created in 1989 to be the flagship facility for Penn State's Propulsion Engineering Research Center (PERC). In this section, the capabilities of the CCL are discussed first. This is followed by a description of the optically-accessible chamber that was used for the uni-element rocket flowfield characterization experiments.

### **2.1 CRYOGENIC COMBUSTION LABORATORY**

The CCL is a unique university facility where researchers conduct work on representative rocket flowfields. The laboratory is designed based on a similar test cell at NASA Lewis Research Center. The CCL, a remotely controlled laboratory, features a control room, diagnostic room and the test cell. The test cell where the combustion experiment is housed is isolated from the control and diagnostic rooms with reinforced concrete walls. For experimentation, the test cell's garage door is fully opened and the ventilation turned on to prevent the possible buildup of combustible materials. The diagnostic room located adjacent to the test cell is utilized for situating all the laser-based diagnostics. Optical ports between the diagnostics room and the test cell provide access into the test cell. The control room houses the computer control system that is used for timing the rocket firing. Video cameras with pan features enable remote visualizations of the test room. The operation of the entire system is designed with two levels of safety.

The CCL was initially operable for gaseous oxygen/hydrogen propellants. Liquid oxygen capability was initiated within a year of the laboratory's operation. Liquid hydrocarbon capability was brought on-line three years later. Finally airflow capability was brought on-line in early 1997. The propellant flowrate capabilities are tabulated Table 2.1.

### **2.2 OPTICALLY-ACCESSIBLE ROCKET CHAMBER**

The injector flowfield characterization experiments reported here were conducted using the optically accessible rocket chamber at Penn State's Cryogenic Combustion Laboratory. The rocket chamber used was designed in a modular fashion to easily provide optical access along the chamber length. A cross-sectional view of the rocket assembly is shown Fig. 2.1. The rocket chamber is comprised of several sections that include an injector assembly, igniter, window and

**Table 2.1. Flowrate Capabilities of Cryogenic Combustion Laboratory**

<b>Propellant</b>	<b>Maximum Flowrate (lbm/s)</b>
Gaseous Oxygen (GO <sub>2</sub> )	1
Gaseous Hydrogen (GH <sub>2</sub> )	0.25
Liquid Oxygen (LO <sub>2</sub> )	1
Liquid Hydrocarbon	0.5
Air	4 (can be upgraded to 16)

blank sections, and a nozzle assembly. These sections are held together by a hydraulic jack which allows for ease of assembly and arrangement of the various sections. The chamber length is varied by inserting or removing blank sections.

The modular design of the rocket chamber allows the testing of various injector geometries/propellant combinations up to a maximum chamber pressure of approximately 1000 psia. The injector assembly shown in Fig. 2.1 is for the shear coaxial element. However, the injector assembly can be easily configured to test various injector geometries. To date, shear coaxial, swirl coaxial, impinging jet, pintle, effervescent and triaxial injector elements have been tested in this chamber.

The igniter section of the rocket chamber consists of an ignition chamber (assembly shown on top of rocket chamber in Fig. 2.1) which utilizes a spark-ignited gaseous hydrogen/oxygen mixture to provide an ignition torch in the main combustion chamber. The window-section allows optical access into the combustion chamber for laser-based diagnostic techniques. As illustrated in Fig. 2.1, this section can be placed anywhere along the chamber length by interchanging it with other sections. Two diametrically opposed windows, 50.8 mm (2 in.) in diameter and 25.4 mm (1 in.) thick, provide optical access into the 50.8 mm (2 in.) square rocket chamber. Two slot windows measuring 6.25 x 50.8 mm (0.25 x 2 in.) on the remaining two sides provide additional optical access into the rocket chamber for laser sheet diagnostics. All windows are protected from the hot combustion gases by a gaseous nitrogen (GN<sub>2</sub>) curtain purge which flows across each of the interior window surfaces. Lastly, the water-cooled nozzle assembly is also modular in design. Nozzles of different throat diameters can be interchanged, thus providing the capability for varying the chamber pressure for the same propellant flow rate.

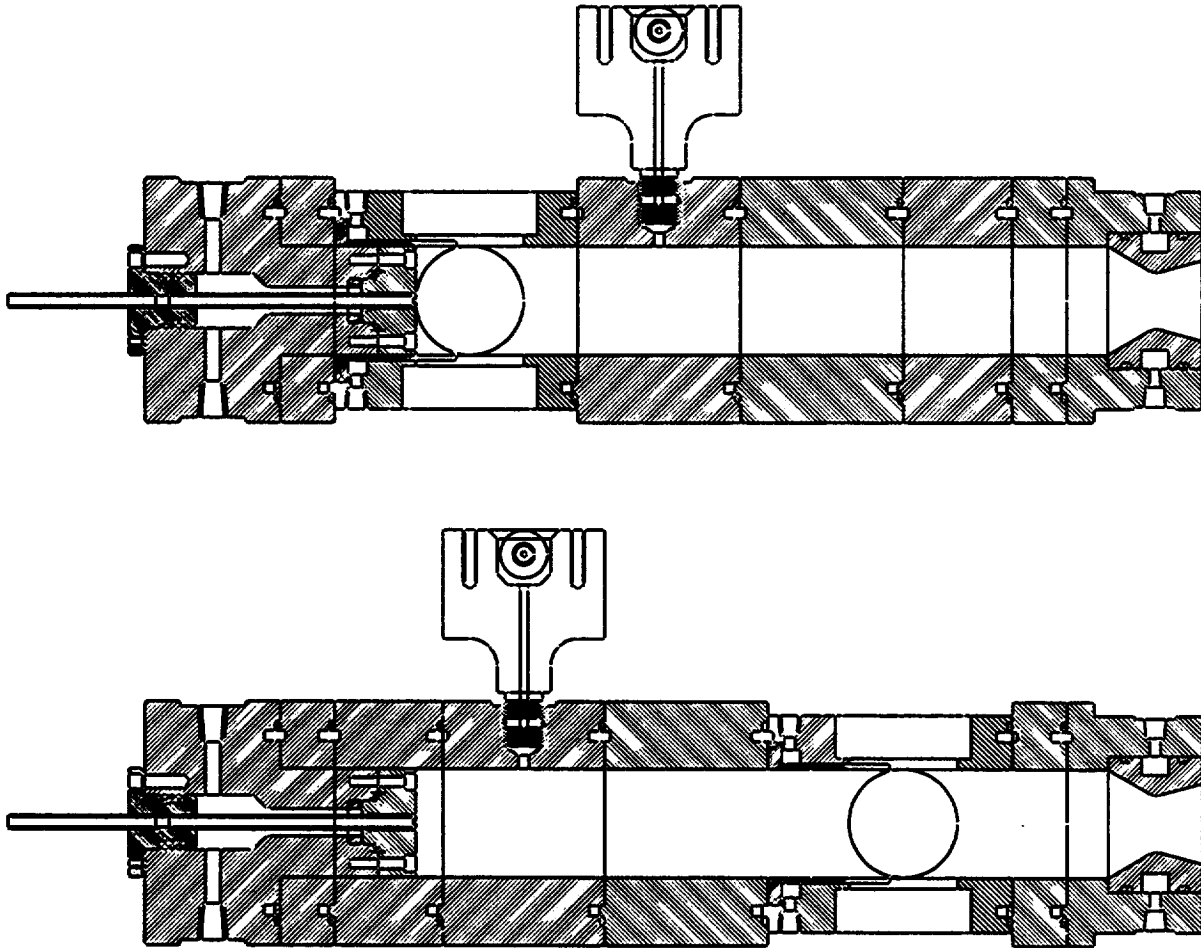


**Fig. 2.1. Schematic of the optically-accessible rocket chamber. The chamber is designed such that optical access can be gained for any axial location by interchanging sections. Two configurations illustrating this feature are shown in the figure.**

The time duration of a rocket test firing is typically set between two to four seconds depending on the target propellant flowrate, mixture ratio and chamber pressure. This run time represents a compromise between quartz window/chamber wall survivability and the time required for steady-state chamber pressure to be reached.

## **III GASEOUS OXYGEN/HYDROGEN SHEAR COAXIAL INJECTOR STUDIES**

The goal of this contract with NASA Marshall was to provide benchmark quality results for injector flowfields that could then be used for validating computational fluid dynamic codes. Early on in the program, the decision was made to first benchmark the flowfield for the simplest injector geometry and propellant combination. Here, “simplicity” was defined as a representative rocket injector flowfield with tractable fluid mechanics and chemistry in terms of both diagnostic application and CFD code verification. Inspection of various rocket propellant combinations and injector geometries in concert with current and future rocket applications clearly indicated that the gaseous oxygen/hydrogen shear coaxial injector outweighed all other combinations. The gaseous oxygen/hydrogen shear coaxial injector is “simple” because the flowfield is axisymmetric and the chemistry only includes  $O_2$ ,  $H_2$  and  $H_2O$  as major species. Based on these arguments, the initial thrust of the research was directed towards mapping the combusting gaseous oxygen/hydrogen flowfield downstream of a shear coaxial injector.

A laboratory scale shear coaxial injector element was designed for the rocket chamber described in the last chapter. In this section, the details of the injector geometry and experimental flow conditions are discussed first. This is followed by a description of the various diagnostic techniques utilized for characterizing the flowfield. Finally, the experimental results are presented and discussed.

### **3.1 EXPERIMENTAL SETUP**

In this section, the shear coaxial injector geometry and flow conditions are described. Details regarding the optically-accessible rocket chamber can be found in the previous chapter (see section 2.2).

#### **3.1.1 Injector Geometry**

The shear coaxial injector, shown in Fig. 3.1, was used for introducing the propellants into the rocket chamber. The  $GO_2$  post of the injector had an inner diameter of 7.75 mm (0.305 in.) and was not recessed with respect to the injector face. Two geometries were used for the fuel annulus to vary the mean injection velocity for the same  $GH_2$  mass flow rate. The inner diameters of both fuel annuli were 9.53 mm (0.375 in.), whereas the outer diameters of the fuel

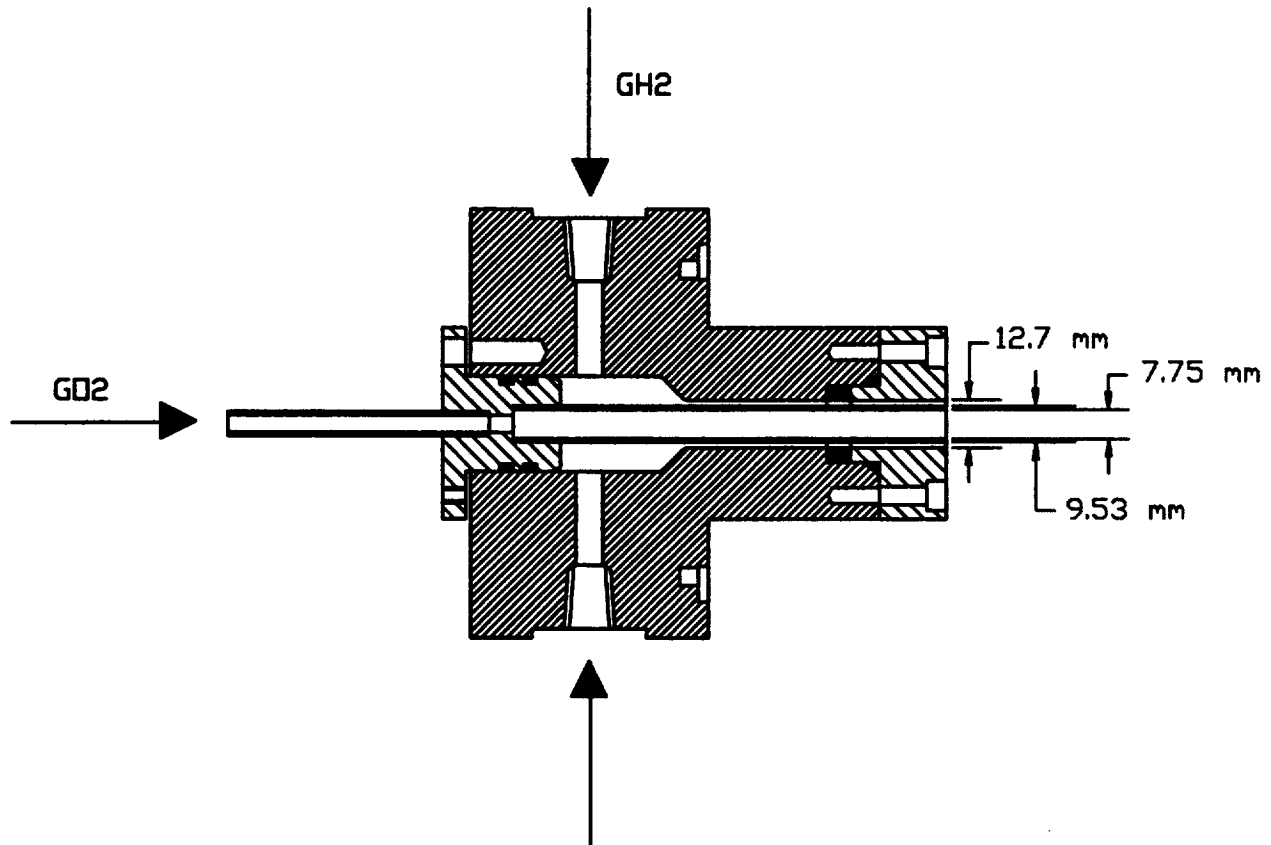


**Fig. 3.1. Schematic of the shear coaxial injector.**

annuli were 12.7 mm (0.5 in.) and 10.74 mm (0.423 in.). Note that in Fig. 3.1, the dimensions for the first injector are shown.

### 3.1.2 Flow Conditions

The injector flow conditions for the two test cases reported here are summarized in Table 3.1. The nominal mass flow rate of  $\text{GH}_2$  through the annulus of the shear coaxial injector was 0.011 kg/s (0.025 lbm/s) whereas the  $\text{GO}_2$  mass flow rate through the central tube of the injector was 0.045 kg/s (0.1 lbm/s) resulting in an O/F mass flow rate ratio of four. These flow rates together with the nozzle configuration produced a chamber pressure of 1.31 MPa (190 psia). The fuel annulus area for the two injectors tested was different and hence the fuel injection velocities differ, as shown in Table 3.1.

The  $c^*$  efficiency of the rocket firings is also presented in Table 3.1. The theoretical chamber pressure for complete combustion was calculated with the Combustion Equilibrium Calculation (CEC) [1] program (same for Cases 1 and 2). The calculations were done for two conditions, one which included the  $\text{GN}_2$  window purge flow and the other that neglected the

**Table 3.1. Rocket Chamber Conditions**

	Case 1*	Case 2**
GH <sub>2</sub> Mass Flow Rate	0.011 kg/s (0.025 lbm/s)	0.011 kg/s (0.025 lbm/s)
GO <sub>2</sub> Mass Flow Rate	0.045 kg/s (0.1 lbm/s)	0.045 kg/s (0.1 lbm/s)
GO <sub>2</sub> /GH <sub>2</sub> Mass Flow Ratio	4	4
GN <sub>2</sub> Mass Flow Rate (Purge)	0.01 kg/s (0.022 lbm/s)	0.01 kg/s (0.022 lbm/s)
GH <sub>2</sub> Injector Velocity	177 m/s (581 ft/s)	506 m/s (1660 ft/s)
GO <sub>2</sub> Injector Velocity	51 m/s (167 ft/s)	51 m/s (167 m/s)
GO <sub>2</sub> /GH <sub>2</sub> Velocity Ratio	0.29	0.10
Inlet Gas Temperature	294 K	294 K
Post Area (GO <sub>2</sub> )	47.14 mm <sup>2</sup> (0.073 in <sup>2</sup> )	47.14 mm <sup>2</sup> (0.073 in <sup>2</sup> )
Annulus Area (GH <sub>2</sub> )	55.42 mm <sup>2</sup> (0.086 in <sup>2</sup> )	19.41 mm <sup>2</sup> (0.030 in <sup>2</sup> )
Chamber Pressure	1.31 MPa (190 psia)	1.31 MPa (190 psia)
c* Efficiency (with GN <sub>2</sub> purge)	0.89	0.89
c* Efficiency (without GN <sub>2</sub> purge)	0.98	0.98

\* Velocity, major species field quantified

\*\* OH-radical region quantified

purge flow. The ratio of the measured chamber pressure to the calculated theoretical pressure for each case yielded the two tabulated  $c^*$  efficiencies. It was observed that by including the GN<sub>2</sub> purge flow in the combustion equilibrium calculation, the  $c^*$  efficiency decreased from 98% to 89%. However, a rocket test firing with the GN<sub>2</sub> window purge gas turned off yielded the same chamber pressure as shown in Table 3.1. This indicates that the  $c^*$  efficiency of the rocket was closer to 98%. The GN<sub>2</sub> window purge flow probably does not mix entirely with the combustion gases and therefore exits the nozzle at a colder temperature, thus explaining the lack of change in chamber pressure with and without the purge flow.

### 3.2 EXPERIMENTAL DIAGNOSTIC TECHNIQUES

Various laser-based diagnostic techniques were used to map the fluid dynamic/combustion characteristics of the shear coaxial flowfield. The majority of the diagnostic techniques were applied to map the flowfield corresponding to Case 1 in Table 3.1. The flame structure was first interrogated using planar laser induced fluorescence for OH

radicals. Since the OH radical is a marker of the combustion zone, these qualitative measurements provided valuable information regarding the high Reynolds number turbulent diffusion flame. These first experiments were conducted for the flow conditions corresponding to Case 2, Table 3.1. Initial attempts at velocity measurements using laser Doppler velocimetry (LDV) for the flow conditions of Case 2 indicated that the high velocity shear flow region between the GH<sub>2</sub> and the GO<sub>2</sub> could not be quantified because of spatial resolution and velocity range limitations. Based on the results of these attempts, the GH<sub>2</sub> annulus passage area was increased for the same propellant mass flow conditions, thereby decreasing both the GH<sub>2</sub> injection velocity and the need for improved spatial resolution. In summary, LDV was successfully implemented for characterizing the velocity field corresponding to the flow conditions of Case 1. Successive measurements were then only applied to the flow conditions of Case 1. The next technique, planar laser light scattering, was then applied to provide an initial picture of the mixing characteristics of the GH<sub>2</sub> and GO<sub>2</sub> streams in the near-injector tip region. These measurements were conducted for Case 1 to be consistent with the velocity field measurements. Raman spectroscopy was then applied in a “line” mode to quantify the major species (H<sub>2</sub>, O<sub>2</sub> and H<sub>2</sub>O) concentrations in the flowfield. It is noteworthy that the application of this technique was continuously refined and optimized during the course of this program. Hence, in this document, various configurations for this technique are noted. Clearly, the development of the Raman technique for making quantitative measurements in the harsh rocket flowfield conditions is a major contribution of this program. Also, measurements of the temperature of the injector tip were made using thermocouples to provide a boundary condition for CFD model input.

The implementation of the aforementioned diagnostic techniques is discussed in the following sub-sections.

### **3.2.1 Planar Laser Induced Fluorescence**

Laser induced fluorescence (LIF) measurements of hydroxyl radical (OH) were obtained at several axial locations downstream of the injector face for the injector geometry and flow rates summarized in Table 3.1, Case 2. One- and two-dimensional LIF images were obtained using the experimental setup shown in Fig. 3.2. A frequency doubled Nd-Yag pulse laser ( $\lambda=532$  nm) was used to pump a dye laser utilizing Rhodamine 590 laser dye to produce a tunable laser beam

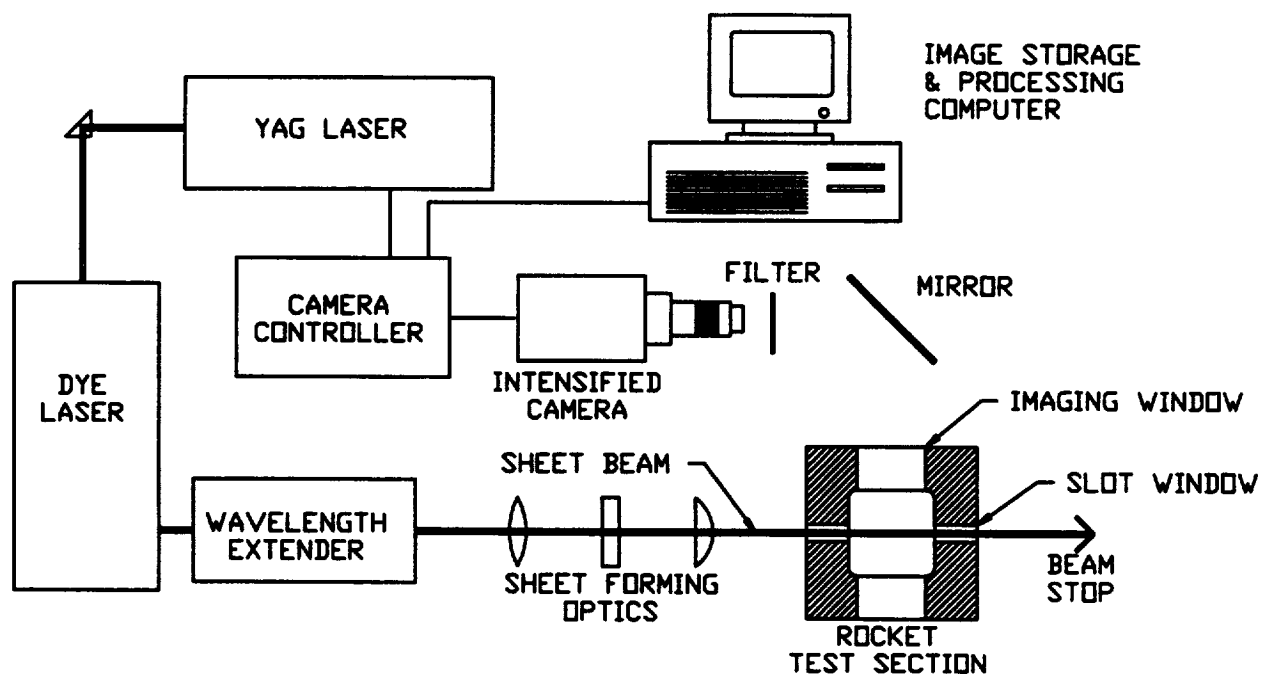


**Fig. 3.2 Planar laser induced fluorescence (PLIF) setup for measuring OH-radical fluorescence in the uni-element rocket chamber. The OH-radical fluorescence is detected by a cooled array intensified camera.**

with wavelengths between 542 to 607 nm. The output of the dye laser was then frequency doubled to yield a ultraviolet (UV) laser beam. The laser system produced laser pulses of ~2 mJ/pulse at a repetition rate of 10 Hz with a pulse duration of 7 ns. Wavelengths between 284.0 and 286.5 nm were used to excite the  $A^2S^+$  state of the OH-radical through absorption by various rotational lines of the (1,0) vibrational band.

Prior to the rocket experiments, the laser system was tuned to the particular OH-radical absorption line of interest using a propane fueled bunsen burner flame. A portion the laser beam was diverted from the primary beam and focused into the hot combustion gases at the tip of the propane flame. The OH-radical fluorescence from the flame was imaged at  $90^\circ$  to the laser beam onto a photo-multiplier tube. The wavelength of interest was then tuned by maximizing the photomultiplier output.

For the two-dimensional LIF images, the laser beam was formed into a sheet 100 mm (3.94 in.) in height and 0.75 mm (0.03 in.) in thickness using a combination of cylindrical ( $f_l=250$  mm) and spherical ( $f_l=1000$  mm) lenses. For the one-dimensional LIF measurements, the laser beam was focused with a 1000 mm spherical lens. The laser beam or sheet was introduced into the rocket chamber through the quartz slot windows.

The resulting OH-radical fluorescence perpendicular to the laser sheet/beam was imaged through one of the 50.8 mm diameter quartz windows. A Nikon 105 mm UV-Nikkor f4.5 lens was used to image the OH-radical fluorescence onto a Princeton Instruments cooled array intensified CCD camera. To reduce the interference from elastically scattered laser light, a WG-305 high pass filter was placed in front of the camera lens. This filter transmitted light with wavelengths greater than 300 nm, thus reducing the elastically scattered light while allowing the collection of the fluorescence from the radiative transitions from the (1,1) band of OH near 315 nm and the collisionally populated (0,0) band near 308 nm. In addition, a UG-11 bandpass filter (full width at half maximum ~275 to 380 nm) was used to reduce interference from flame luminosity. To further reduce the background light, the intensifier was gated on for approximately 20 ns .

Initial experiments showed that, even when the intensifier was gated off, a significant amount of light from the luminous flame was detected during the image readout time, thus producing a smeared image of the flame along with the OH-radical fluorescence image. This effect, which amounted to 10-20% of the peak fluorescence signal, was due to both the slightly degraded UV light rejection ability of the intensifier tube and the intense UV emission from the flame. A mechanical shutter with a minimum aperture opening time of 7 ms was placed in front of the camera lens to act as a physical barrier to the intense flame emission while the CCD was being digitized, which reduced this source of interference to negligible levels.

The intensified CCD has a full image size of 578 x 384 pixels. Since the CCD array is cooled to reduce the dark current, the digitizing process becomes the noise limiting step. To minimize this source of noise, a relatively slow digitizing rate (100 kHz) was employed, resulting in a full image readout time of approximately 2.3 seconds. This limited the number of images that could be obtained during a rocket firing. However, the camera system can be setup to digitize only the portion of the acquired image on the CCD that is of interest, while the remaining regions can be fast scanned without digitizing. By reducing the number of pixels digitized, the acquisition time speeds up and the resulting data file size is reduced.

Both instantaneous (single pulse) and ten pulse averaged two-dimensional images consisting of 350 x 360 pixels (50 x 50 mm) were acquired. The instantaneous images recorded the OH-radical fluorescence from a single laser pulse. Three such images were obtained during a four second rocket firing. In addition, LIF images resulting from 10 sequential laser pulses were

integrated directly onto the CCD to obtain a 10 pulse average two-dimensional LIF image. Two 10 pulse averaged images were acquired in a four second firing. In this way, information from 20 pulses can be obtained in a single firing as compared to three single shot images. This ten pulse averaging technique is useful in obtaining a statistically significant average, but any instantaneous structure information is lost. One-dimensional cross-section images were also obtained of the OH-radical fluorescence resulting from a laser beam passing through the combustion chamber. The camera was setup for a 20 x 350 pixel (2.8 x 50 mm) image centered on the laser beam. Ten instantaneous one-dimensional images were obtained during a firing.

The peak laser intensity of each pulse was also recorded along with the corresponding image. A portion of the beam was reflected by a quartz flat onto a fast photodiode. A high speed peak detector with a sample and hold circuit was used to sample the laser pulse corresponding to the image collected. The signal was digitized by the camera controller and stored as the first row of the image.

The intensity variation across the sheet was needed to correct the OH-radical fluorescence images. Before and after a series of firings a small rag saturated with acetone was inserted into the combustion chamber through the nozzle. The acetone vapors fluoresce at the same wavelength as OH, thus an image of the laser sheet intensity distribution could be obtained without disturbing the experimental setup. An instantaneous measurement of the sheet intensity profile was also acquired by reflecting a portion of the sheet beam with two quartz microscope slides onto a high cotton and bleach content card stock. The resulting fluorescence was of the same order as the OH-radical fluorescence and the two images were recorded together on the CCD camera. The linearity of the card fluorescence was checked by changing the incident laser intensity and observing the fluorescence from the card. The resulting fluorescence was found to be linearly proportional to the incident laser intensity over the range utilized in these experiments.

The intensified cooled array CCD camera was used for detecting both one- and two-dimensional OH-radical fluorescence images. The fluorescence signal detected by each pixel of the camera can be expressed as:

$$S_F = (I_v B)(F_y)(f_B N_i V_c) \left( \eta \frac{\Omega}{4\pi} \right) \tau_p \quad (\text{Equation 3.1})$$

The first parenthetical term depends on the local laser intensity,  $I_v$ , and the Einstein  $B$  coefficient (transition probability) for a particular transition. Corrections for variations of this term are obtained by normalizing the image by the laser sheet intensity profile. The second term,  $F_y$ , is the ratio of the radiative decay rate over all possible decay rates from the laser excited state. In the linear fluorescence regime, this factor is proportional to the square root of temperature if the quenching rate does not vary significantly with composition. The third parenthetical term represents the number of absorbing molecules in the collection volume. The size of the collection volume,  $V_c$ , is determined by the laser sheet thickness and the field of view of a pixel element, while the number of absorbing molecules per unit volume is given by the product,  $f_B N_i$ . The Boltzmann fraction,  $f_B$ , is the fraction of the total population,  $N_i$ , resident in the energy level excited by the laser. For a given level,  $f_B$  depends only on spectroscopic parameters and the local gas temperature. The next parenthetical term represents the collection efficiency of the lenses, filters and camera systems. Finally, the last term,  $t_p$ , is the laser pulse duration. The equation can be simplified to:

$$S_F = C I_v F_y f_B N_i \quad (\text{Equation 3.2})$$

by defining a proportionality constant,  $C$ , that includes all the constant terms in Equation 3.1. For a given laser intensity, the proportionality between the fluorescence signal and the number density of the absorbing species can be considered to be a constant times the fluorescence yield,  $F_y$  and the Boltzmann population fraction,  $f_B$ . The factor  $F_y f_B$  is a function of the ground state rotational quantum number,  $J''$ , and the local temperature. Assuming that  $F_y$  is proportional to the square root of the local temperature, the factor  $F_y f_B$  is constant to within 10% for a temperature range of 1550 to 3540 K for  $J''=8$ , and 1800 to > 3500 K for  $J''=9$ . These temperature ranges envelop the adiabatic flame temperatures for gaseous hydrogen/oxygen combustion for O/F ratios from four to eight. Note that the stoichiometric O/F ratio for  $\text{GH}_2/\text{GO}_2$  propellants is eight. Choosing transitions from these levels minimizes the variation of the OH-radical fluorescence signal due to temperature variations, provided that quenching does not vary significantly. In the present experiments, no attempt has been made to place the OH-radical concentrations on an absolute basis that would require complementary temperature and species measurements to account for quenching effects.

### 3.2.2 Laser Doppler Velocimetry

A Phase Doppler Particle Analyzer (PDPA) instrument was used to measure the velocity field in the flow downstream of the shear coaxial injector in the rocket chamber. The PDPA instrument is capable of measuring both velocity and size of spherical particles traversing the probe volume; here, only the laser Doppler velocimetry (LDV) capability was used to measure the seeded  $\text{GO}_2$  and  $\text{GH}_2$  flows. The schematic for the experimental setup is shown Fig. 3.3.

A probe volume was formed inside the rocket chamber by splitting an argon ion laser beam ( $\lambda=514.5 \text{ nm}$ ) into two beams and focusing them to an intersection as shown in Fig. 3.3. Probe volume characteristics are determined by the transmitting and receiving optics and are given in Table 3.2. To avoid problems with reflections caused by the quartz windows of the rocket chamber, both the transmitting and receiving optics were inclined at  $15^\circ$  with respect to the horizontal plane. The optics were also mounted on translation stages to allow the probe volume to be traversed vertically through the flowfield. In order to reject light from the luminous flame of the combusting  $\text{GH}_2/\text{GO}_2$  flow, a 10 nm bandpass filter centered around 514.5 nm was placed in front of the receiving optics. Fluidized bed seeders were used to introduce aluminum oxide ( $\text{Al}_2\text{O}_3$ ) seed particles into the  $\text{GH}_2$  and  $\text{GO}_2$  flows. Both the  $\text{GH}_2$  and  $\text{GO}_2$  flows were independently seeded. The system used for seeding the flow is shown in

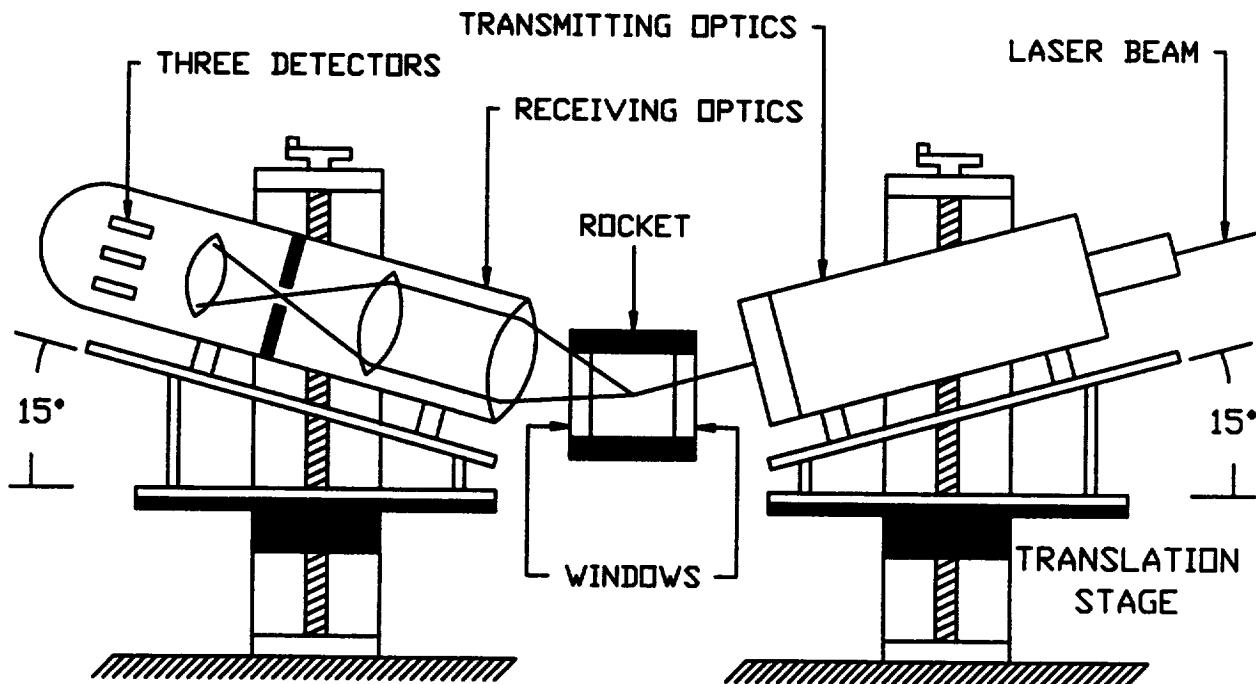


Fig. 3.3. Schematic of laser Doppler velocimetry (LDV) setup.

**Table 3.2. LDV Parameters**

Laser Power	0.5 W
Wavelength	514.5 nm
Probe Volume Diameter	350 $\mu\text{m}$
Fringe Spacing	12.5 $\mu\text{m}$

Fig. 3.4. A small portion of the main gas flow was diverted into the seeder and flowed through a porous plate (this plate traps particles greater than 5 mm) on which seed particles were placed. This secondary flow entrained seed particles as it exited through the top of the seeder to recombine with the primary flow.

The aluminum oxide ( $\text{Al}_2\text{O}_3$ ) seed particles of nominally 0.3  $\mu\text{m}$  diameter were chosen because of their low toxicity, availability and cost, as well as for its compatibility with the experimental environment. The melting temperature of aluminum oxide is 2300 K [2]. Calculations with the Combustion Equilibrium Calculation (CEC) [1] program indicated that the temperature in the chamber reaches 2900 K; however, the presence of sufficient seed particles for LDV measurements throughout the length of the chamber suggested that seed particle melting was not a significant problem.

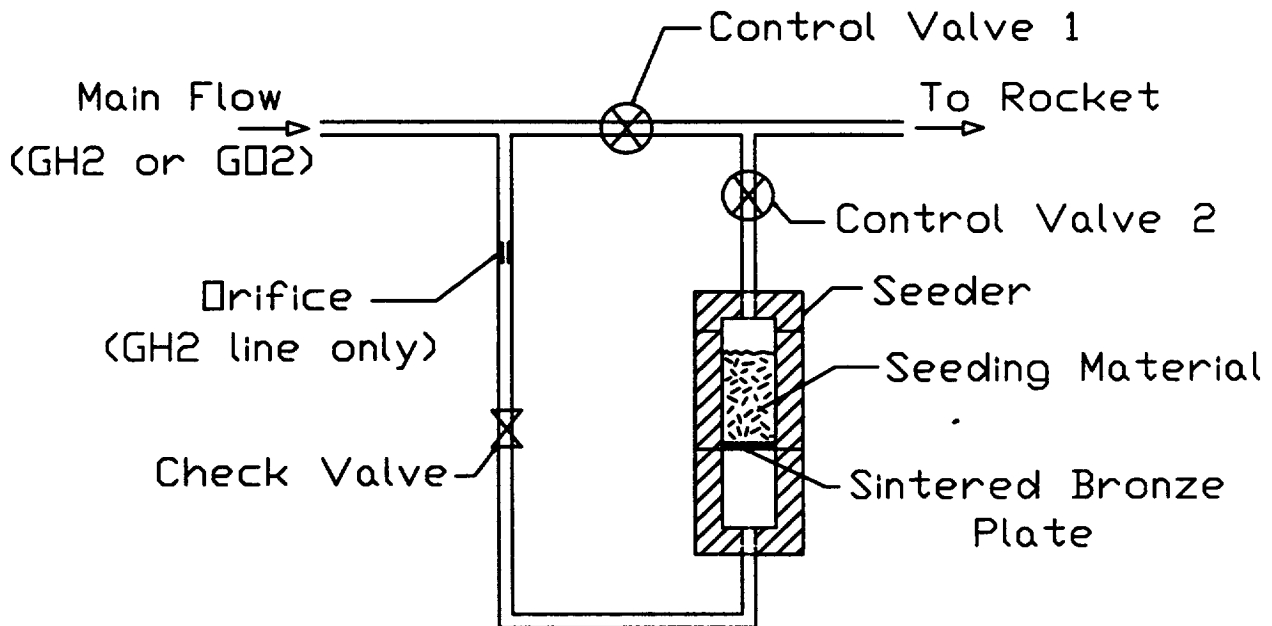


**Fig. 3.4. Schematic of the fluidized bed seeder apparatus. A fluidized bed seeder was incorporated into both the GO<sub>2</sub> and GH<sub>2</sub> feed lines. Secondary flow was directed through the orifice and check valve into the seeder from below. The secondary flow entrains seed particles and then mixes with the main flow.**

The velocity field in the rocket chamber corresponding to the flow conditions for Case 1 listed in Table 3.1 was measured using LDV. The flow conditions of  $\text{GH}_2$  corresponding to Case 2 were beyond the measurement range of the LDV instrument, and therefore velocity measurements for this case were not attempted. For the flow conditions corresponding to Case 1, the radial velocity profile was measured at three axial locations downstream of the injector face, viz., 25.4, 50.8 and 127 mm (1, 2 and 5 in.). At each axial location, velocity measurements were made in 1.52 mm (0.06 in.) radial intervals. Within the  $\text{GH}_2/\text{GO}_2$  shear layer, velocity measurements were made at a finer radial interval of 0.25 mm (0.01 in.). It should be noted that the velocity measurements in the rocket environment were characterized by a high percentage of signal to noise rejections resulting from both multiple particles in the probe volume and window contamination by the seed material.

The measurement procedure involved focusing the probe volume at a measurement location and hot-firing the rocket for four seconds. Depending on the measurement location, either the  $\text{GO}_2$  or the  $\text{GH}_2$  fluidized bed seeder was activated. The velocities of seed particles were measured in the time interval from 1.4 to 3.9 seconds (2.5 second interval) into the four second rocket firing to avoid measuring velocities during the start up and shut down transient periods. Velocity histograms were then compiled and statistically evaluated to yield the mean and root mean square velocities. This procedure was repeated at each measurement location. For all the measurement locations in the central part of the flow, at least 1000 individual data points were collected to construct the velocity histogram. For some radial locations, this required collecting velocity data points from a number of rocket firings to construct the histogram. However, for a few radial measurement locations near the edges of the flowfield, the 1000 data point criterion had to be compromised because of low data rates. Therefore, the errors associated with these edge points are higher.

The velocity profile measurements reported here for the three axial locations represent in excess of 300 rocket firings, of which 230 firings contributed to the measurements. Data from the remaining firings were unusable because the seed material contaminated the quartz windows.

### **3.2.3 Planar Laser Light Scattering**

The planar laser light scattering (LLS) technique was used to measure the mean distributions within the combustion chamber of refractory particles seeded into the propellant flows to serve as passive markers. This technique involves seeding each of the propellant streams

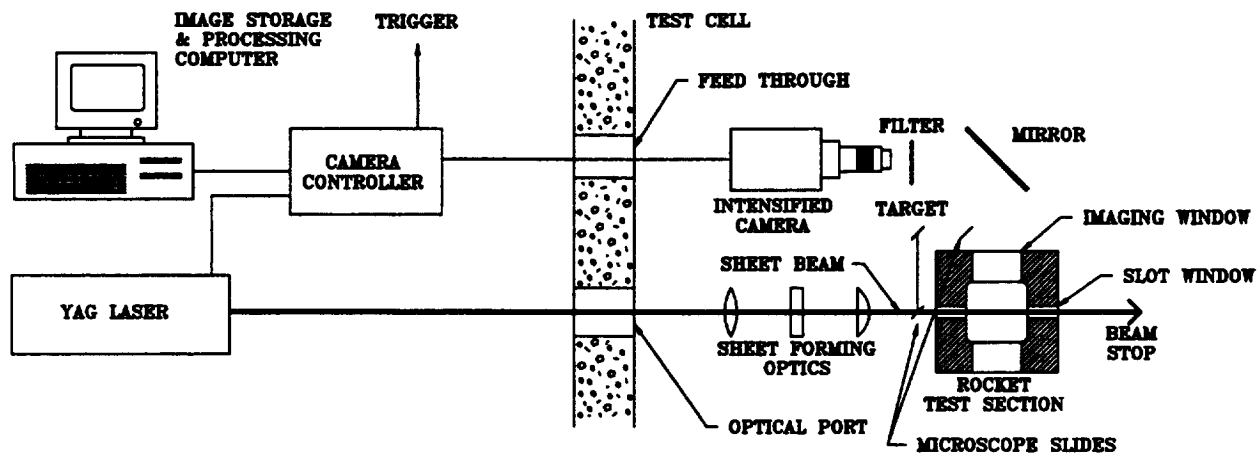


**Fig. 3.5. Experimental setup for planar laser light scattering experiments.**

individually with sub-micron particles, illuminating the flowfield with a laser sheet, and recording the resulting scattered light. The scattered light intensity is proportional to the concentration of the seed particles. If the flow is properly seeded and the seed follows the gas stream, the spatial extent of the particles can be related to mixture fraction, density, species concentration and temperature [1,2,3]

The flow seeding methodology described in the last sub-section was also utilized for these experiments. Please refer to the last sub-section for details on flow seeding.

The experimental setup for the planar laser light scattering (LLS) measurements is shown in Fig. 3.5. To maximize the light scattering signal due to the particles and to minimize scattering from the windows, the polarization vector of the frequency double Nd-YAG laser beam (532 nm) was oriented such that the camera recorded vertically polarized scattered light. A narrow bandpass interference filter (1 nm bandpass centered around 532 nm) was placed in front of the camera to pass only the elastically scattered light.

An image of the laser sheet intensity profile was obtained to correct the scattered light image for intensity variations across the laser sheet. This profile was obtained by reflecting a portion of the laser sheet toward a target with a microscope slide. A second slide, near the viewing window of the rocket, directed the scattered light from the target onto the camera to be imaged along with the scattered light from the particle seeded flow.

A Nikon 105 mm UV-Nikkor f4.5 lens imaged the scattered light onto a Princeton Instruments cooled array intensified CCD camera. The recorded image size was 250 x 300 pixels which corresponds to an image area of 38.1 x 45.7 mm (1.5 x 1.8 in.). Images were acquired at

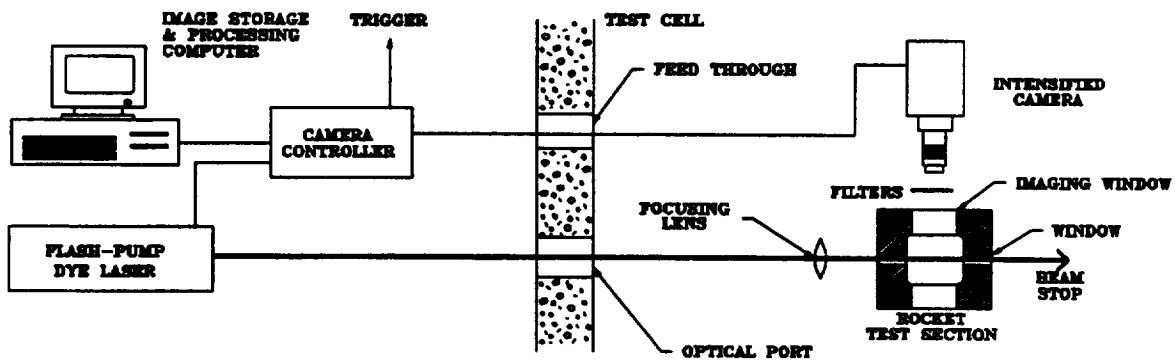


**Fig. 3.6. Raman spectroscopy experimental setup for species measurements.**

5 Hz and, therefore, 15 images were recorded for each firing (time duration of a firing was 4 seconds; chamber pressure was steady for at least 3 seconds of a firing).

### 3.2.4 Raman Spectrometry (Line)

The Raman spectroscopy technique was developed and applied for making line images of the species field in the combustion chamber. Note that various optical configurations can be used for applying the Raman spectroscopy technique [3,4], here an optical arrangement that stresses maximum collection of the weak Raman signal for making line images of the species field was developed. The experimental setup shown in Fig. 3.6 includes a Cynosure flash pump dye laser for Raman excitation and an intensified charged coulomb device (CCD) camera for Raman signal detection.

Specifics regarding the collection side of the setup are summarized in Table 3.3. The 10 Hz repetition rate flash pump dye laser used for Raman excitation delivers a pulse energy of 1 J (duration of 3  $\mu$ s) at a wavelength,  $\lambda$ , of 510.8 nm. The 10 mm diameter laser beam was focused to a waist of 0.9 mm at the centerline of the rocket chamber. The full width at half maximum (FWHM) laser bandwidth is measured to be 0.45 nm. The integrated slow scan intensified 16-bit CCD camera (12 bits were used) equipped with a f# 1.2, 50 mm focal length lens, was aligned 90° to the laser beam (Fig. 3.6). For image analysis, only a portion of the total image (area of 144 x 20 pixels corresponding to a line image field of view of 32.5 x 4.5 mm) corresponding to the laser beam region was utilized. This optical arrangement represents a near optimum configuration for signal strength with respect to equipment limitations. Multiple

**Table 3.3. Collection Side Optical Characteristics.**

Camera Type	12 Bit Intensified CCD Camera
Camera Readout Rate	200 kHz
Camera Gate Width	3 ms
Camera Lens	50/1.2 with PK-11 and PK-12 Extensions
Field of View	32.5 x 4.5 mm
GO <sub>2</sub> Interference Filter	$\lambda_c=555.4$ nm, $\Delta\lambda=9.5$ nm
GH <sub>2</sub> Interference Filter	$\lambda_c=648.8$ nm, $\Delta\lambda=9.2$ nm
H <sub>2</sub> O Interference Filter	$\lambda_c=627.3$ nm, $\Delta\lambda=10.6$ nm
GN <sub>2</sub> Interference Filter	$\lambda_c=581.2$ nm, $\Delta\lambda=8.5$ nm

uncorrected instantaneous line images were obtained at three axial stations corresponding to 25.4, 50.8 and 127 mm from the injector face at the laser 10 Hz rate. The camera was operated at 20 Hz, hence images of the background luminosity (no laser beam) were also recorded at 10 Hz for background level correction.

For the wavelength of the laser used here ( $\lambda=510.8$  nm), the center wavelength for the shifted Stokes signal from GO<sub>2</sub>, GH<sub>2</sub>, GN<sub>2</sub> and H<sub>2</sub>O species are 555.4, 648.8, 581.2 and 627.3 nm, respectively [3]. For each species measurement, a 10 nm (nominally; see Table 3.3 for specifics) bandpass filter centered at the aforementioned wavelengths was placed in front of the camera. In addition, for each species measurement, a high pass cutoff filter was placed in front of the camera to further isolate the Raman signal from the Rayleigh scattered light. Note that the choice of the interference filter bandwidth affects the temperature sensitivity of the Stokes bandwidth factor. For example, with Nd-YAG laser (532 nm) excitation for GN<sub>2</sub> species, the temperature dependence of the Stokes bandwidth factor to interference filter bandwidth shows that a filter centered at 607.3 nm with a bandwidth of 5 nm effectively makes the species measurement temperature independent to within 5% [3]. Alternately, the Stokes bandwidth factor increases non-linearly by about 40% for the GN<sub>2</sub> species temperature range from 300 to 3000K with a 10 nm bandwidth filter centered at 607.3 nm [3]. Clearly, for species field concentration measurements, the filters should be chosen to make the measurement temperature independent; otherwise careful filter calibration is necessary.

The major species mole fractions and temperature are obtained from the wavelength averaged vibrational Raman signal intensity values. Raman signal intensity is related to the number density of the molecule, a constant and a temperature dependent function that relates the spectral bandwidth factor to the Raman signal strength as represented by the following equation.

$$S_i = n_i K_i f_i(T) \quad \text{(Equation 3.3)}$$

The constant in this equation accounts for the laser pulse energy, species Raman cross section, optical collection efficiency and optical solid angle.

To quantify the Raman measurements, each species was calibrated with a known gas sample (number density) for determining  $K_i$  which is a constant that depends on the Raman cross sections that enter into the above equation. For  $\text{GO}_2$ ,  $\text{GH}_2$  and  $\text{GN}_2$  species, the experimental setup was calibrated using a pure species sample at standard temperature and pressure conditions in the rocket chamber. The  $\text{H}_2\text{O}$  species was calibrated utilizing a vaporizer placed in the location of the rocket chamber. This vaporizer consisted of a central tube (12.7 mm (0.5 in.) diameter) that flowed water vapor surrounded by a co-annular flow of air (28.1 mm (1.5 in.) outer diameter). A thermocouple was used to measure the exit temperature ( $\approx 393$  K) of the gases for calibration purposes and to ensure that the temperature was above the boiling point of water. Calibration measurements were taken at 3 mm from the steam tube exit. These calibrations for  $K_i$ , along with the theoretically calculated bandwidth factor,  $f_i$ , were then used to calculate species number density using the above equation. Temperature was calculated by summing the species number densities and calculating the temperature using the ideal gas law.

### 3.2.5 Injector Thermocouple Instrumentation

To verify that the calculated mean inlet velocities documented in Table 3.1 were correct, temperature measurements of the propellant temperature at the injector face were necessary. To this end, the shear coaxial injector used for the above experiments was instrumented with thermocouples as shown in Fig. 3.7. Thermocouples labelled Tc1 and Tc2 in Fig. 3.7 were grounded 0.51 mm (0.02 in.) diameter Type T (Copper-Constantan) thermocouples in a stainless steel sheath. Thermocouple, Tc1, was silver soldered to the outside of the  $\text{GO}_2$  post flush with the tip of the post. Thermocouple, Tc2, was silver soldered to the outside  $\text{GH}_2$  annulus wall, 25.4 mm (1 in.) back from the injector face plate. These surface mounted thermocouples provided the metal temperature. Thermocouples, Tc3 and Tc4 as shown in the figure, were exposed junction Type T

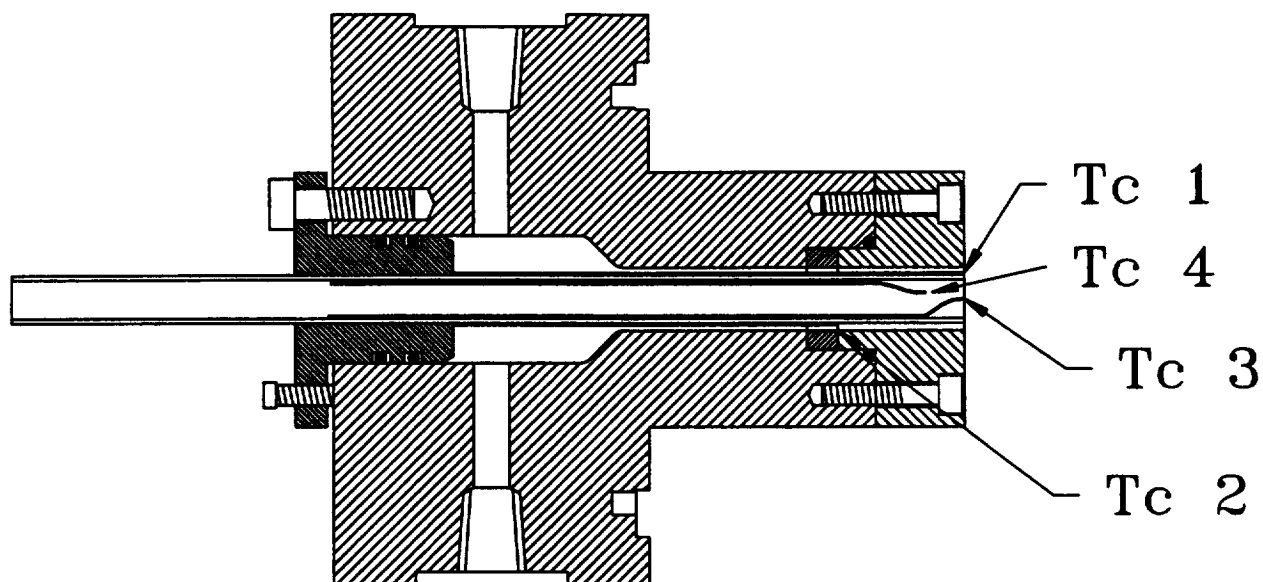


**Fig. 3.7. Shear coaxial injector instrumented with four thermocouples for temperature measurements.**

thermocouples. For these thermocouples, the wire and junction bead diameters were 0.076 mm (0.003 in.) and 0.25 mm (0.01 in.), respectively. The lead wires were stainless steel sheathed with an outer diameter of 0.51 mm (0.02 in.). The exposed junction of these thermocouples were positioned in the center of the  $\text{GO}_2$  post; Tc3 was flush with the injector exit and Tc4 6.86 mm (0.27 in.) recessed from the injector face. These two thermocouples provided the  $\text{GO}_2$  temperature in the injector. Due to the small size of the fuel annulus, it was not possible to mount a thermocouple for measuring the inlet  $\text{GH}_2$  temperature. The wires for all the four thermocouples were routed through the flow passage of the injector. These thermocouples interfered with the propellant flow and were therefore used specifically for temperature measurements during rocket firings. For other measurements in the rocket chamber, these thermocouples were removed.

### **3.3 RESULTS AND DISCUSSION**

The flowfield measurements in the combusting flowfield downstream of the shear coaxial injector in a rocket chamber for the  $\text{GH}_2/\text{GO}_2$  propellants are presented. Emphasis is given to examining the evolution of the flowfield in terms of the interaction between the two propellant jets. In particular, studies of the  $\text{GO}_2$  core and its interaction with the surrounding  $\text{GH}_2$  flow are examined. The composite flowfield in terms of the mean velocity field, turbulent intensity, flame structure, propellant mixing characteristics and species concentration fields are discussed.

To orient the reader to the global geometry, a photograph of the  $\text{GO}_2/\text{GH}_2$  rocket firing is shown in Fig. 3.8. In the photograph, flow is from right to left. On the right side of the photograph, the tubes for the  $\text{GH}_2$  manifold and  $\text{GN}_2$  flow used for window purging are seen. The flame front is clearly seen through the window section. The igniter shown in the schematic of Fig. 2.1 can not be seen in the photograph as it physically located on the back side of the rocket chamber. The tube emanating from the nozzle section is the water line that feeds cooling water to the nozzle.

### 3.3.1 OH-Radical Results

The OH-radical fluorescence measurements discussed here were all obtained at the same propellant mass flow rates as for the previously discussed velocity measurements. The injector geometry was different in that the outer diameter of the fuel annulus was 10.74 mm (0.423 in.). The flow parameters for this case are presented in Table 3.1, Case 2.

The OH-radical is a key intermediate in hydrocarbon and hydrogen combustion. Near the injector, OH-radical levels indicate the position of the primary reaction zone where the oxidizer to fuel ratio is locally stoichiometric[5,6]. Further downstream in the flowfield, the reactions are reaching completion, and therefore the temperature field is high throughout this region. Here,

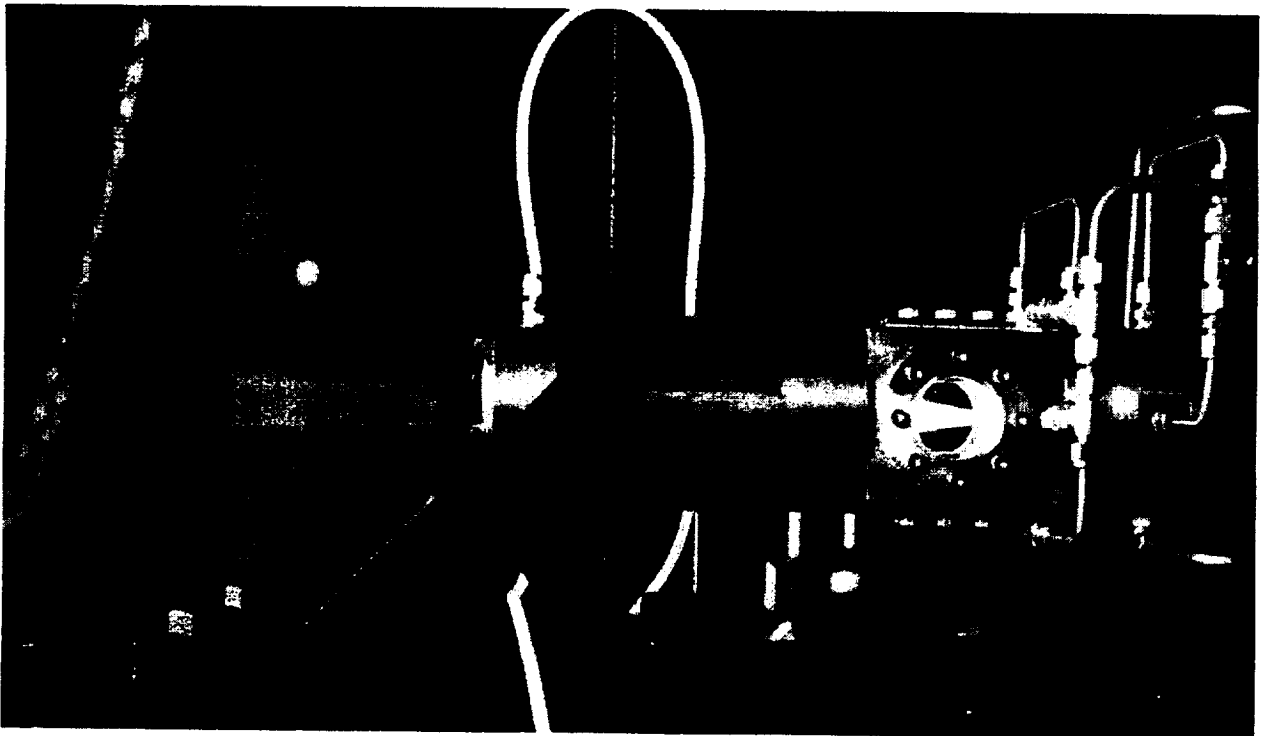


**Fig. 3.8. Panoramic photograph of  $\text{GO}_2/\text{GH}_2$  rocket firing. Notice nozzle plume and  $\text{GO}_2/\text{GH}_2$  flame front at exit of shear coaxial injector. Flow conditions correspond to Case 1, Table 3.1.**

the OH-radical is stable because of high temperatures and therefore it can be used to infer the extent of reaction and flame spreading[5].

The two-dimensional LIF images were obtained by exciting the combined  $Q_1(9)$  and  $Q_2(8)$  line of the (1,0) band of OH-radical at 283.92 nm. The  $Q$  transitions were chosen because their high absorption efficiencies yield strong signals. An instantaneous image of OH-radical fluorescence near the injector is shown in Fig. 3.9. The left and right edges of this image are 6.35 mm (0.25 in.) and 32.5 mm (1.28 in.) downstream of the injector face, respectively. The flow is from left to right with  $GO_2$  flow in the center surrounded by coaxial  $GH_2$  flow. In this image, the laser sheet passes from top to bottom. The image has been corrected for the laser sheet intensity profile. The black areas correspond to high OH-radical fluorescence levels

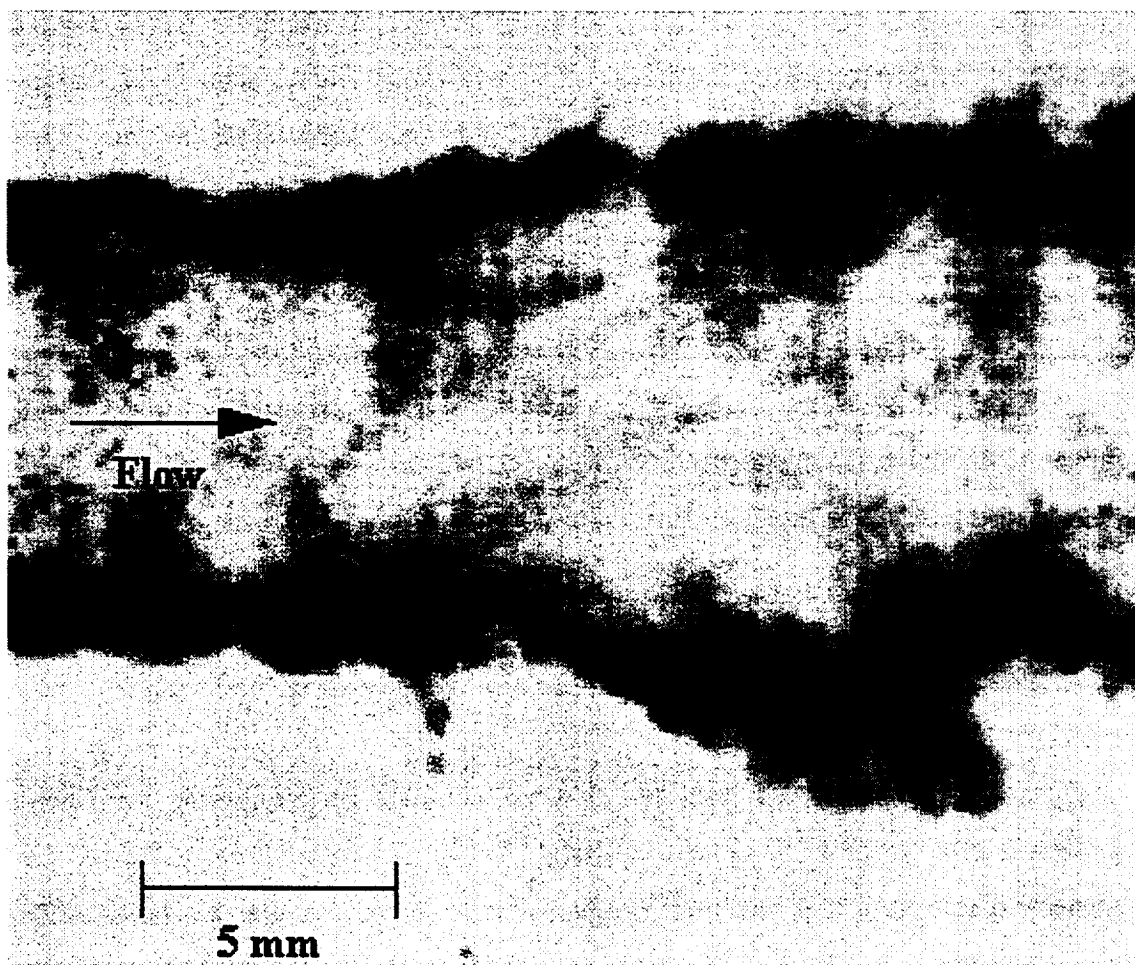


**Fig. 3.9. Instantaneous two-dimensional image of OH fluorescence. Field of view is from 15 mm to 38 mm downstream of injector face. Laser direction is from bottom to top. Dark regions indicate high fluorescence intensity.**

whereas the white areas correspond to low levels. It can be seen that the OH-radicals, and therefore the reaction zone, are confined to a narrow region along the shear layer on either side of the GO<sub>2</sub> jet. As the flowfield develops downstream, the reaction zone widens. The turbulence ( $Re=3.6 \times 10^5$  for GO<sub>2</sub> flow and  $7.95 \times 10^4$  for GH<sub>2</sub> flow) of the combusting flow is manifested by the presence of large structures that are readily observed in the image. The OH-radical images are similar to results observed in turbulent hydrogen/air diffusion flames studied at atmospheric pressure conditions[6] at Reynolds numbers between  $10^3$  and  $10^4$ . In the present experiments, the elevated pressure (1.31 MPa) extends the Reynolds number range to the order of  $10^5$ .

As the number density of the OH-radical increases, the optical thickness increases and both the incident laser beam and the resulting OH-radical fluorescence can be attenuated. The effect of the incident beam attenuation is observed in Fig. 3.9 where the signal levels of the reaction zone in the lower half of the image are significantly higher than in the upper half. The level of attenuation is significant even though the thickness of the reaction zone is narrow in this region. This is because the OH-radical number density is very high due to both the high chamber pressure and the high mole fractions of OH-radicals in a combusting hydrogen/oxygen flame. Near the injector, the OH-radical layer is thin and, therefore, OH-radical fluorescence trapping is not a significant problem. At locations further downstream, two-dimensional LIF images of OH-radical (not shown here) show that OH-radical fluorescence trapping and laser beam attenuation are significant because of a thicker OH-radical layer. At a location 152.4 mm (6 in.) downstream from the injector, very little signal was observed even though the highest level of OH-radicals was expected at this location. For the transitions considered here, calculations based on equilibrium OH-radical concentration levels showed that for this axial location, 95% of the fluorescence would be trapped and virtually all of the incident beam would be absorbed.

Images averaged over ten laser pulses were obtained by integrating the OH-radical fluorescence directly on the CCD camera detector. These images were corrected for the laser sheet intensity distribution and five such images were averaged together to obtain a 50 pulse average as depicted in Fig. 3.10. The average reaction zone is seen to expand as the flow progresses downstream which is largely a result of the unsteady nature of the flame reaction zone as described previously. Once again, significant laser beam attenuation is observed. The field of



**Fig. 3.10. Average two-dimensional image of OH fluorescence. Average of 70 frames. Field of view is from 15 mm to 38 mm downstream of injector face. Laser direction is from bottom to top. Dark regions indicate high fluorescence intensity.**

view in this figure is the same as for Fig. 3.9. These average OH images clearly show that the average reaction zone, as characterized by the OH-radical LIF images, broadens with downstream distance.

One-dimensional OH-radical fluorescence measurements were also obtained at the axial locations shown in Figs. 3.11 and 3.12 (the axial locations overlap the measurement region for Figs. 3.9 and 3.10). Since these measurements were taken with a focused laser beam, the incident light intensity was increased dramatically over that available for the two-dimensional imaging experiments. In fact, measurements were taken at a reduced laser power to make sure that the OH-radical fluorescence was linear. The  $P_2$  line was selected in order to reduce the attenuation of incident laser light by using a weaker absorbing transition of the OH-radical.

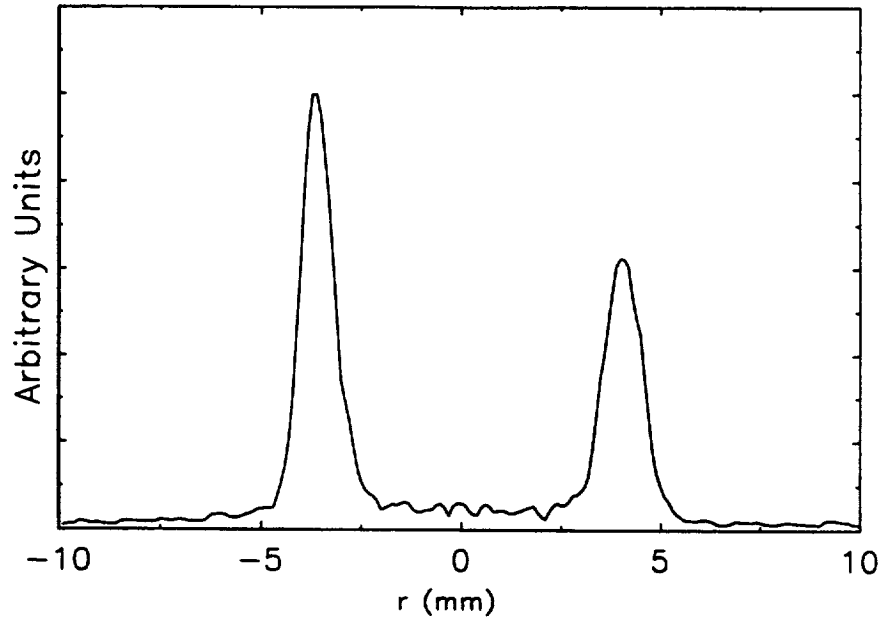


**Fig. 3.11. OH-radical fluorescence intensity (arbitrary units) versus radial distance at an axial location of 9.53 mm (0.38 in.) from the injector face obtained from a contour plot corresponding to Fig. 3.10. The laser sheet direction is from left to right.**

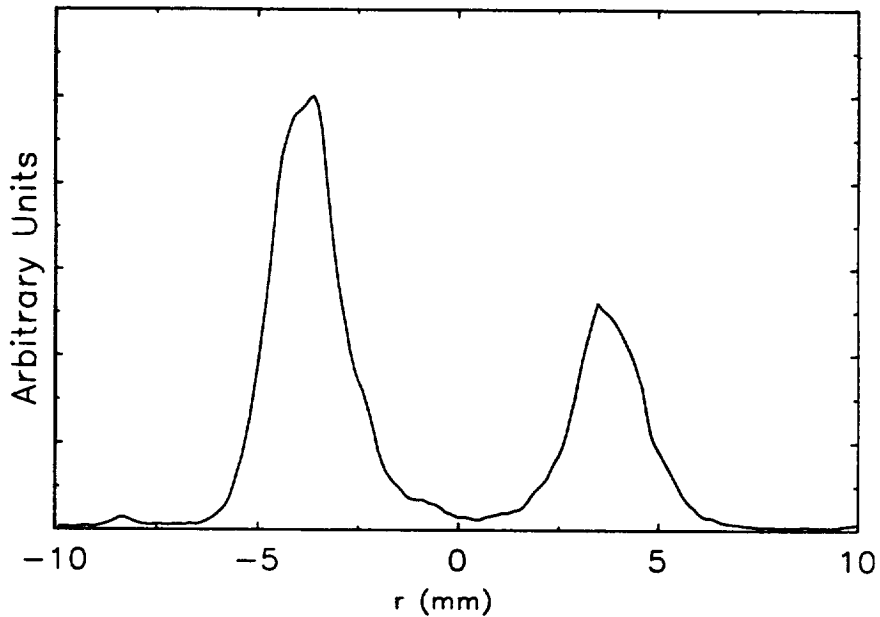


**Fig. 3.12. OH-radical fluorescence intensity (arbitrary units) versus radial distance at an axial location of 25.4 mm (1 in.) from the injector face obtained from a contour plot corresponding to Fig. 3.10. The fluorescence intensity scale is the same as in Fig. 3.11. The laser sheet direction is from left to right.**

Fig. 3.13 shows a one-dimensional LIF image of the OH-radicals for the 9.53 mm (0.375 in.) axial location obtained by averaging over nine laser pulses. A comparison of the cross-sectional

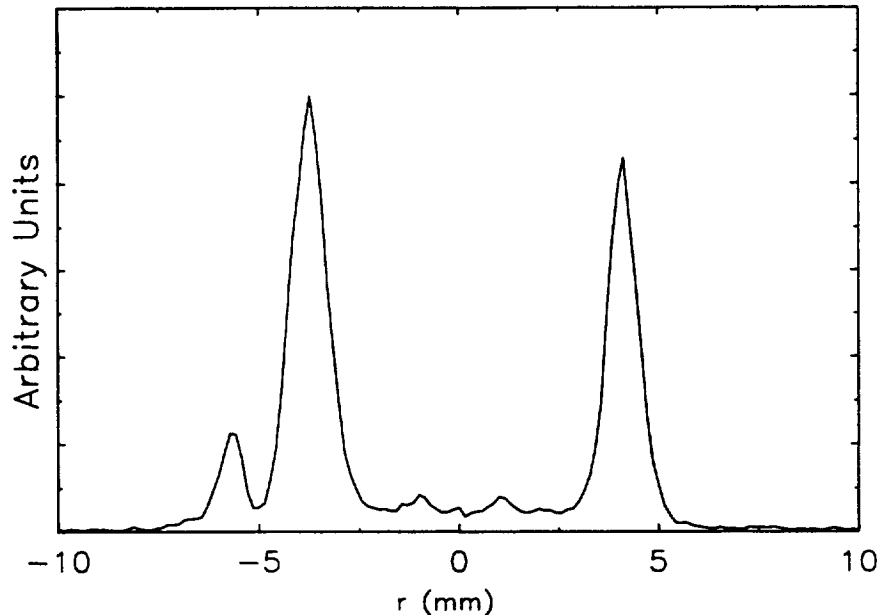


**Fig. 3.13. OH-radical fluorescence intensity (arbitrary units) versus radial distance at an axial location of 9.53 mm (0.38 in.) from the injector face obtained by averaging nine one-dimensional single pulse images. The laser beam direction is from left to right.**

intensity profiles shown in Figs. 3.11 and 3.13 indicates that the profiles are very similar. However, in comparing the two figures, it is evident that on the far side of the flame (with respect to the incident laser sheet/beam), the peak intensity is higher in Fig. 3.13, indicating that the level of attenuation is reduced for the laser beam in this experiment. It should be noted that the choice of the  $P_2$  line only reduces the attenuation of the incident beam. Absorption of the resulting fluorescence from the OH-radical as this light traverses the reacting flow is still substantial.

A one-dimensional OH-radical LIF image at an axial location of 76.2 mm (3 in.) is shown in Fig. 3.14. Note that for this figure, the abscissa scale is different from that in Figs. 3.11-3.13. Clearly, the incident laser beam is still able to penetrate the entire flowfield allowing the imaging of the entire reaction region. Attenuation of the OH-radical fluorescence intensity is evident in Fig. 3.14 and consequently only qualitative flame structure information can be inferred from this one-dimensional image. The only significant point to be made from this figure involves the distribution of the OH-radicals at this axial location. In contrast to the LIF images obtained at axial locations closer to the injector, the results displayed in Fig. 3.14 show no distinct narrow flame region. The OH-radical fluorescence at this downstream location (76.2 mm (3 in.)) is observed to be distributed through the reaction region. These results are in

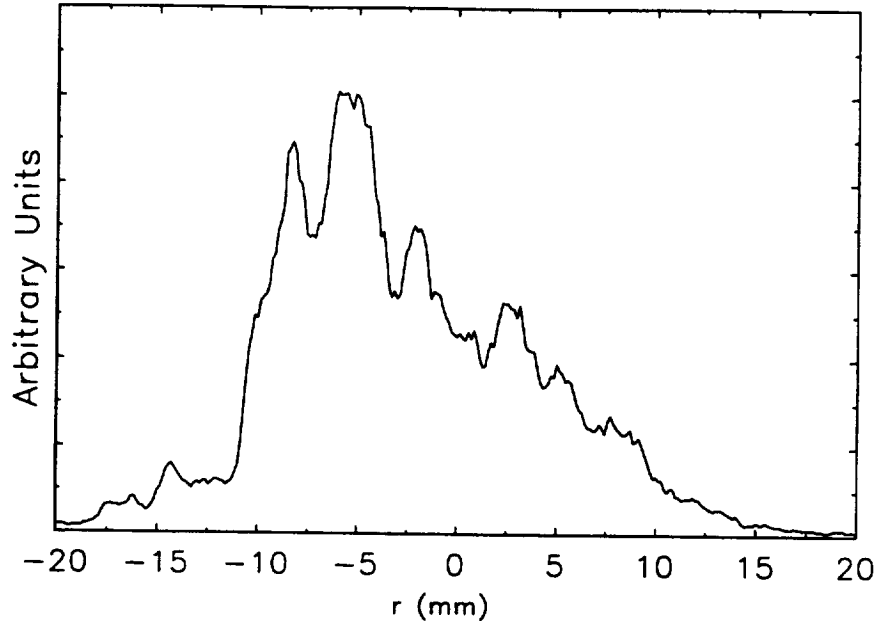


**Fig. 3.14. OH-radical fluorescence intensity (arbitrary units) versus radial distance at an axial location of 76.2 mm (3 in.) from the injector face obtained by averaging 20 one-dimensional single pulse images. Note that the scale for the abscissa differs from that of Figs. 3.11-3.13. The laser beam direction is from left to right.**

agreement with observations obtained in the downstream regions of turbulent diffusion flames [6].

The one-dimensional images are attractive because of the increased signal to noise ratio achievable and the large number of images that can be obtained in a single rocket firing. With some minor changes to the LIF system, 20 images can be obtained in a single four second rocket firing. The signal to noise ratio is greatly increased which enhances the minimum detectability limit. The increased laser intensity also enables the use of transitions that reduce the effects of laser beam attenuation.

At locations from approximately 100 mm (3.94 in.) downstream of the injector face to the nozzle entrance, the one-dimensional measurement technique is the only one possible with this setup because of the large laser attenuation and fluorescence trapping toward the aft end of the chamber. Quality two-dimensional measurements at this location would require the excitation of the (3,0) band of the OH-radical with a KrF excimer laser followed by the detection of the (3,3) or (3,2) fluorescence bands [7]. The laser attenuation would be greatly reduced with this system since the absorption in the (3,0) band is 100 times weaker than the (1,0) band absorption. The fluorescence trapping of the (3,3) or (3,2) band fluorescence would be very small since the

population fraction of the  $v''=3$  vibrational level of the OH-radical is very small at these flame temperatures.

### 3.3.2 Injector Tip Temperature Results

The rocket was fired at the flow conditions listed in Table 3.1, Case 1 and the temperatures in the injector were measured by installed thermocouples. Please refer to section 3.1.3 for details regarding the placement of the thermocouples. The results of multiple four second duration rocket firings showed that the temperature measurements were repeatable. The chamber pressure attains steady state condition in less than 0.5 seconds. The corresponding temperature traces measured by the thermocouples are shown in Fig. 3.15. The temperature measured by a thermocouple mounted 6 in. upstream of the injector in the  $GO_2$  line is also shown in the figure (indicated as ox T2). The traces for the  $GO_2$  sensing thermocouples, Tc3 and Tc4, show a sharp increase in the temperature right at ignition. However, after ignition, the temperature decreases rapidly to about

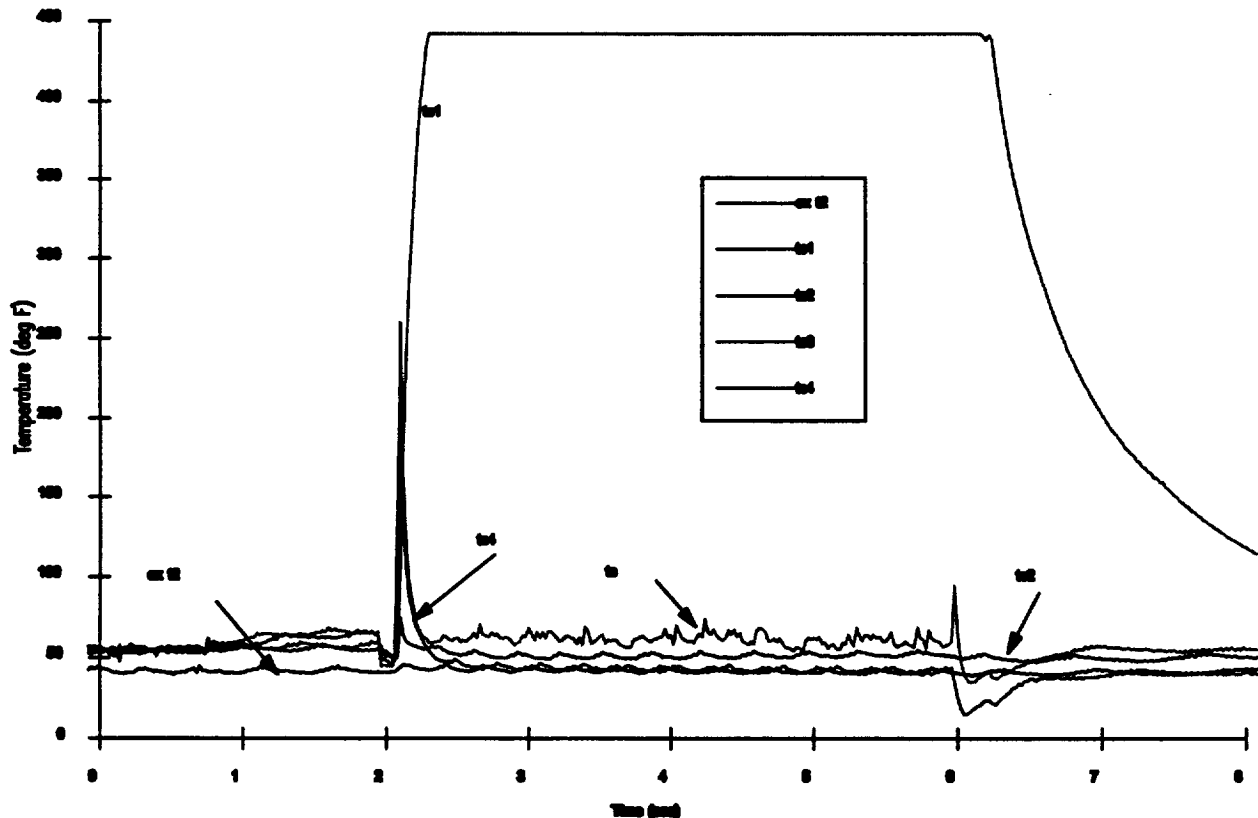
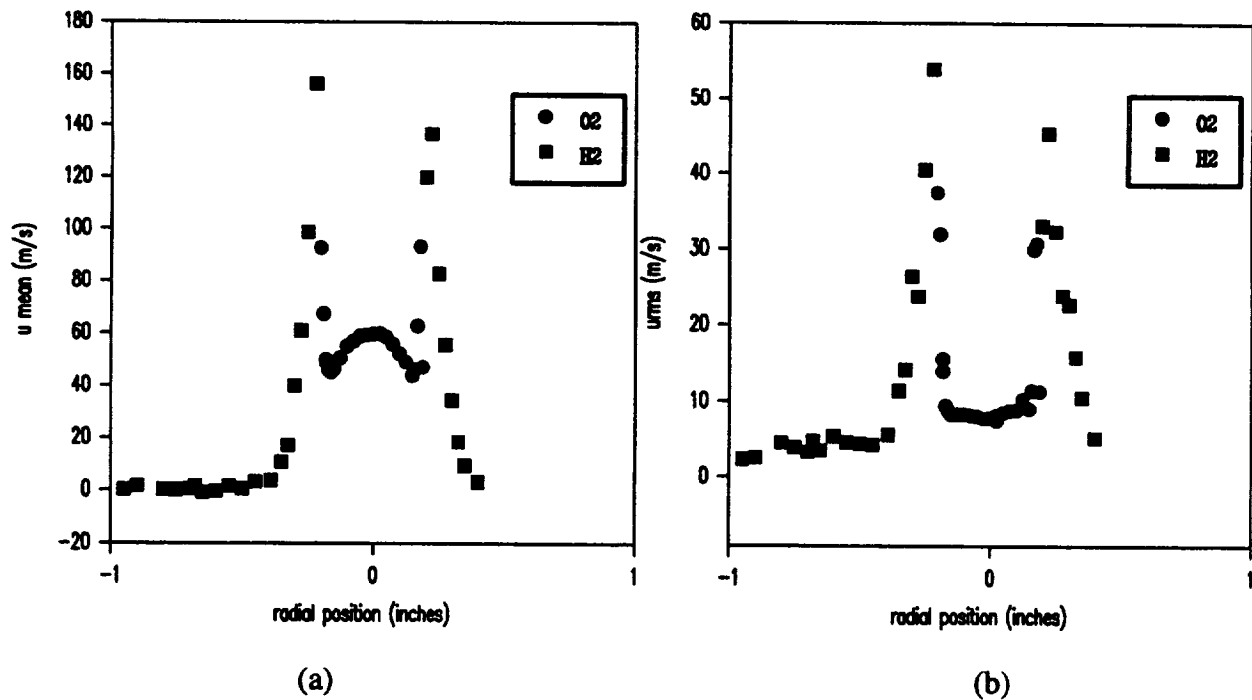


Fig. 3.15. Temperature versus time for a 4 second rocket firing. Temperature measurements are for the four thermocouples (Tc1-Tc4) locations shown in Fig. 3.7. The temperature trace from a thermocouple (ox t2) mounted 6 in. upstream of the injector in the  $GO_2$  flow line is also shown. This thermocouple is typically used for making temperature measurements of the incoming  $GO_2$  flow.

60°F and then stays constant at this value for the entire duration of the rocket firing. Notice that except for ignition, the temperature traces for Tc3, Tc4 and ox T2 are within a few degrees of each other for the test firing. These measurements show that during the firing, the GO<sub>2</sub> temperature right at the injector face does not increase significantly. The mean inlet velocity calculated for GO<sub>2</sub> (see Table 3.1, Case1) is therefore correct. The metal temperature traces corresponding to thermocouples, Tc1 and Tc2 (see Fig. 3.15), show that while the GO<sub>2</sub> post temperature rises (tc1 reaches its maximum at 450°F) to in excess of 450°F, the temperature of the outer wall of the fuel annulus (tc2) does not show any significant increase.

### 3.3.3 Velocity Field Results

The radial profiles of mean and root mean square (RMS) velocity were measured at 4 axial locations, viz., 12.7, 25.4, 50.8 and 127 mm (0.5, 1,2 and 5 in.) from the injector face. The near injector face (12.7 mm axial location) results are plotted in Fig. 3.16. The radial mean velocity profiles at the further three axial measurement locations are presented in the three inset graphs in Fig. 3.17, whereas the complementary RMS velocity profiles are depicted in Fig. 3.18.



**Fig. 3.16. (a) Mean velocity and (b) RMS velocity profiles at an axial distance of 12.7 mm (0.5 in.) from injector face.**

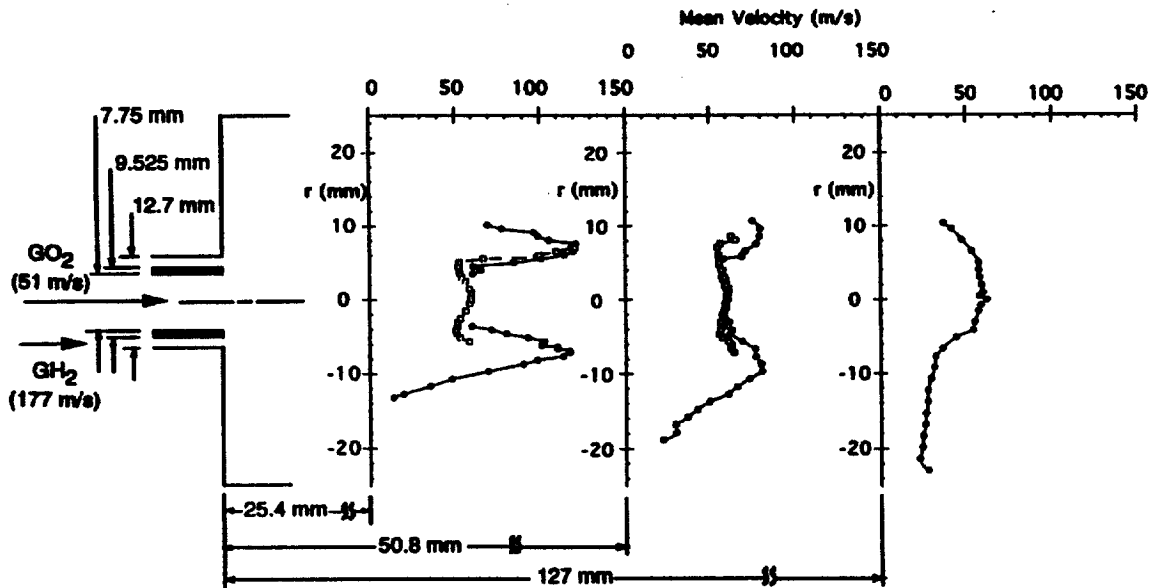


Fig. 3.17. Mean velocity profile measurements at three axial locations downstream of the injector face. Note that the axial distances are not to scale. Flow conditions are listed in Table 3.1, Case 1. The hollow square (□) and solid circle (•) symbols correspond to GO<sub>2</sub> and GH<sub>2</sub> flow seeding, respectively.

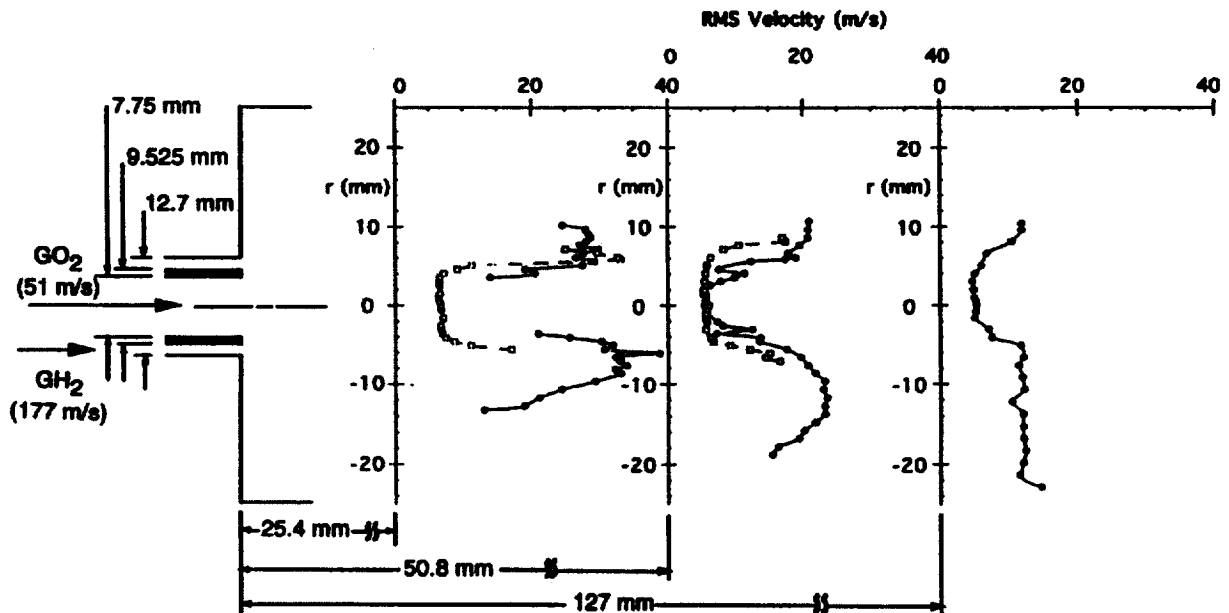


Fig. 3.18. RMS velocity profile measurements corresponding to the results shown in Fig. 3.17.

The corresponding rocket and shear coaxial injector parameters are listed in Table 3.1, Case 1. The mean injection velocities of  $\text{GO}_2$  and  $\text{GH}_2$  into the rocket chamber were 51 m/s (167 ft/s) and 177 m/s (581 ft/s), respectively.

At the closest measurement location, Fig. 3.16 (a), in the region downstream of the  $\text{GO}_2$  injector post, the velocity profile shows a peak velocity of about 60 m/s (197 ft/s) in the centerline followed by a decrease in the velocity with radial distance to a minimum of about 45 m/s (150 ft/s). The peak velocity is about 20% higher than the mean injection velocity of 51 m/s (168 ft/s) suggesting that the  $\text{GO}_2$  velocity profile at the exit of the injector is not a "classical" fully developed turbulent profile (centerline velocity to mean velocity ratio of 1.1) [8]. The velocity profile shows the lowest velocities in the region downstream of the  $\text{GO}_2$  injector post wall (thickness of 0.89 mm (0.035 in.)). This indicates that a recirculation zone exists on the  $\text{GO}_2$  post tip; however the large LDV probe volume size prohibits its characterization. The velocity profiles in the region of  $\text{GH}_2$  flow show a very rapid increase in the mean velocity next to the  $\text{GO}_2$  region. The profiles are not exactly symmetric with respect to the centerline, with the difference in peak velocities directly attributable to the large LDV probe volume size and the unsteady nature of the flame. The measured mean peak velocities compare reasonably with the calculated mean  $\text{GH}_2$  injection velocity of 177 m/s (581 ft/s).

The radial velocity profile at the 25.4 mm (1 in.), shows that in the shadow of the central  $\text{GO}_2$  post of the injector, the mean velocity at the centerline is the same as the injection  $\text{GO}_2$  mean velocity, i.e. about 51 m/s (167 ft/s), suggesting that the core of the  $\text{GO}_2$  flow has not been affected by shear from the higher velocity  $\text{GH}_2$  flow. For velocity measurements in this central region, only the  $\text{GO}_2$  flow was seeded. The profile in the core region shows a slight reduction in the mean velocity with radial distance from the centerline, a result of the turbulent velocity profile in the central  $\text{GO}_2$  post of the injector ( $Re=3.2 \times 10^5$  for the  $\text{GO}_2$  flow). For increasing radial distance in both directions, the mean velocity increases to a peak of about 120 m/s (394 ft/s), and then decreases. For velocity measurements in this outer region, only the  $\text{GH}_2$  flow was seeded. The peak velocity is significantly lower than the injection  $\text{GH}_2$  mean velocity (177 m/s) and occurs radially outward from the shadow of the injector's annulus, suggesting that the  $\text{GH}_2$  flow is diffusing with radial distance and mixing with both  $\text{GO}_2$  and the net outward mass flux of the combustion product, gaseous  $\text{H}_2\text{O}$ . Clearly, these measurements have to be

complemented by species measurements of  $H_2$ ,  $O_2$  and  $H_2O$ , and temperature measurements to obtain a complete understanding of this complex combusting flowfield.

Further inspection of the velocity profile at the 25.4 mm (1 in.) location also shows that in the mixing layer between the two flows, the measured mean velocity at a point differs depending on which flow was seeded. This is a reflection of the unsteady nature of the flame front and will be discussed later. The maximum radial distance to which the seed particles penetrated was about 15 mm (0.59 in.) from the centerline, which is considerably less than the chamber wall location at 25.4 mm (1 in.) from the centerline. There is a recirculation zone in this outer wall region which could not be measured because of a lack of seed particles. Also, because of geometric constraints associated with the positioning of the LDV optics at a  $15^\circ$  angle, only a portion of the chamber could be traversed in the positive radial direction corresponding to a maximum  $r$  of 10 mm. However, the full chamber height could be examined in the negative radial direction subject to seeding constraints.

The radial velocity profile at the next axial measurement location, 50.8 mm (2 in.), shows that the mean velocity in the central core is still the same as the injection  $GO_2$  mean velocity, i.e. about 51 m/s (167 ft/s); however, here the velocity profile is more uniform suggesting that the wall effects on the turbulent velocity profile from the central  $GO_2$  tube have relaxed with axial distance. Away from the central core, the mean velocity peaks at a maximum of about 80 m/s (262 ft/s) at a greater radial location than for the 25.4 mm (1 in.) axial measurement location, and then decreases with radial distance. Mean velocities were measured radially up to about 20 mm (0.79 in.) showing that the flowfield expands with axial distance. Photographs of the visible flame front at this location also show that the front extends to a greater radial distance. The recirculation zone probably still exists at this measurement location. In terms of seeding, seed in the  $GH_2$  flow was sufficient for making mean velocity measurements in the shadow of the central tube. The seed particles can be viewed to represent a passive scalar [9], i.e. the  $GH_2$  flow seeding marks locations where hydrogen is present either as  $H_2$  or  $H_2O$ , the combustion product. This indicates that at this axial measurement location, hydrogen in the form of reactant  $GH_2$  or product, gaseous  $H_2O$  is present in the central regions of the flowfield. Conversely, radial locations where velocity measurements are made by just seeding the  $GO_2$  flow marks the presence of either  $GO_2$  or gaseous  $H_2O$ . The radial extent of velocity measurements for only

GO<sub>2</sub> seeding was stopped when the data rate became low, therefore, the radial extent of oxygen can not be correctly demarcated by the measurements shown in the figure.

The last velocity profile shown in Fig. 3.17 is for the 127 mm (5 in.) axial position. Here, the velocity in the central core is still about the same as the mean GO<sub>2</sub> injection velocity. However, unlike the velocity profiles at the other two axial measurement locations, the peak velocity is maximum at the centerline and relaxes with radial distance. Velocity measurements were made at radial locations close to the wall indicating that the recirculation zone does not exist at this measurement location. Near the wall, the velocity profile shows a small increase from 25 m/s (82 ft/s) at a radial distance of -21 mm (0.83 in.) to almost 30 m/s (98 ft/s) at the next radial location. This is probably due to the nitrogen (GN<sub>2</sub>) purge flow at the bottom of the combustion chamber for the slot windows. Note that the entire velocity profile was measured by just seeding the GH<sub>2</sub> flow. Finally, based on the total flow rate and rocket chamber geometry, the mean chamber velocity is calculated to be 40 m/s (131 ft/s). The velocity measurements at the furthest radial location approach the calculated mean chamber velocity. No velocity measurements were made further downstream, but it is expected that with axial distance, the velocity profile across the chamber becomes uniform.

The corresponding root mean square (RMS) velocity profile at the closest axial location of 12.7 mm (0.5 in.) is shown in Fig. 3.16 (b). In the GO<sub>2</sub> region, the RMS velocity is constant across the profile. In the GH<sub>2</sub> region, the local turbulent intensity (RMS velocity/mean velocity) gets as high as 50%. It is noted that this high intensity level may be largely due to the large probe volume size and unsteady nature of the flame, and not due to high turbulence levels in the GH<sub>2</sub> flow exiting the annulus of the injector. From these measurements, it is clear that any modeling of the flowfield has to include the unsteadiness of the flowfield since steady flow assumptions simply neglect the major physical mechanisms of the flowfield. The RMS velocities are plotted for the remaining three axial stations in Fig. 3.18. In the central core, the root mean square velocity is about 6 m/s at all these axial measurement locations yielding a turbulent intensity value of about 0.1, or 10%. Fully developed pipe flow turbulent intensities are about 0.05, or 5% [8], indicating that the incoming flow has a higher turbulent energy content and/or the combustion enhances the turbulence levels. In the peak velocity region at the 25.4 mm (1 in.) measurement location, the mean velocity is about 120 m/s (394 ft/s) with a corresponding root mean square velocity of about 30 m/s (98 ft/s) resulting in a turbulent

intensity of about 0.25 or 25%. The higher turbulent intensity value here is probably a result of both combustion and the unsteady nature of the flow. A similar value of turbulent intensity is also obtained for the peak velocity region at the next axial location (mean velocity and RMS velocity are 80 m/s (262 ft/s) and 20 m/s (66 ft/s), respectively). The level of turbulence intensity (i.e. 25%) observed in the peak velocity region is similar to those reported for turbulent hydrogen/air diffusion flames [10,11]. At the outer regions of the furthest axial measurement location, both the mean velocity and the RMS velocity drop off in comparison to the other measurement locations; however, the rate of drop off is significantly higher for the mean velocity, resulting in a turbulent intensity of about 0.4 or 40% (mean velocity and RMS velocity are 25 m/s (82 ft/s) and 10 m/s (33 ft/s), respectively).

Images were also taken with the CCD camera of just the scattered light from the seed particles inside the rocket chamber under conditions in which only the  $\text{GO}_2$  flow was seeded (see next section for details). These images of scattered light from the seed particles at the near injector location clearly show that the oxygen region does not have smooth edges, but is characterized by irregular protuberances. This suggests that the mixing region is characterized by large scale turbulent structures that seem to eject from the central oxygen rich region in a manner analogous to bursts in the near wall region of a turbulent boundary layer. Single point velocity measurements in this type of mixing layer will therefore vary depending on the seeding method, i.e. seed in  $\text{GH}_2$  or  $\text{GO}_2$  flow, and is observed to be true for the velocity profile measurements described earlier. Similar observations regarding the effects of seeding on velocity measurements have been reported for turbulent diffusion flame studies [12].

### 3.3.4 Mixing Study Results

Multiple (~ 100) instantaneous planar images of light scattered from particles individually seeded into the  $\text{GO}_2$  and  $\text{GH}_2$  flows were obtained downstream of the injector face. The images were first corrected by subtracting a background image. They were then corrected for intensity variations across the laser sheet. Finally, the images were normalized with respect to the intensity near the injector exit where the gas properties are known. For the  $\text{GH}_2$  seeded flow, the normalized intensity,  $f_F$ , relates scattered light intensity,  $I$ , to density,  $\rho$ , and mixture fraction,  $\xi$ , by the following relation:

$$f_F = \frac{I}{I_F^o} = \frac{\rho \xi}{\rho_F^o \xi_F^o} \quad (\text{Equation 3.4})$$

where  $I_F^o$ ,  $\rho_F^o$ , and  $\xi_F^o$  are intensity, density, and mixture fraction at the fuel annulus exit. Mixture fraction is defined here as the mass fraction of fluid from the fuel stream. Therefore at the annulus exit, by definition,  $\xi_F^o$  is equal to one.

In a similar manner, for the  $\text{GO}_2$  seeded flow, the following relation is obtained:

$$f_o = \frac{I}{I_o^o} = \frac{\rho(1-\xi)}{\rho_o^o(1-\xi_o^o)} \quad (\text{Equation 3.5})$$

where  $I_o^o$ ,  $\rho_o^o$ , and  $\xi_o^o$  are intensity, density, and mixture fraction at the oxygen post exit where  $\xi_o^o$  by definition is equal to zero.

The image shown in Fig. 3.19 is a typical single shot image of the  $\text{GO}_2$  seeded flow. The injector is at the left edge of the image and flow is from left to right. The image has been corrected for laser intensity variations. The dark areas in this image represent locations where  $\rho(1-\xi)/\rho_o^o$  is high and can be considered as the "mole fraction of injector fluid" [13]. The images clearly show that the  $\text{GO}_2$  region does not have smooth edges, but is characterized by irregular protuberances.

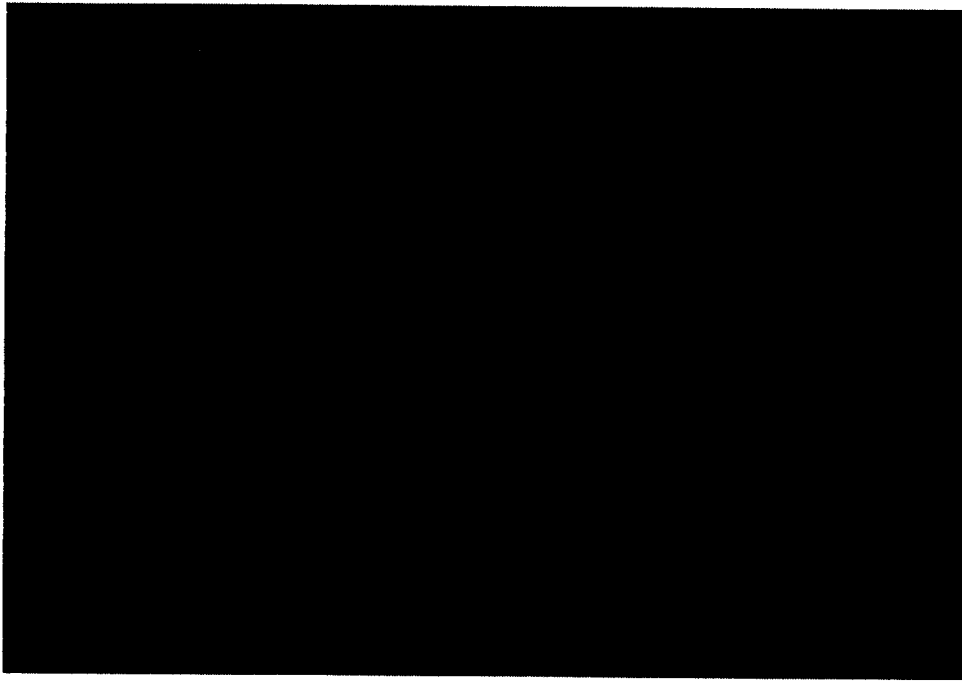


**Fig. 3.19. Instantaneous image of scattered light from particles seeded in the  $\text{GO}_2$  stream. Field of view is from the injector face to 45.7 mm downstream. The seeded region is indicated by the dark regions of the image.**



**Fig. 3.20. Average of 105 scattered light images from particles seeded in the  $\text{GO}_2$  stream. Field of view is from the injector face to 45.7 mm downstream. Hexagonal structures are an artifact of camera intensifier.**

The corrected images from multiple laser pulses and several rocket firings were averaged together. The result of averaging 105 images of the  $\text{GO}_2$  seeded flow is shown in Fig. 3.20. Fig. 3.21 shows the result of averaging 120 images with the  $\text{GH}_2$  flow seeded. Note that the hexagonal structures in these images are an artifact of the camera intensifier. Each of the images represents the "mole fraction" of fluid for the  $\text{GO}_2$  and  $\text{GH}_2$  streams, respectively. When the two images are combined, the result, shown in Fig. 3.22, is the "mole fraction" of the total injected



**Fig. 3.21. Average of 120 scattered light images from particles seeded in the  $\text{GH}_2$  stream. Field of view is from the injector face to 45.7 mm downstream. Hexagonal structures are an artifact of camera intensifier.**



**Fig. 3.22. Overlay of averaged images shown in Figs. 3.20 and 3.21. Hexagonal structures are an artifact of camera intensifier.**

fluid. The light areas are regions of low mole fraction as a result of high temperatures in the reaction zone.

The mean values  $\overline{\rho\xi}$  and  $\overline{\rho(1-\xi)}$  can be obtained by multiplying the respective images of  $\overline{f_F}$  and  $\overline{f_O}$  by the corresponding density at the injector exit,  $\rho^o$ . The results can be combined to obtain the average local density as following:

$$\overline{\rho} = \rho_F^o \overline{f_F} + \rho_O^o \overline{f_O} = \overline{\rho\xi} + \overline{\rho(1-\xi)} \quad \text{(Equation 3.6)}$$

In a similar fashion, the Favre averaged local mixture fraction is obtained from:

$$\frac{\overline{\rho\xi}}{\overline{\rho}} = \tilde{\xi} = \frac{\rho_F^o \overline{f_F}}{(\rho_F^o \overline{f_F} + \rho_O^o \overline{f_O})} \quad \text{(Equation 3.7)}$$

The radial profile of  $\overline{\rho}$  at an axial location 25.4 mm (1 in.) downstream of the injector is shown in Fig 3.23 along with the radial density profile calculated using FLUENT [14]. The average density profiles agree reasonably well with predictions obtained using FLUENT, and suggest that at this axial location close to the injector face, the  $\text{GO}_2$  and  $\text{GH}_2$  flows are not well mixed.

If the two measurements of  $f_F$  and  $f_O$  could be performed simultaneously with a detector capable of distinguishing between the seed particle origins, then the instantaneous values of density and mixture fraction could be obtained from the following two equations [12]:

$$\rho = \rho_F f_F + \rho_O f_O \quad (\text{equation 3.8})$$

$$\xi = \frac{\rho_F f_F}{\rho_F f_F + \rho_O f_O} \quad (\text{equation 3.9})$$

Instantaneous measurements of both  $\rho$  and  $\xi$  are desirable since much more information about the flow can be derived from these data. It is currently not possible to make this simultaneous measurement, however, instantaneous values of  $\rho$  and  $\xi$  can be derived from the images of  $\rho\xi$ , obtained by seeding the  $\text{GH}_2$  flow, or  $\rho(1-\xi)$ , obtained by seeding the  $\text{GO}_2$  flow, using a function relating  $\rho$  and  $\xi$  to either  $\rho\xi$  or  $\rho(1-\xi)$ . One such function can be obtained, assuming local equilibrium, using the NASA-Lewis Chemical Equilibrium Calculations (CEC) computer program [1].

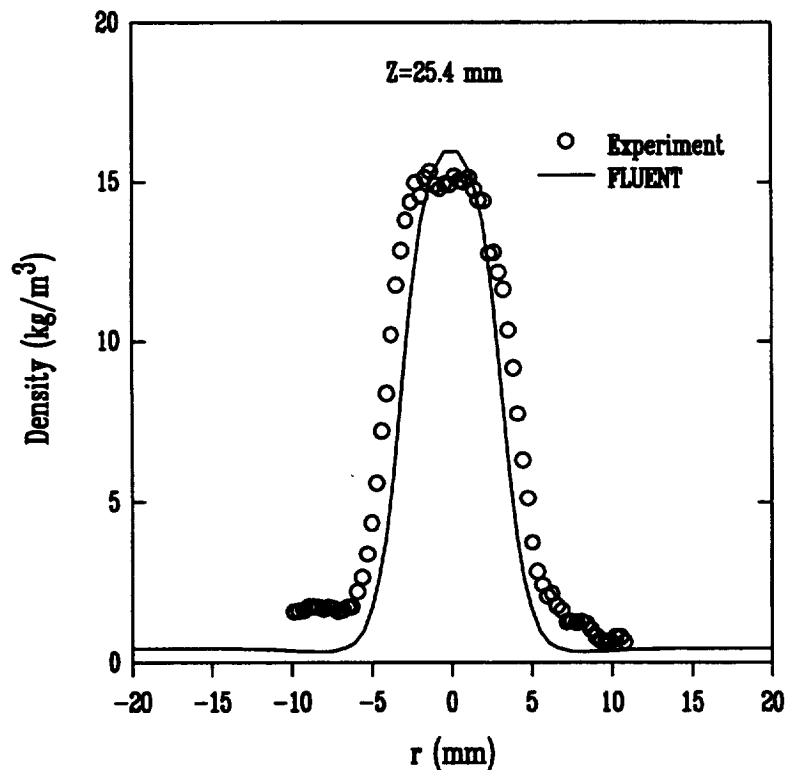


**Fig. 3.23. Density versus radial position at an axial location 25.4 mm from the injector face. Symbols represent average density derived from averaged images of  $\text{GO}_2$  and  $\text{GH}_2$  seeded flows. Line represents results calculated using FLUENT.**

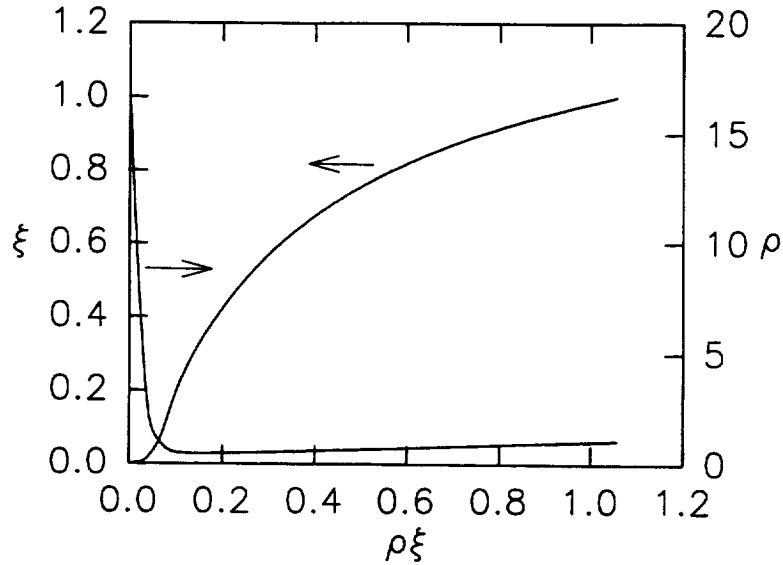


**Fig. 3.24. Relationships of  $\rho$  and  $\xi$  vs.  $\rho\xi$  calculated for adiabatic, equilibrium  $\text{GO}_2/\text{GH}_2$  combustion at 1.37 MPa.**

The two functions  $\rho$  and  $\xi$  of  $\rho\xi$  calculated using CEC for the test conditions are shown in Fig. 3.24. Both functions are monotonic and give unique values of  $\rho$  and  $\xi$  from the measured light intensity. Once obtained, conventional statistics of  $\rho$  and  $\xi$  can be derived in the normal manner. Similar functions relating temperature and species concentration to  $\rho\xi$  and  $\rho(1-\xi)$  can also be derived using the equilibrium calculations.

Each frame of the light scattered images was converted to  $\rho$  and  $\xi$  by applying the function shown in Fig 3.24 for the  $\text{GH}_2$  seeded flow and the complementary function for  $\rho(1-\xi)$  for the  $\text{GO}_2$  seeded flow. The results for average density,  $\bar{\rho}$ , and average mixture fraction,  $\bar{\xi}$ , along with the root mean square (rms) values for each quantity are shown for an axial location of 25.4 mm (1 in.) in Figs. 3.25 and 3.26, respectively. The circle symbols were derived from the  $\text{GO}_2$  seeded flow and the square symbols were derived from the  $\text{GH}_2$  seeded flow. Only the data points where the signal to noise ratio is greater than one are plotted.

In general, the curves for average density and mixture fraction have the expected shape and magnitude for both the  $\text{GO}_2$  and  $\text{GH}_2$  seeded flows. The full width at half maximum (FWHM) of the average density and mixture fraction curves is larger for the  $\text{GO}_2$  seeded flow than for the  $\text{GH}_2$  seeded flow scattered light images. This observation will be discussed below, since both seeding conditions should yield the same average density and mixture fraction profiles. The RMS of both the density and mixture fraction fields are relatively large as a result of both the highly turbulent

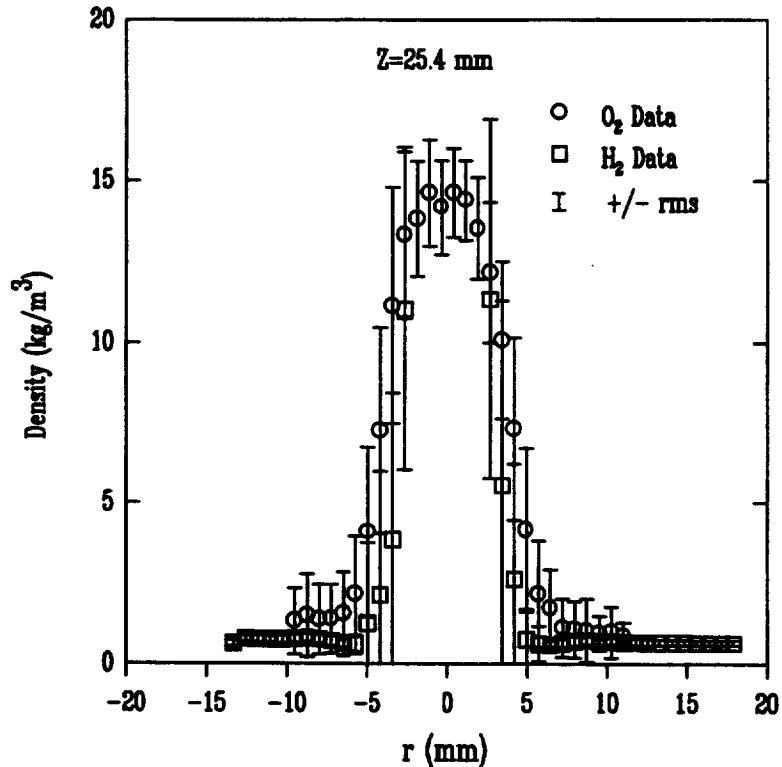


**Fig. 3.25 Density vs. radial position as derived from the scattered light measurements at an axial location of 25.4 mm.**

and unsteady nature of the high Reynolds number flowfield for both the  $\text{GO}_2$  and  $\text{GH}_2$  streams. Similar conclusions were arrived in an earlier velocity field characterization study of the same flowfield [15].

In contrast to the highly accurate quantitative flowfield characterization results reported by earlier researchers [9, 12, 16], the difference in average density and mixture fraction results between those obtained for  $\text{GO}_2$  seeding versus  $\text{GH}_2$  seeding as shown in Figs. 3.25 and 3.26 is troublesome in terms of defining the quantitative measurement capability of the planar LLS technique for rocket flowfield characterization. In assessing the diagnostic technique, the following were identified as candidate reasons for the noted discrepancy, 1) inaccuracies in the background level measurements stemming from seed particle accumulation on the window surfaces and time varying seeding rates, 2) the inability of the seed to follow the respective flows, 3) seed particle size change due to agglomeration or breakup and 4) seed particle index of refraction change due to temperature or phase change.

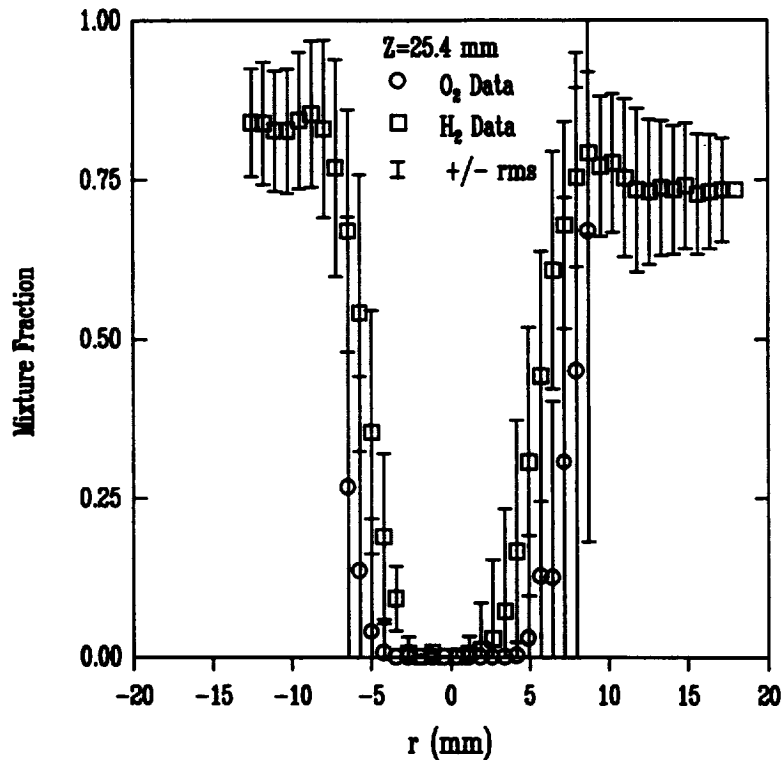


**Fig. 3.26. Mixture vs. radial position as fraction derived from the scattered light measurements at an axial location of 25.4 mm.**

The inaccuracies in background level measurements can easily explain the noted difference in average density and mixture fraction results obtained for the two seeded flows. A parametric study shows that because of the different sensitivities of the function relating  $\rho$  and  $\xi$  to  $\rho\xi$  and  $\rho(1-\xi)$ , a low error percentage in the background level (say 10%) would change the average density and mixture fraction results derived from the GH<sub>2</sub> seeded flow data an order of magnitude more than that for similar results derived from GO<sub>2</sub> seeded data. Errors in background level measurement at the 10% level can easily be realized due to window surface contamination due to seed particles and time varying seeding rates. Clearly, this parametric study shows that the confidence level for the average density and mixture fraction results obtained from the GO<sub>2</sub> seeded data is higher than for similar results from the GH<sub>2</sub> seeded data. Also, seeding of the annular GH<sub>2</sub> stream invariably contaminated the window surfaces more frequently than GO<sub>2</sub> seeding.

### 3.3.5 Raman Spectroscopy Measurements

Raman spectroscopy measurements of the major species fields were made at three axial locations, viz. 25.4, 50.8 and 127 mm (1, 2 and 5 in.) from the injector face. Note that these measurement locations correspond to the axial locations chosen for velocity field measurements (see Section 3.3.3). Examples of ten instantaneous uncorrected false-color Raman line images for  $\text{GO}_2$ ,  $\text{GH}_2$  and  $\text{H}_2\text{O}$  species ( $\text{GN}_2$  not shown) at an axial location of 25.4 mm (1 in.) from the shear coaxial injector face are shown in Fig. 3.27. Note that all images on this figure are at the same axial location and that the vertical spacing is introduced only to distinguish the various measurements. In particular, each image illustrates (by color) the radial extent of species at the stated axial location at one instant of time. These instantaneous images show that at this axial station,  $\text{GO}_2$  species is present only in the region downstream of the  $\text{GO}_2$  post, whereas  $\text{GH}_2$  species diffuses considerably in the radial direction. The  $\text{H}_2\text{O}$  species is present in the shear layer between the  $\text{GO}_2$  and  $\text{GH}_2$  flows. The instantaneous images also highlight the highly turbulent

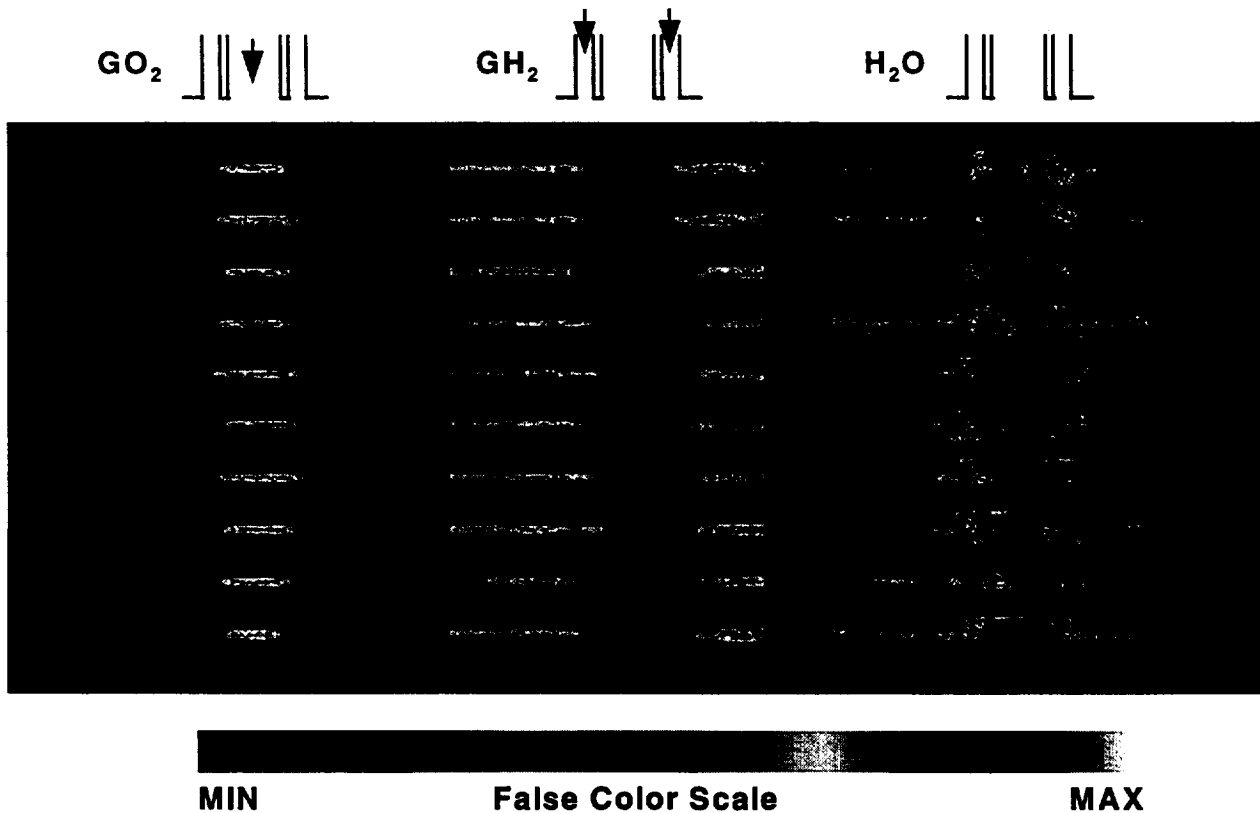


**Fig. 3.27. Multiple instantaneous uncorrected radial (32.5 mm width ) images of major species at an axial location of 25.4 mm (1 in.) from injector face. Flow is from top to bottom. Shear coaxial injector geometry is shown on top.**

nature of the combusting shear layer. Analysis of the instantaneous flow structure in the combusting flowfield was not possible because the current experimental setup provided the Raman signal from only one species at a time.

The time-averaged distributions for the three major species were obtained by averaging approximately 80 instantaneous images and correcting for flame luminosity levels and background scattering. The results for the three axial measurement stations are shown in Fig. 3.28. Note that the false-color scale for each species at each measurement station was scaled from 0 to 1, and therefore the figure should not be used to compare the relative Raman signal strength. The surprising observation from these images is that  $\text{GO}_2$  is present even at the furthest measurement location (16  $\text{GO}_2$  post diameters downstream).

To quantify the Raman spectroscopy measurements, the experimental setup was calibrated for  $\text{GO}_2$ ,  $\text{GH}_2$  and  $\text{GN}_2$  species at standard temperature and pressure conditions. A similar calibration for  $\text{H}_2\text{O}$  was obtained in a simple laboratory setup involving steam/air flow (393K). Using these calibrations, radial profiles of the major species mole fractions were extracted from the corrected/averaged Raman images. The resulting  $\text{GO}_2$  and  $\text{GH}_2$  mole fraction profiles for the three axial measurement locations are presented in Fig. 3.29. For all inset graphs in Fig. 3.29, the ordinate shows the radial distance from the centerline normalized with the  $\text{GO}_2$  post radius.

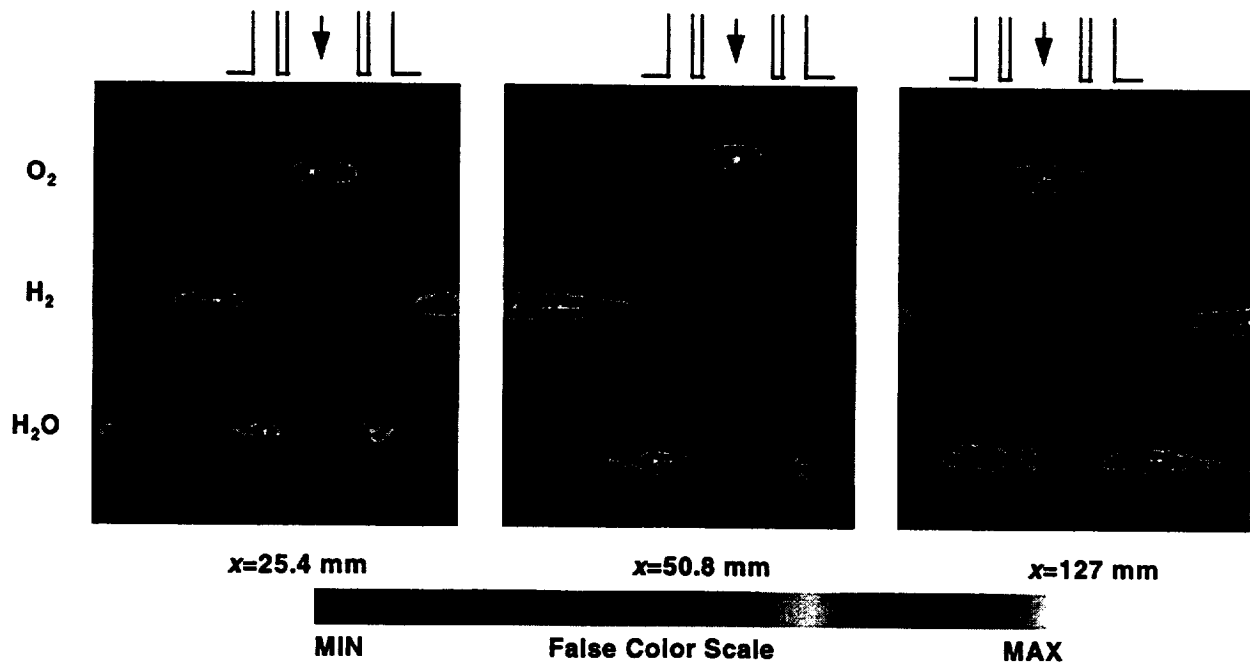
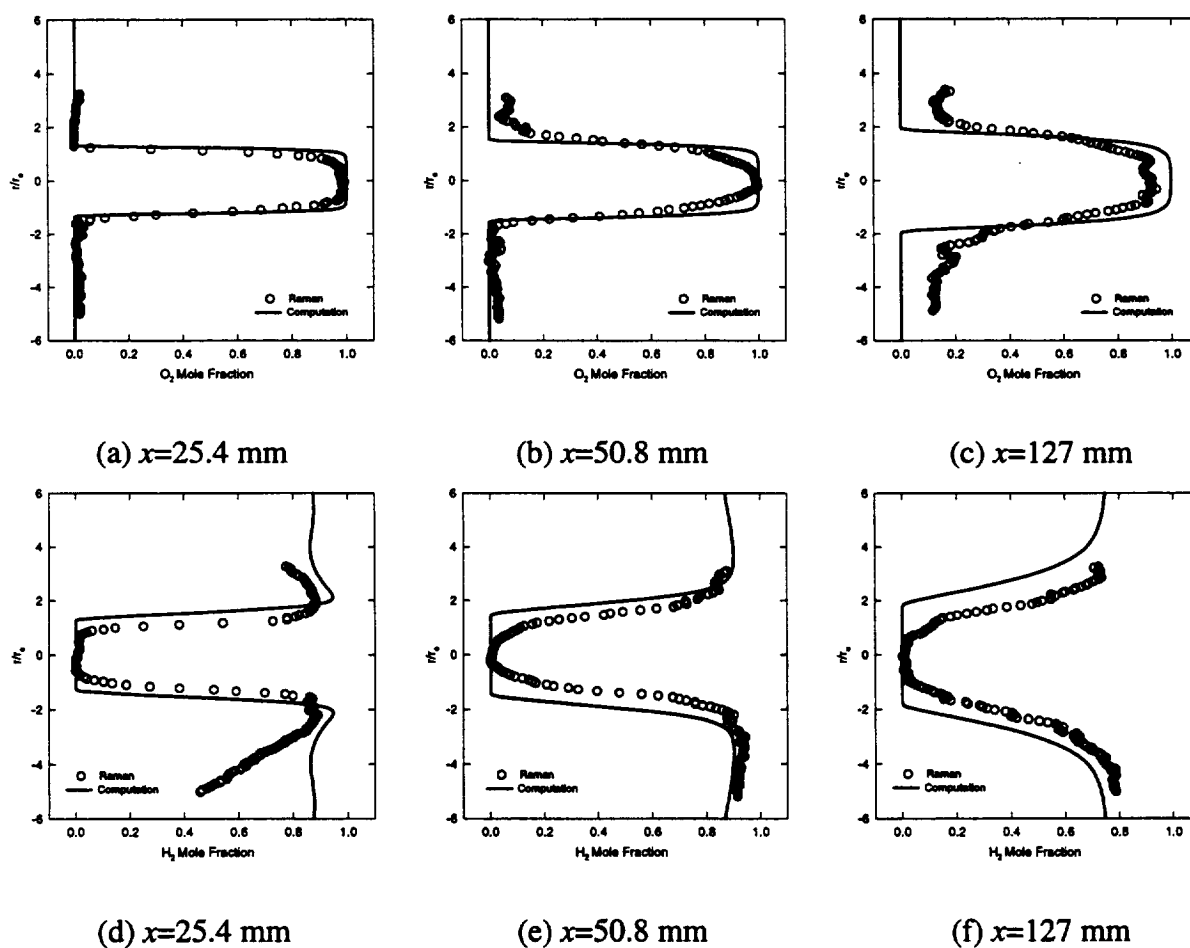


Fig. 3.28. Average corrected images of major species at all three axial measurement locations. Flow is from top to bottom. The radial width of the figure is 32.5 mm.

At the first axial measurement location,  $x=25.4$  mm, the radial profiles of  $\text{GO}_2$  and  $\text{GH}_2$  mole fraction (Fig. 3.29 (a) and (d)) show that at 3.3  $\text{GO}_2$  post diameters downstream (25.4 mm), propellant mixing and combustion is limited to the thin shear layer between the two propellant flows. The  $\text{GO}_2$  flow does not diffuse radially outward, whereas the  $\text{GH}_2$  flow does diffuse radially outward but fails to penetrate the dense  $\text{GO}_2$  central region. The  $\text{H}_2\text{O}$  mole fraction (not shown) peaks at a radial location ( $r/r_0 \approx 1.2$ ) near the intersection of the  $\text{GO}_2$  and  $\text{GH}_2$  mole fraction radial profiles. It is emphasized that the species mole fraction results are semi-quantitative since the Stokes bandwidth factor for the filters used for the experiment was temperature dependent. Note that due to the non-linear dependence of the Stokes bandwidth factor on temperature, the error in the radial profiles of species mole fraction is highest in the narrow high temperature zone corresponding to the shear layer mixing region between the two propellant streams, and minimal in other low temperature ( $<1500\text{K}$ ) regions.



**Fig. 3.29. Measured  $\text{GO}_2$  (a-c) and  $\text{GH}_2$  (d-f) mole fraction profiles for three axial locations from injector face. The measurements are compared with CFD predictions [17].**

Further downstream at an axial location of 50.8 mm from the injector face (6.6  $\text{GO}_2$  post diameters), the radial profiles of  $\text{GO}_2$  and  $\text{GH}_2$  mole fraction (Fig. 3.29 (b) and (e)) show that, as compared to the first measurement location, the mixing shear layer has radially shifted outward by a small amount. The half width at half maximum (HWHM) of the  $\text{GO}_2$  mole fraction is at  $r/r_o \approx 1.2$ , suggesting that the central  $\text{GO}_2$  flow is diffusing radially at a slow rate.

The measurements (up to 127 mm (16.4  $\text{GO}_2$  post diameters)) of the major species (and also velocity fields as discussed in Section 3.3.3) indicate that, whereas the low density annular  $\text{GH}_2$  flow rapidly diffuses radially outward to fill the chamber, the high density central  $\text{GO}_2$  flow does not diffuse significantly with downstream distance, resulting in a shear layer with low mixing efficiency as attested by the measured high  $\text{GO}_2$  mole fraction levels ( $\text{GO}_2/\text{GH}_2$  combustion products for a mixture ratio of four are  $\text{GH}_2$  and  $\text{H}_2\text{O}$ , each at a mole fraction of 0.5). However, since the  $c^*$  efficiency (see Table 1) for the rocket is very high, near complete combustion is achieved by the nozzle entrance, and hence, additional flowfield measurements between the furthest current axial station and the nozzle entrance are desirable.

## IV FLAME HOLDING STUDIES OF SHEAR COAXIAL INJECTORS

In this chapter, the results of a parametric study on injector tip flame holding are presented and discussed. These experiments were conducted to ascertain the manner in which the gaseous oxygen/gaseous hydrogen flame attaches to the tip of the shear coaxial injector for varying oxygen to hydrogen flow velocity, or momentum ratios. The major diagnostic technique that was applied was the Raman spectroscopy technique for major species ( $O_2$ ,  $H_2$  and  $H_2O$ ) measurements. The technique was not applied for making linewise measurements as discussed in the last chapter, but in a planar manner. This type of application in the injector tip region provided details on the flame holding characteristics for the injector. The gaseous oxygen post of the injector element was also instrumented with an array of thermocouples that were used for complementary temperature measurements of the injector tip.

### 4.1 EXPERIMENTAL SETUP

In this section, the injector geometry and flow conditions are discussed first. Details pertaining to the implementation of the Raman spectroscopy technique are also presented. The thermocouple instrumented injector characteristics are also discussed. Finally, the results obtained for both the injector tip temperature measurements and Raman spectroscopy characterization of the near-injector tip flowfield region are presented and discussed.

#### 4.1.1 Injector Geometry

The design of the shear coaxial injector that was used for the near-injector flowfield characterization studies incorporated a thicker-walled  $GO_2$  post that had a 7.87 mm (0.310 in.) inside diameter and a 2.41 mm (0.095 in.) wall thickness. The outer diameter of the fuel annulus was 15.2 mm (0.600 in.). This design as shown in Fig. 4.1 allowed better interpretation of the measurements since higher resolution was achieved across the injector lip as opposed to the thin-walled injector described in the last chapter. The thicker wall gaseous oxygen post design was exploited to embed thermocouples in the tip region to allow temperature measurements to be made.

Two injectors with the previously mentioned geometry were used in the flame holding studies. One injector design did not include the thermocouples within the  $GO_2$  post wall, and was used exclusively for the Raman spectroscopy experiments. The second injector design as

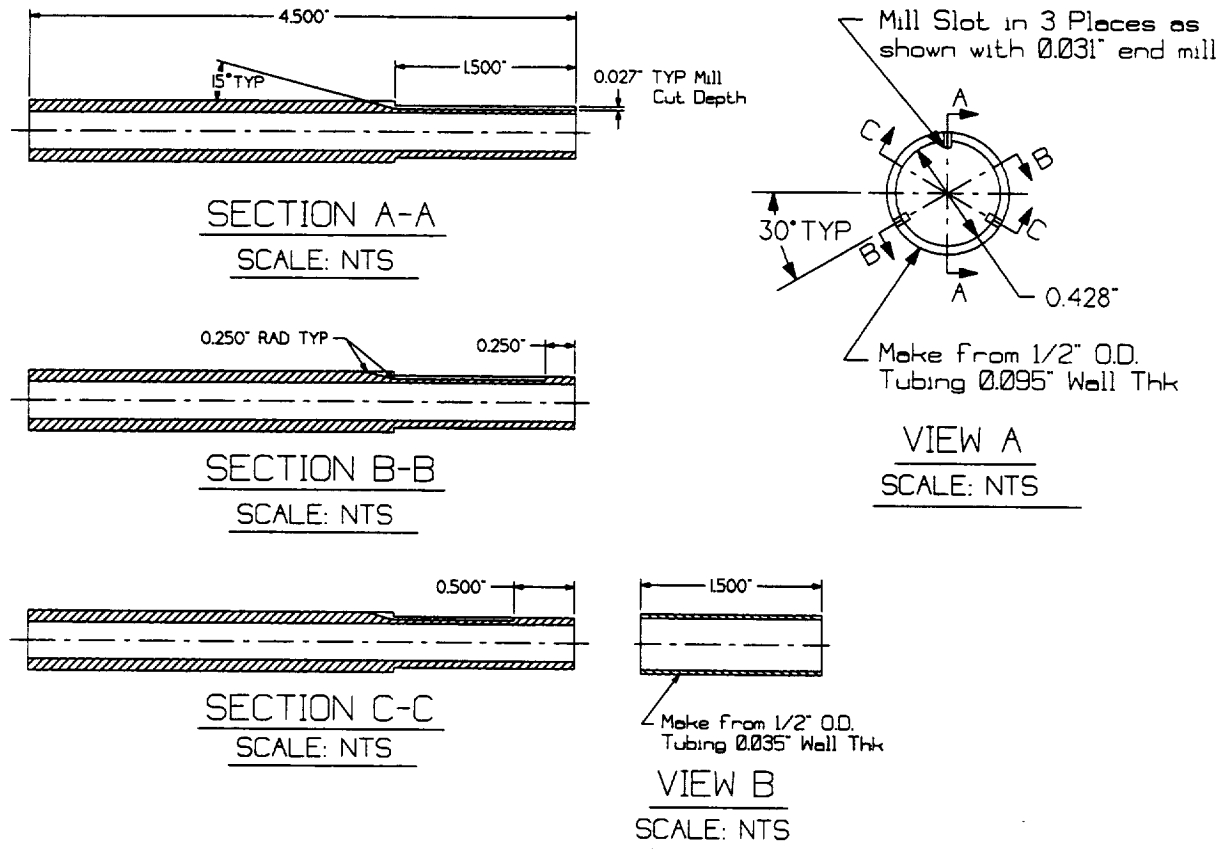


**Fig. 4.1. Detailed schematic of injector tip region of instrumented  $\text{GO}_2$  post.**

shown in Fig. 4.1 incorporated three Chromega-Alomega type thermocouples within the  $\text{GO}_2$  post wall for temperature measurements. The measurements were recorded at a sampling rate of 200 Hz. The first thermocouple was mounted right at the injector tip, whereas the other two thermocouples were recessed 6.35 mm (0.250 in.) and 12.7 mm (0.500 in.) from the injector tip, respectively.

#### 4.1.2 Flow Conditions

In these studies, the O/F ratio was varied from 1 to 50 by decreasing the  $\text{GH}_2$  mass flowrate while holding the  $\text{GO}_2$  mass flowrate nearly constant at 0.042 kg/s (0.092 lbm/s). The nominal mass flowrate of the  $\text{GN}_2$  curtain purge was constant at 0.010 kg/s (0.022 lbm/s). Note that the  $\text{GO}_2$  and  $\text{GN}_2$  mass flowrates were the same as those described in the previous chapter. Therefore, the flame holding experiments conducted at an O/F = 4 provided a complementary investigation for the previous flowfield measurements that were performed under the same rocket operating conditions. The corresponding flow conditions of the exit gases for

each of the cases being studied in the flame holding experiments are given in Table 4.1. The flow conditions in Table 4.1 show that, as the O/F increases from 1 to 50, both the velocity ratio,  $(V)_{GH_2} / (V)_{GO_2}$ , and the momentum ratio,  $(\rho V^2)_{GH_2} / (\rho V^2)_{GO_2}$ , of the gases take on values greater and less than 1. The chamber pressure for all the test cases was also held nearly constant at 1.34 MPa (194 psia).

#### 4.1.3 Raman Spectroscopy (Planar)

**Table 4.1. Flow conditions for parametric flame holding studies.**

O/F	1.03	2.02	4.06	14.1	50.6
$\dot{m}_{GO_2}$ (kg/s)	$4.22 \times 10^{-2}$	$4.34 \times 10^{-2}$	$4.25 \times 10^{-2}$	$4.06 \times 10^{-2}$	$4.10 \times 10^{-2}$
$\dot{m}_{GH_2}$ (kg/s)	$4.08 \times 10^{-2}$	$2.15 \times 10^{-2}$	$1.05 \times 10^{-2}$	$2.87 \times 10^{-3}$	$8.10 \times 10^{-4}$
$Re_{GO_2}$	$2.98 \times 10^5$	$3.14 \times 10^5$	$3.22 \times 10^5$	$2.98 \times 10^5$	$3.14 \times 10^5$
$Re_{GH_2}$	$1.87 \times 10^5$	$1.00 \times 10^5$	$5.12 \times 10^4$	$1.36 \times 10^4$	$4.00 \times 10^3$
$V_{GO_2}$ (m/s)	46.7	49.2	50.4	46.7	49.1
$V_{GH_2}$ (m/s)	632.2	338.2	173.2	45.9	13.5
$(V)_{GH_2} / (V)_{GO_2}$	13.529	6.878	3.439	0.984	0.275
$(\rho V^2)_{GH_2} / (\rho V^2)_{GO_2}$	11.541	2.983	0.746	0.061	0.005
$P_c$ (MPa)	1.44	1.40	1.33	1.38	1.33
c* efficiency (with GN2 Purge)	1.02	1.00	0.91	0.91	0.91

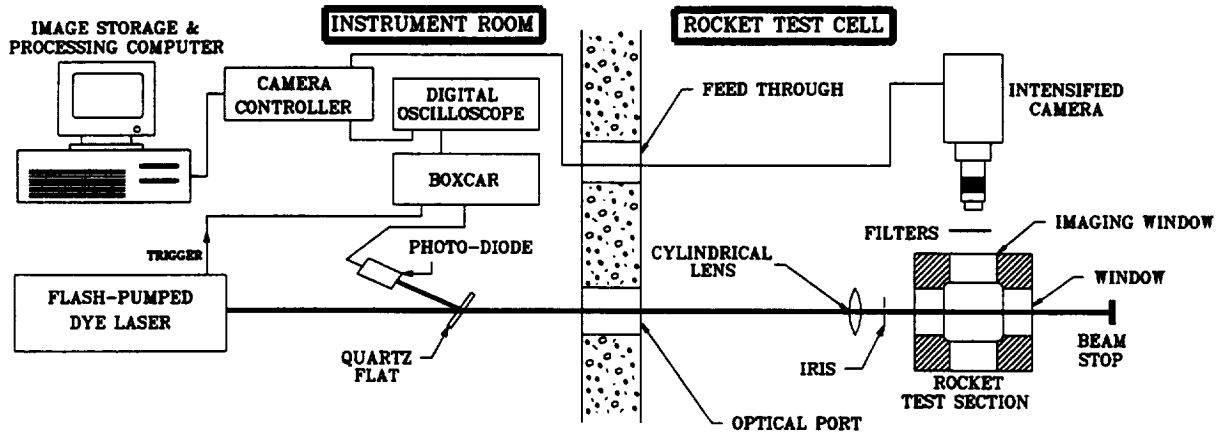


**Fig. 4.2. Experimental setup for planar Raman imaging measurements.**

The modified design of the injector required that flowfield measurements be made to ensure the species mixing fields in the rocket chamber were unaffected by the increased wall thickness of the  $\text{GO}_2$  post. These measurements were performed using the setup shown in Fig. 4.2. Improvements were made in the laser system such that a higher laser energy of 2 J could be obtained. The focused laser beam diameter for this case was nominally 0.30 mm in diameter at the centerline of the rocket chamber. For image analysis, the data was digitized using 14 bit resolution in a 4 x 4 pixel binning format of the laser beam region. The image area consisted of 144 x 15 pixels which corresponds to an image field of view of 29.7 x 2.91 mm (1.17 x 0.11 in.). This experimental configuration yielded an image magnification of 0.42 and a spatial resolution of 0.21 x 0.30 x 0.30 mm where the smallest dimension is the pixel resolution in the radial dimension of the image and the other two values stem from the diameter of the laser beam. Both the laser and the ICCD camera were operated at 10 Hz.

After performing the flowfield measurements, the apparatus shown in Fig. 4.2 was used for making planar Raman species measurements in the near-injector region of the flow. This experimental setup was similar to the previously mentioned Raman spectroscopy system shown in the last chapter with modifications that were made in order to provide close inspection of the species concentration field in the near-injector region as shown in Fig. 4.3. In the planar Raman imaging system, a 154 mm *f*<sub>l</sub> cylindrical lens was used to focus the laser beam into a laser sheet. After passing through an iris, the width of the laser sheet was 9.6 mm. The laser sheet was focused at the injector post wall within the rocket chamber. At this location, the sheet thickness was measured to be 0.30 mm. The same bandpass and long-pass cutoff filters as in the earlier described setup (see chapter 3) were used in these experiments to isolate the Raman

signals for each species measurement. For image analysis, the data was digitized using 14 bit resolution in a 2 x 2 pixel binning format. The image area consisted of 100 x 95 pixels which corresponds to an image field of view of 10.9 x 10.5 mm (0.43 x 0.41 in.) as shown in Fig. 4.3. This experimental configuration yielded an image magnification of 0.4 and a spatial resolution of 0.11 x 0.11 x 0.30 mm where the 0.11 mm dimension corresponds to the pixel resolution in the image. Both the laser and the ICCD camera were operated at 6 Hz.

## 4.2 RESULTS AND DISCUSSION

In this section, the planar Raman spectroscopy measurements of major species are presented and discussed first. This is followed by a presentation of the results of the injector tip temperature measurements.

### 4.2.1 Raman Spectroscopy Measurements

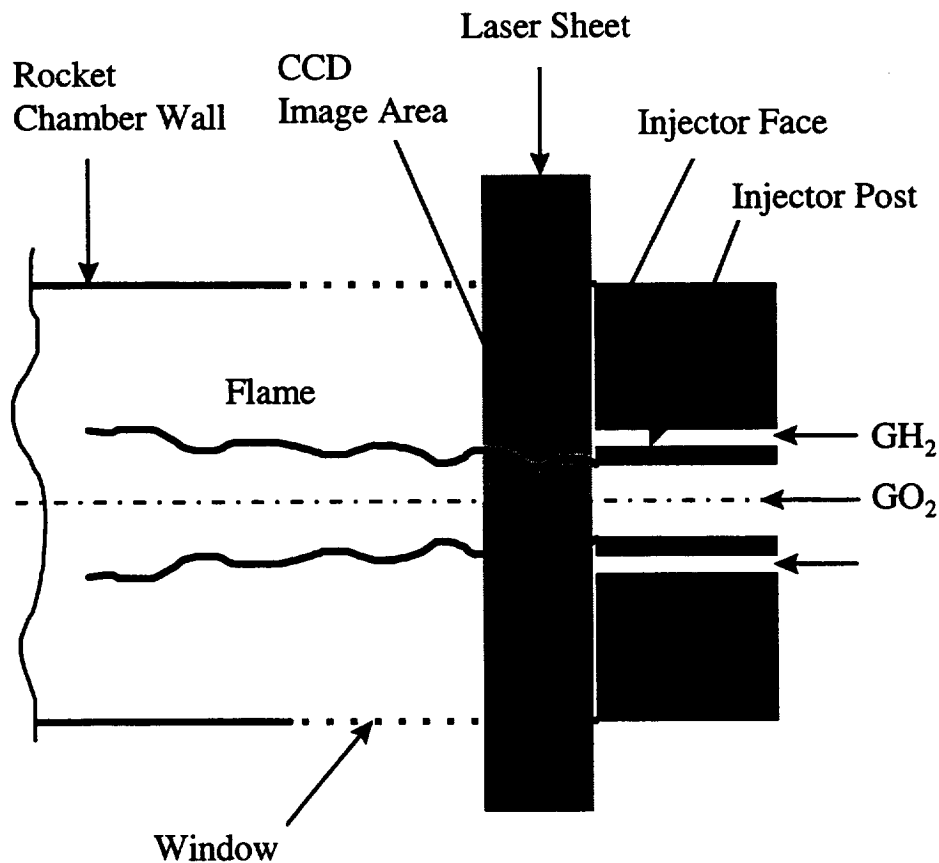
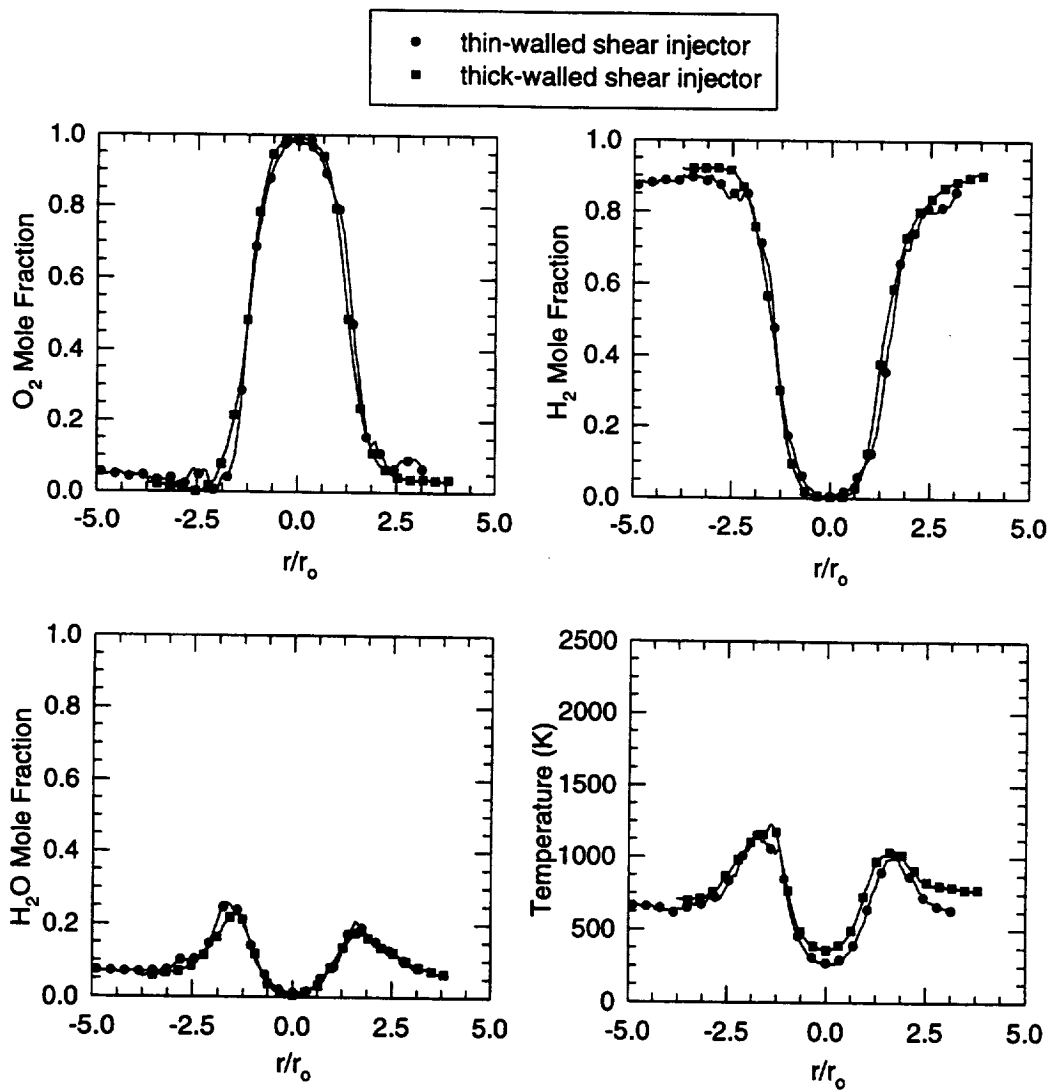


Fig. 4.3. Close-up view of near-injector flowfield region showing the recorded CCD image.

As described earlier, Raman measurements were made in the combusting flowfield downstream of the thick-walled injector post (2.41 mm wall thickness) to ensure that the physical characteristics of the flowfield were the same as those for the thin-walled injector post (results presented in last chapter). The radial profiles of major species mole fraction and temperature obtained for the thin and thick-walled injector at an axial location of 50.8 mm from the injector face are compared in Fig. 4.4. The results show that the characteristics of the combusting flowfield for the two injector designs are the same. In both cases, the *HWHM* of the  $\text{GO}_2$  mole fraction profile is  $\approx 1.2r_o$ . The  $\text{GH}_2$  species is shown to be transported rapidly to the



**Fig. 4.4. Comparisons of species mole fraction and temperature profiles for the thin and thick-walled shear coaxial injector studies conducted at an axial location of 50.8 mm from the injector.**

chamber walls with a maximum mole fraction in this outer flow region of 0.9. The peak values of the H<sub>2</sub>O mole fraction and temperature occur at the same radial location,  $\approx 1.5r_0$ . Note that the GN<sub>2</sub> purge flow was not detected in both of the injector experiments. Clearly, the species field measurements for the two injector designs indicate that the physics of the two flowfields are the same. Therefore, measurements obtained in the near-injector flowfield region using the modified injector design provide complementary results concerning flame holding mechanisms of the thin-walled shear coaxial injector.

The following discussion presents the 2-D Raman results obtained in the near-injector flowfield region for the thick-walled injector design. The near-injector region was visually observed for all the cases being studied, O/F = 1, 2, 4, 14 and 50 (see Table 4.1 for specific flow conditions), using a Nikon 8008 camera operating with a 1 ms exposure time. The O/F values span from fuel-rich to fuel-lean conditions where the stoichiometric condition is O/F = 8. The corresponding fuel to oxidizer velocity,  $(V)_{GH_2} / (V)_{GO_2}$ , and momentum ratios,  $(\rho V^2)_{GH_2} / (\rho V^2)_{GO_2}$ , range from 13.529 to 0.275 and 11.541 to 0.005, respectively. Fig. 4.5 (a-e) shows close-up photographs of the combustng flowfield from 0 to 12 mm (0 to 0.5 in.) from the injector face. These photographs clearly show that the flame is stabilized on the injector tip for all test conditions. Careful inspection of these photographs indicates that as the momentum ratio decreases from 13.529 to 0.275, the flame attachment position on the injector tip moves from being adjacent to the higher momentum GH<sub>2</sub> in the cases where the momentum ratio > 1 (O/F = 1 and 2) to being adjacent to the higher momentum GO<sub>2</sub> in the cases where the momentum ratio < 1 (O/F = 4, 14 and 50). In reviewing the change in flame position against the velocity ratio, the trend where the flame switches position on the injector tip was not observed. These photographs indicate that the relative momentum between the exit gases govern the flame anchoring position on the injector tip.

Representative instantaneous, uncorrected planar images of the Raman scattered signals from GO<sub>2</sub> and GH<sub>2</sub> (H<sub>2</sub>O and GN<sub>2</sub> not shown) in the near-injector flowfield region for the momentum ratio cases = 11.541 and 0.061 (O/F = 1 and 14) are shown in Figs. 4.6 and 4.7. Since the images for each species were obtained individually, qualitative information concerning

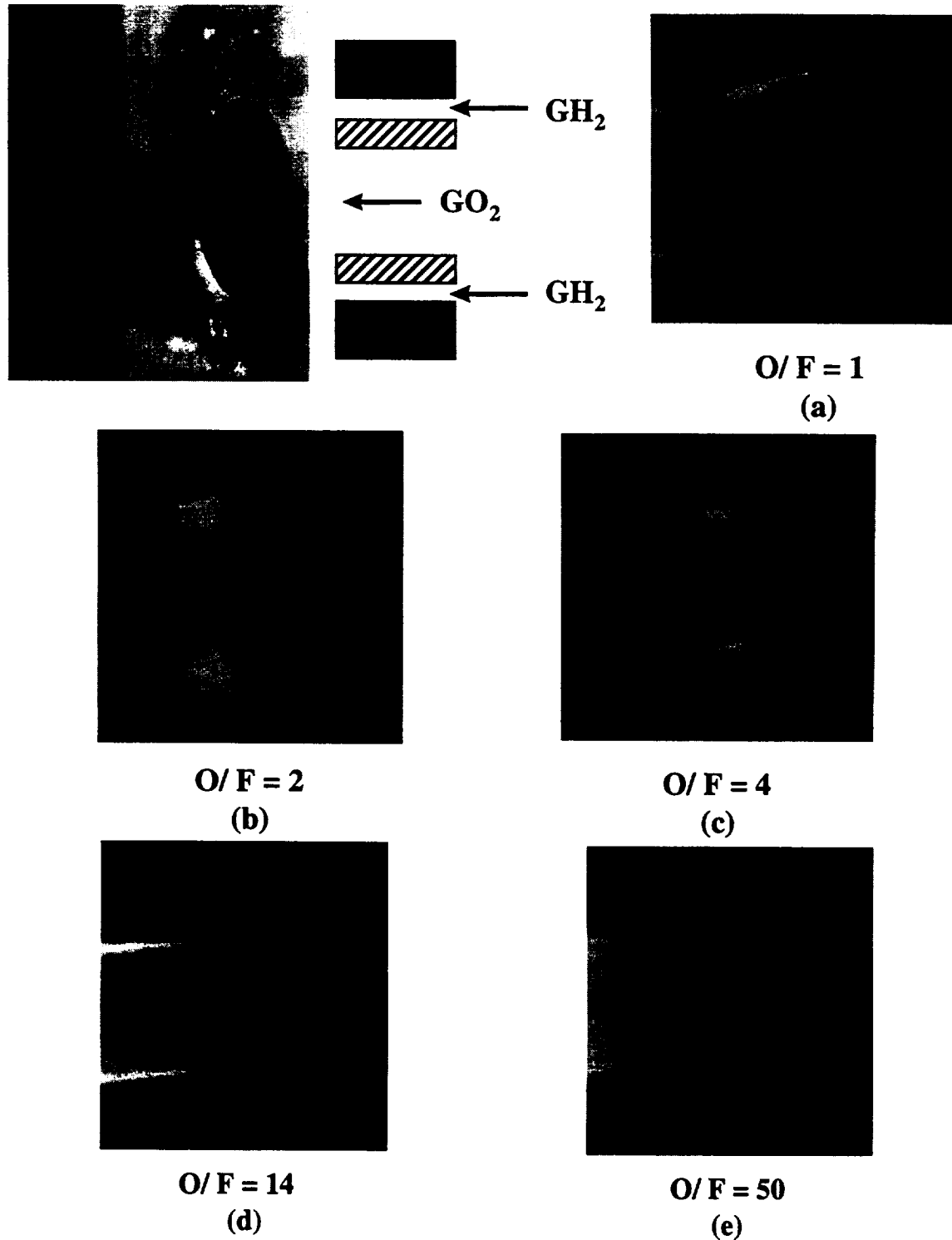


**Fig. 4.5. Close-up photograph (1 ms exposure) showing the flame attachment position on the thick-walled shear injector tip. A pictorial view of the injector is shown with the flow going right to left. Velocity and momentum ratios = (a)13.529 and 11.541, (b) 6.878, and 2.983, (c) 3.439 and 0.746, (d) 0.984 and 0.061 and (e) 0.275 and 0.005, respectively.**

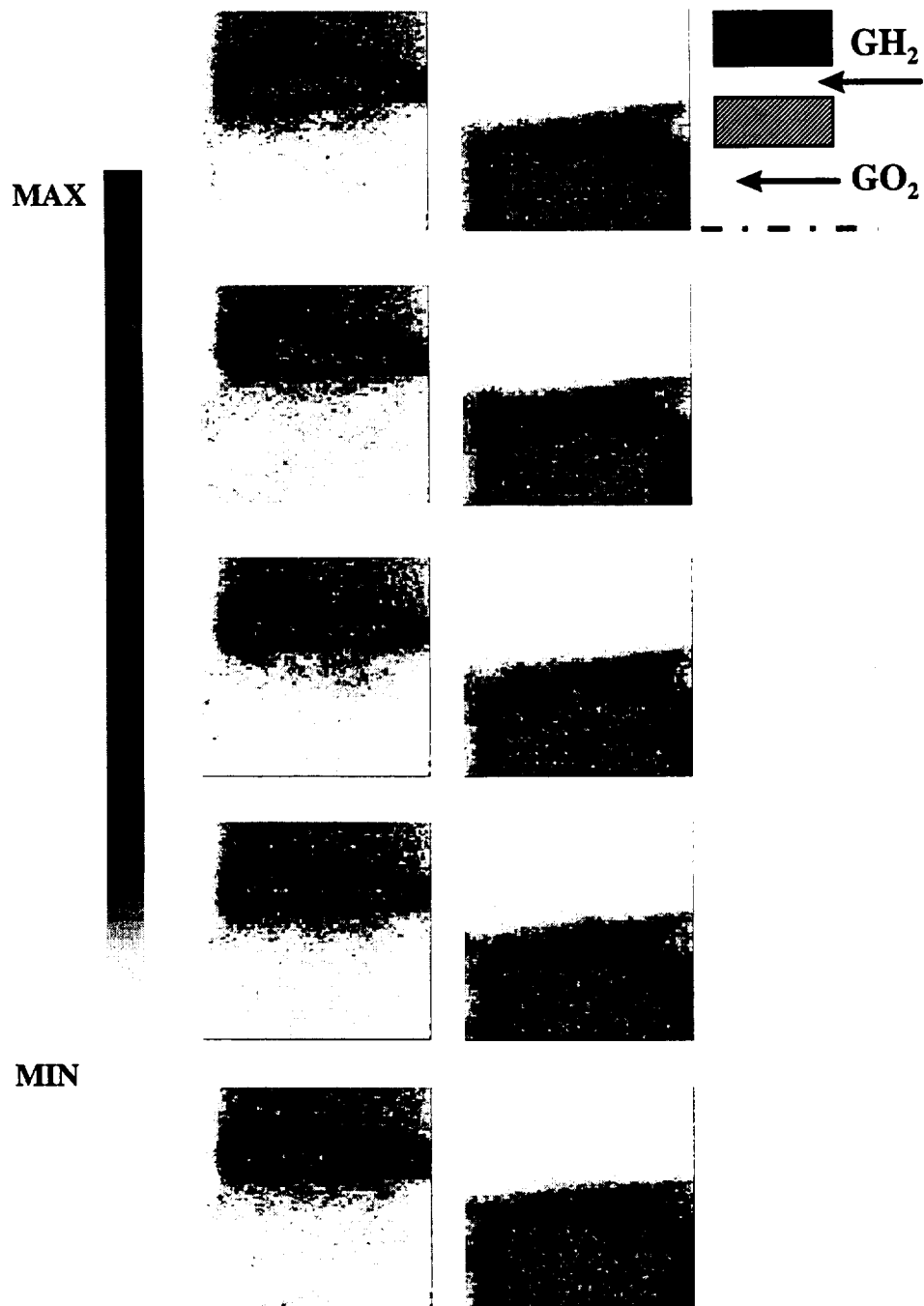


**Fig. 4.6. Multiple (5) instantaneous uncorrected planar images of  $\text{GO}_2$  and  $\text{GH}_2$  species in the near-injector flowfield region of a shear coaxial injector operating at  $\text{O/F} = 1$ . Schematic of injector is shown with the flow going right to left. Momentum ratio = 11.541.**

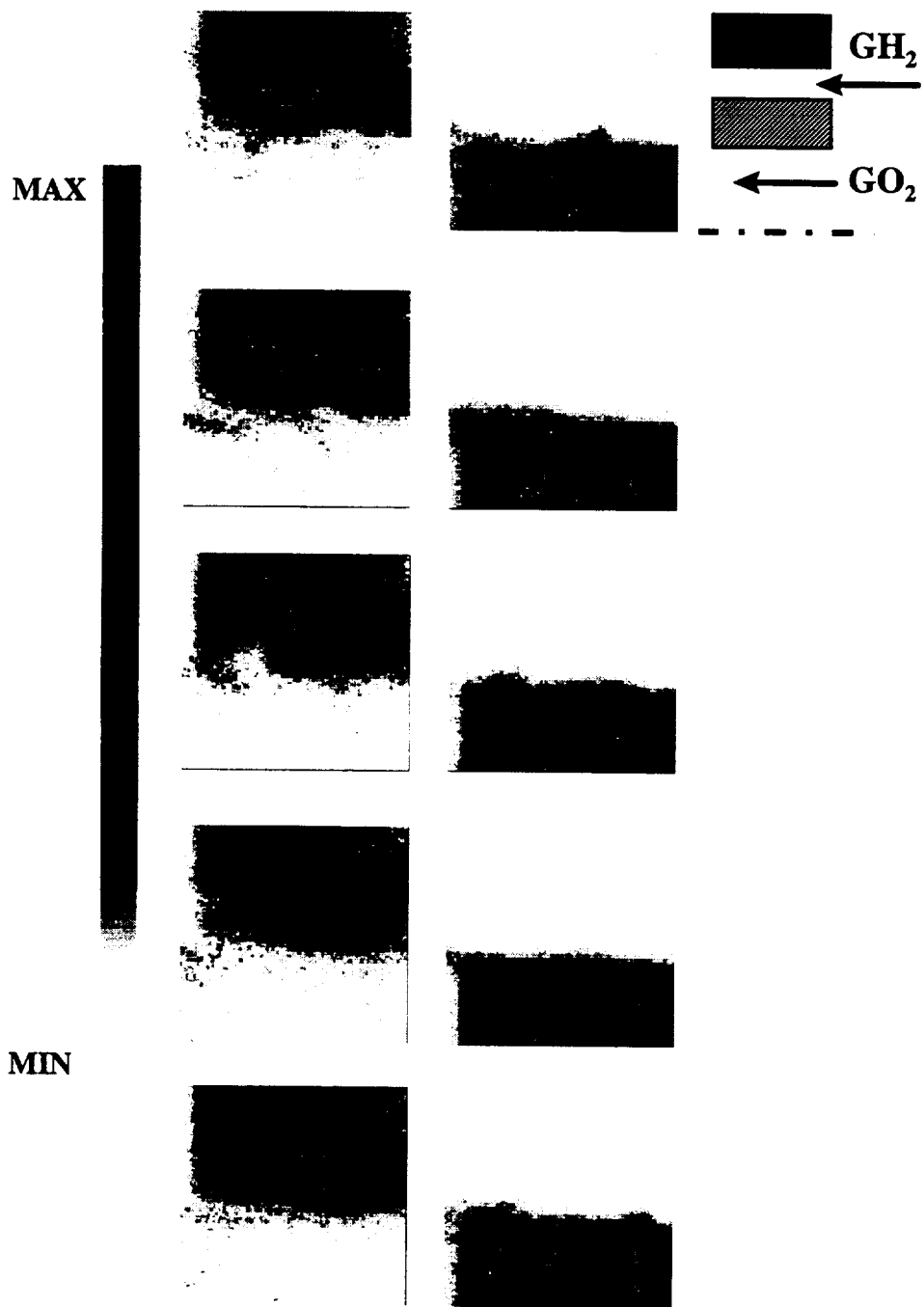


**Fig. 4.7. Multiple (5) instantaneous uncorrected planar images of  $\text{GO}_2$  and  $\text{GH}_2$  species in the near-injector flowfield region of a shear coaxial injector operating at  $O/F = 14$ . Schematic of injector is shown with the flow going right to left. Momentum ratio = 0.061.**

the flow mixing and flame attachment position is only exhibited. Also note that the highly turbulent nature of the flowfield is depicted in the shot-to-shot variation in the images. Each of these images represents a slice through half the annular flame shown in Figs. 4.6 (a) and 4.7 (a). The axial extent of the images is 0.50 to 9.57 mm (0.02 to 0.38 in.) from the injector face whereas the radial extent is 0 to 10.34 mm (0 to 0.41 in.) from the centerline of the rocket chamber. Each image illustrates by color scale the extent of the  $\text{GO}_2$  and  $\text{GH}_2$  species present in this near-injector region. In particular, the flow mixing behind the injector tip (injector base region) which controls the flame attachment position is clearly depicted in the images. The images show that for a momentum ratio = 11.541, the  $\text{GO}_2$  flow fills the injector base region while the higher momentum  $\text{GH}_2$  flow enters into the rocket chamber similar to a jet flow. For this case, the two flows mix near the side of the injector tip adjacent to the  $\text{GH}_2$  exit flow. At first glance, this implies that the flame must be anchored on the injector tip corner adjacent to the higher momentum  $\text{GH}_2$  flow. The opposite flow pattern is exhibited for a momentum ratio = 0.061. In this case, the  $\text{GH}_2$  flow fills the injector base region. Again, the two flows mix near the side of the injector tip adjacent to the higher momentum gas flow.

The Raman system calibrations described earlier provided a basis for extracting the average species mole fraction for all the test cases,  $\text{O/F} = 1, 2, 4, 14$  and 50, as shown in Figs. 4.8-4.12 (a-d) from the instantaneous images (approximately 100) collected from multiple rocket firings. Note that the single-shot images were first corrected for background flame luminosity and stray light scattering. The average temperature shown in Figs. 4.8-4.12 (e) was calculated using the average mole fraction results along with the ideal gas law. The resulting species mole fraction and temperature images consisted of 8360 points (88 x 95 pixels). The x and r axis shown in Figs. 4.8-4.12 depict the axial and radial extent of the images that was described previously for the instantaneous images. The  $\text{GO}_2$  flow passage encompasses the region from  $r = 0$  to 3.94 mm. The injector base region spans from  $r = 3.94$  to 6.35 mm. Finally, the  $\text{GH}_2$  annulus extends from  $r = 6.35$  to 7.62 mm. For the species mole fraction results, the extent of the mole fraction in the images is displayed by the color scale where light yellow is 0 and black is 1. The color scale for the temperature results is also shown, where light yellow represents 300 K and black is the maximum. Note that the maximum calculated temperature in each of the test cases is shown to vary in proportion to the  $\text{O/F}$  ratio.

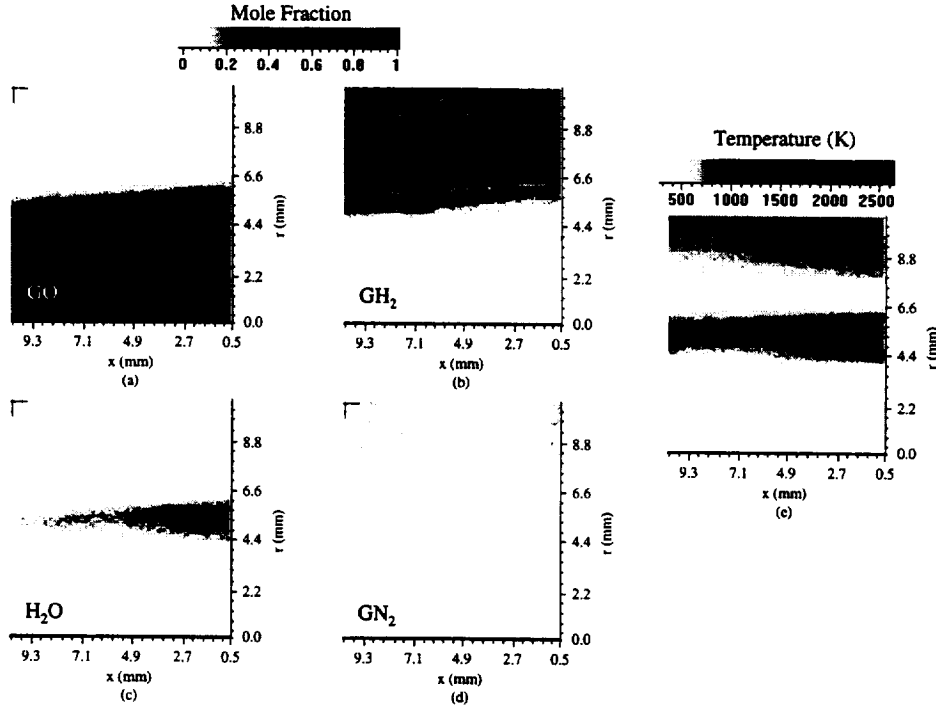


**Fig. 4.8.** Average species mole fraction and temperature in near-injector flowfield region of shear coaxial injector operating at  $O/F = 1$ , momentum ratio = 11.541. Flow is from right to left.  $x$  = axial distance from injector face,  $r$  = radial distance from centerline.

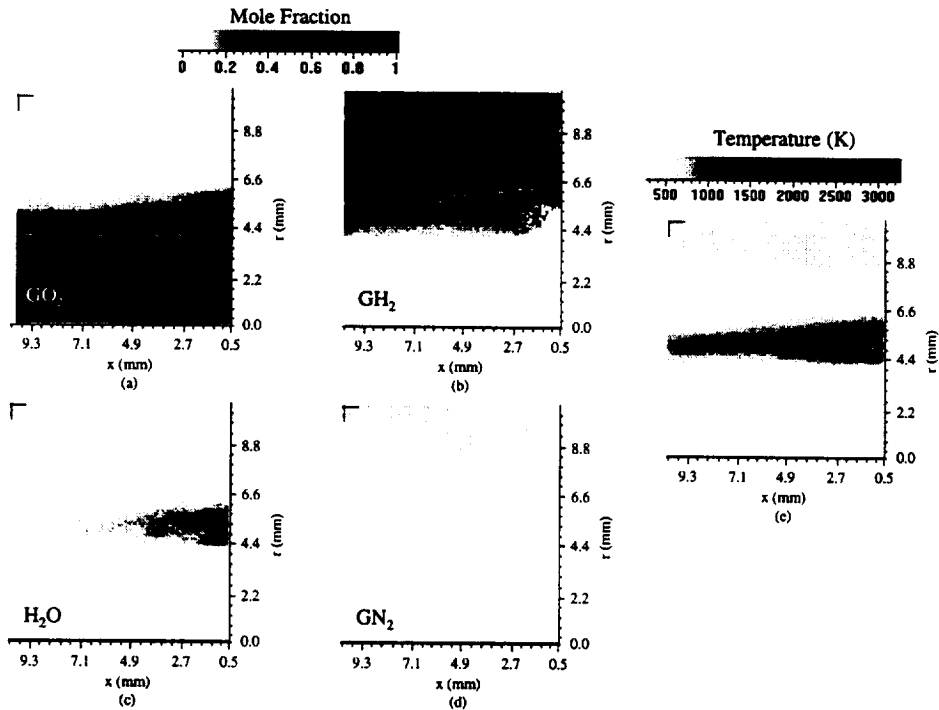


**Fig. 4.9.** Average species mole fraction and temperature in near-injector flowfield region of shear coaxial injector operating at  $O/F = 2$ , momentum ratio = 2.983. Flow is from right to left.  $x$  = axial distance from injector face,  $r$  = radial distance from centerline.

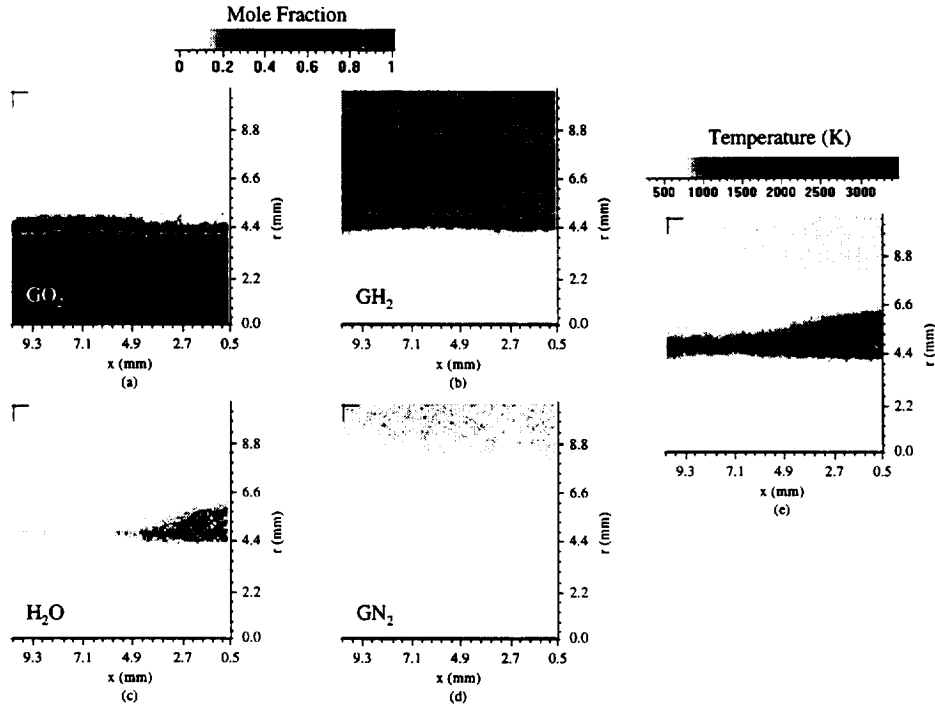


**Fig. 4.10. Average species mole fraction and temperature in near-injector flowfield region of shear coaxial injector operating at  $O/F = 4$ , momentum ratio = 0.746. Flow is from right to left.  $x$  = axial distance from injector face,  $r$  = radial distance from centerline.**

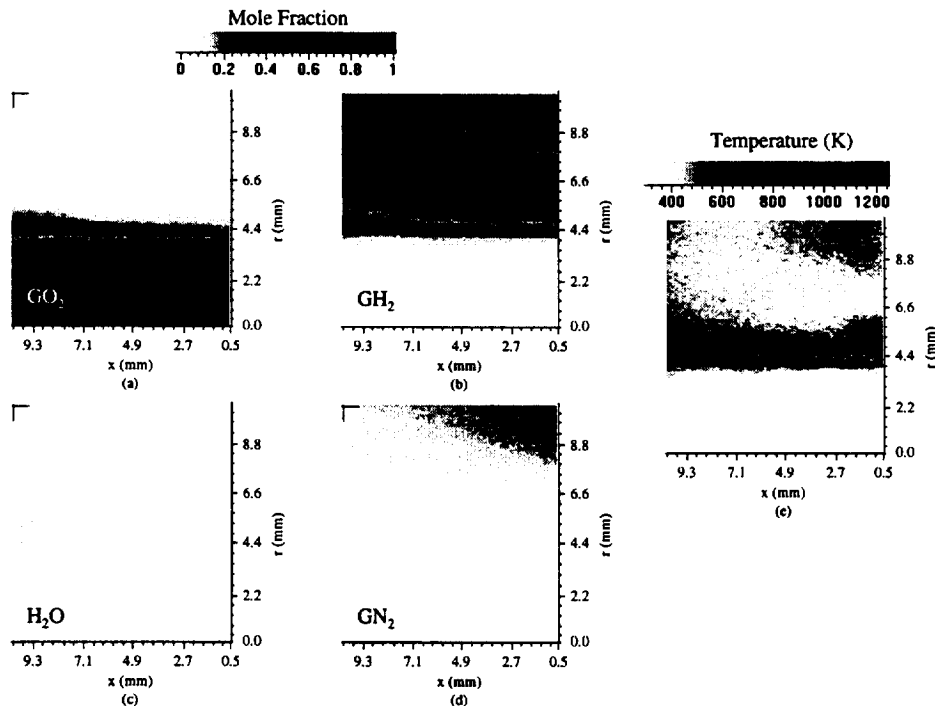


**Fig. 4.11. Average species mole fraction and temperature in near-injector flowfield region of shear coaxial injector operating at  $O/F = 14$ , momentum ratio = 0.061. Flow is from right to left.  $x$  = axial distance from injector face,  $r$  = radial distance from centerline.**

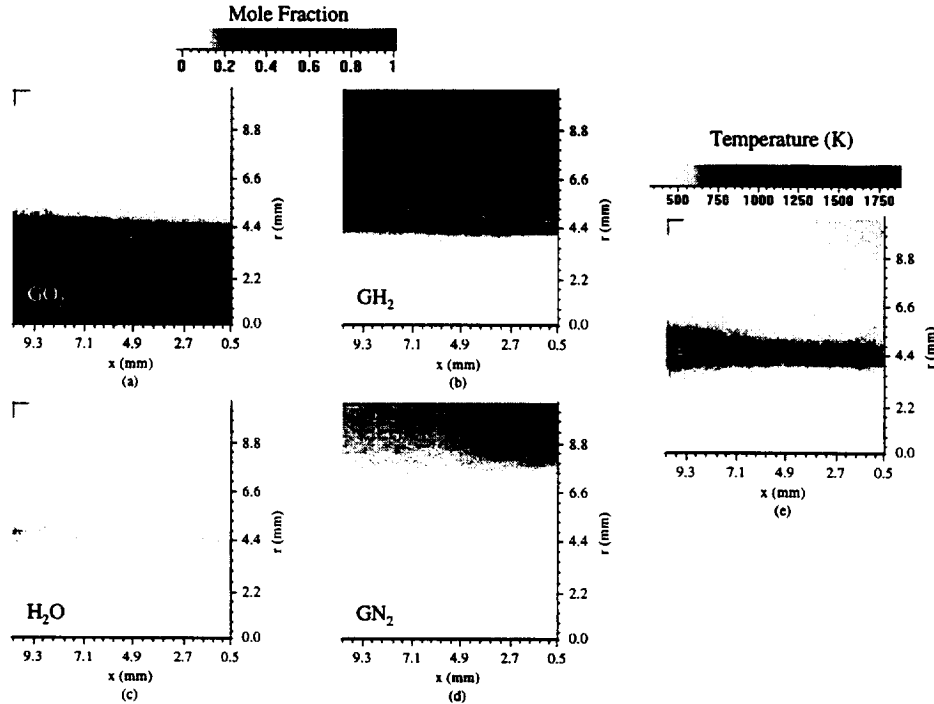


**Fig. 4.12. Average species mole fraction and temperature in near-injector flowfield region of shear coaxial injector operating at  $O/F = 50$ , momentum ratio = 0.005. Flow is from right to left.  $x$  = axial distance from injector face,  $r$  = radial distance from centerline.**

The planar species mole fraction results displayed in Figs. 4.8 and 4.9 for the momentum ratios of 11.541 and 2.983 ( $O/F = 1$  and 2) show that for these two cases, the flame is anchored near the  $GH_2$  side of the injector tip. It should be noted that the species mixing fields for these two cases were very similar. The  $GH_2$  flow is shown to enter the rocket chamber similar to a jet. The results also show that the lower momentum  $GO_2$  flow and the combustion product,  $H_2O$ , are present in the injector base region. This indicates that the  $GO_2$  must react with the  $GH_2$  flow near the  $GH_2$  side of the injector. As the  $GO_2$  and  $GH_2$  flow progress downstream, the thin reacting shear layer propagates toward the centerline. Another feature displayed in the figures is that the region from the  $GH_2$  annulus to the farthest radial measurement location is dominated by the  $GH_2$  flow with only small amounts of the  $GN_2$  purge flow being present. The  $H_2O$  mole fraction and the temperature are shown to have relatively broad profiles in the injector base region. The  $H_2O$  mole fraction peaks are  $\approx 0.4$  and  $0.6$  for the momentum ratios of 11.541 and 2.983, respectively. The corresponding temperature peaks are  $\approx 2600$  and  $3200$  K. Also note that the  $H_2O$  mole fraction and temperatures are quite low farther downstream from the injector tip.

This is mainly due to averaging over an unsteady flowfield. Nevertheless, these results indicate that the flame is anchored near the higher momentum  $\text{GH}_2$  side of the injector tip.

The species mole fraction and temperature for the momentum ratios of 0.746, 0.061 and 0.005 ( $O/F = 4, 14$  and  $50$ ) depicted in Figs. 4.10-4.12 show the counterpart for the preceding discussion. In these test cases, the momentum of the  $\text{GO}_2$  flow was larger than the  $\text{GH}_2$  flow. In the momentum ratio cases = 2.983 and 0.746, the flow mixing characteristics have changed in the injector base region as shown in Figs. 4.10-4.12. The lower momentum  $\text{GH}_2$  flow for a momentum ratio of 0.746 is shown to be present in the region behind the injector tip along with the combustion product,  $\text{H}_2\text{O}$ . This implies that for the momentum ratio = 0.746 case, the flame attachment position had shifted relative to its position in the momentum ratio = 2.983 case. The flame anchoring point for a momentum ratio = 0.746 is near the higher momentum  $\text{GO}_2$  side of the injector tip. This fact is more apparent for the momentum ratio = 0.061 and 0.005 cases. For these two cases, the reacting shear layer is much thinner than the momentum ratio = 0.746 case. The  $\text{GH}_2$  flow almost completely fills the injector base region with  $\text{H}_2\text{O}$  species being present in a narrow zone near the  $\text{GO}_2$  corner of the injector tip. The corresponding temperature results show narrow peaks that are relatively low in value. Again, this is a result of only obtaining average information from the experiments. Also note that as the  $\text{GH}_2$  momentum decreases (corresponds to decreasing momentum ratio), the effect of the  $\text{GN}_2$  purge flow in the outer flow region is more pronounced. The results of these momentum ratio cases  $< 1$  clearly show that the  $\text{GH}_2$  flows into the injector base region, thereby, reacting with the  $\text{GO}_2$  near the injector tip corner adjacent to the higher momentum  $\text{GO}_2$  flow. This fact indicates that the flame is attached near the higher momentum  $\text{GO}_2$  side of the injector tip.

The radial profiles of species mole fraction and temperature at 0.5 mm downstream from the injector face (closest axial measurement to the injector tip) for each of the test cases are shown in Figs. 4.13-4.17. In each of the figures, the abscissa shows the radial distance from the centerline normalized with the  $\text{GO}_2$  post inner radius. The  $\text{GO}_2$  flow encompasses the region from  $r/r_0 = 0$  to 1.00, where as, the injector tip extends from  $r/r_0 = 1.00$  to 1.61 and the hydrogen annulus extends from  $r/r_0 = 1.61$  to 1.94.

Representative  $\pm 1$  standard deviation precision uncertainties in the measurements are shown in Fig. 4.15 for the  $O/F = 4$  case. The experimental relative standard deviation shown in

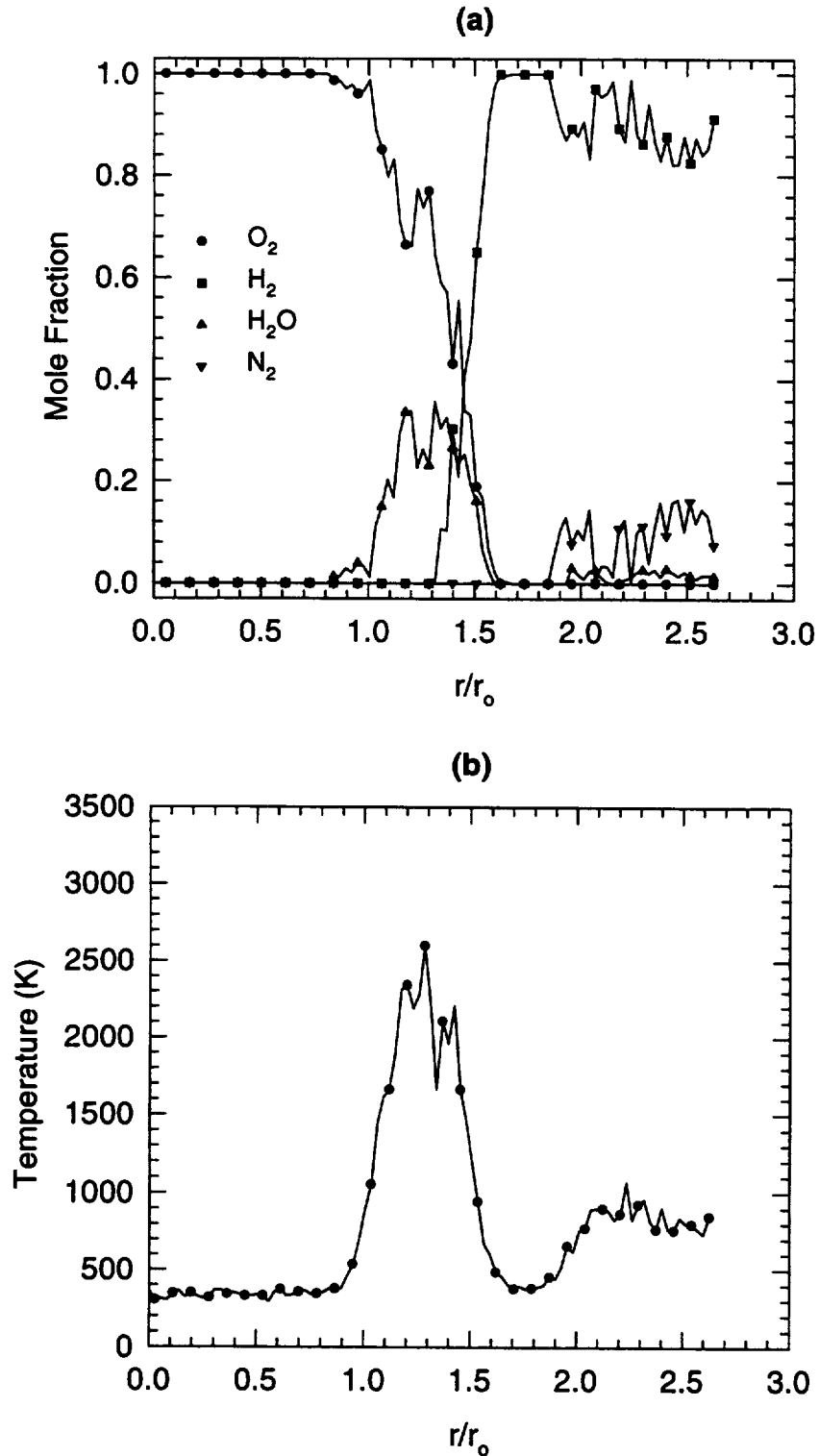


**Fig. 4.13. Radial profiles of (a) species mole fraction and (b) temperature at an axial location of 0.5 mm downstream from the thick-walled shear coaxial injector tip.  $O/F = 1$ , momentum ratio = 11.541.**

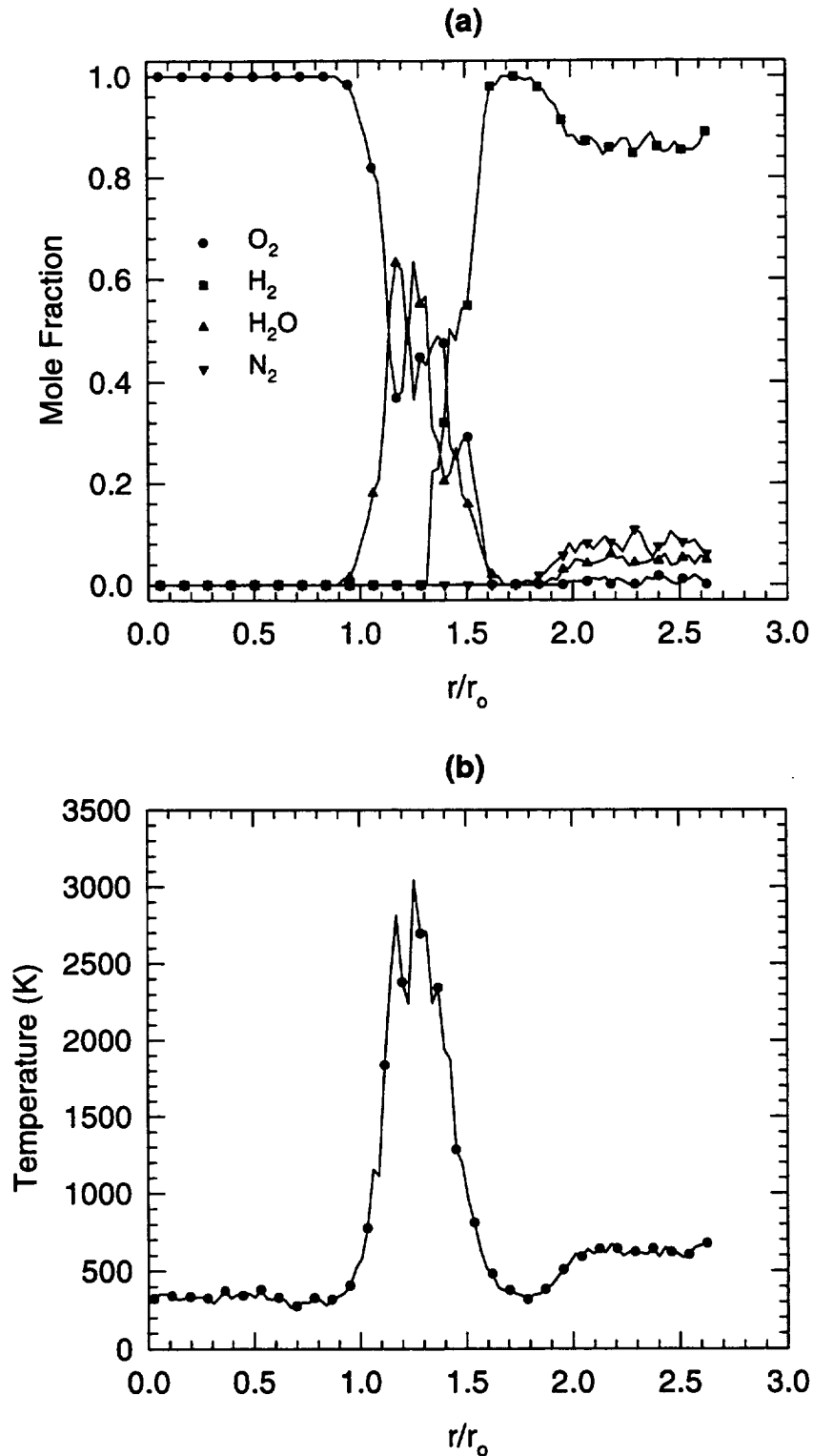


**Fig. 4.14. Radial profiles of (a) species mole fraction and (b) temperature at an axial location of 0.5 mm downstream from the thick-walled shear coaxial injector tip.  $O/F = 2$ , momentum ratio = 2.983.**

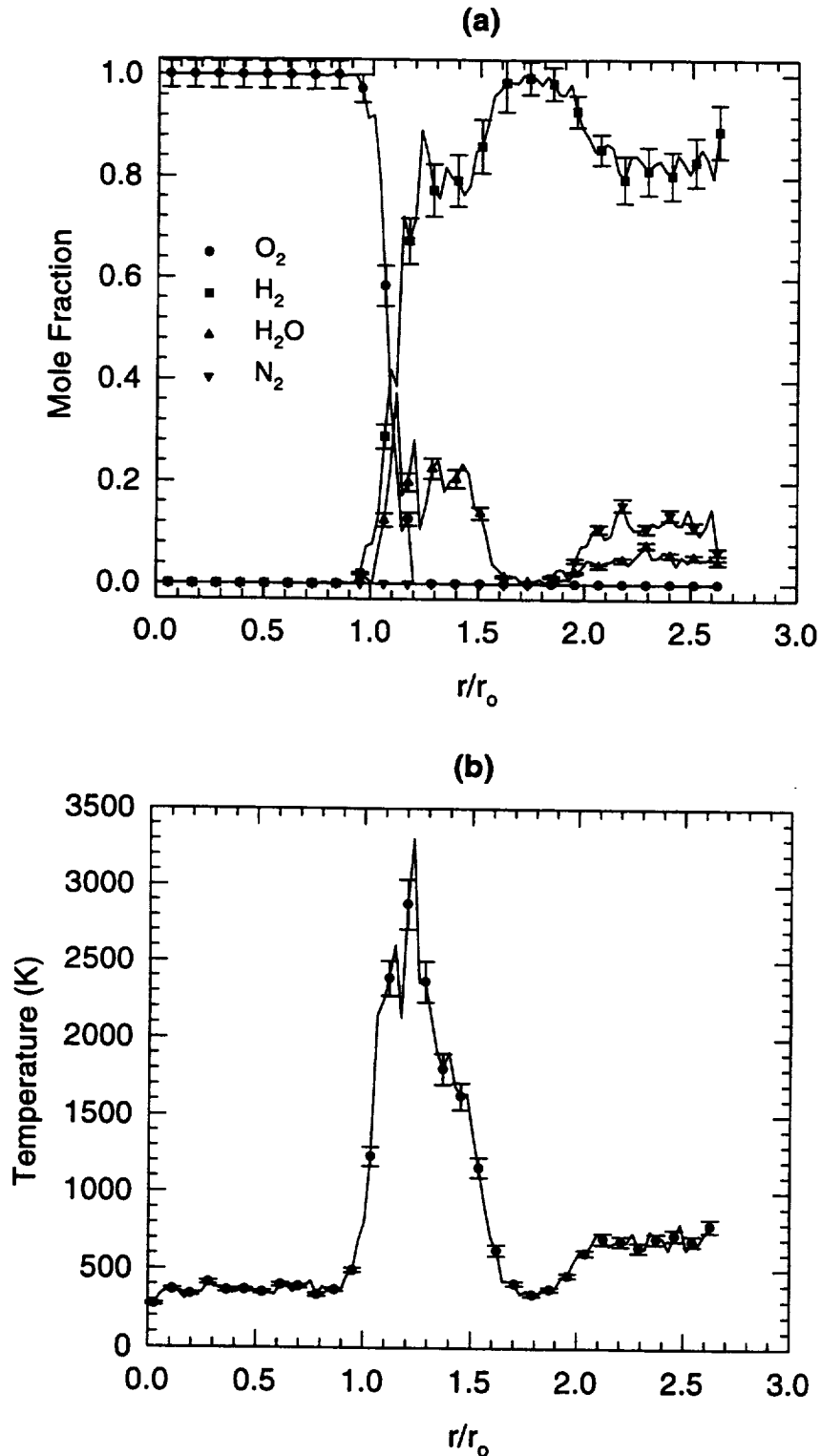
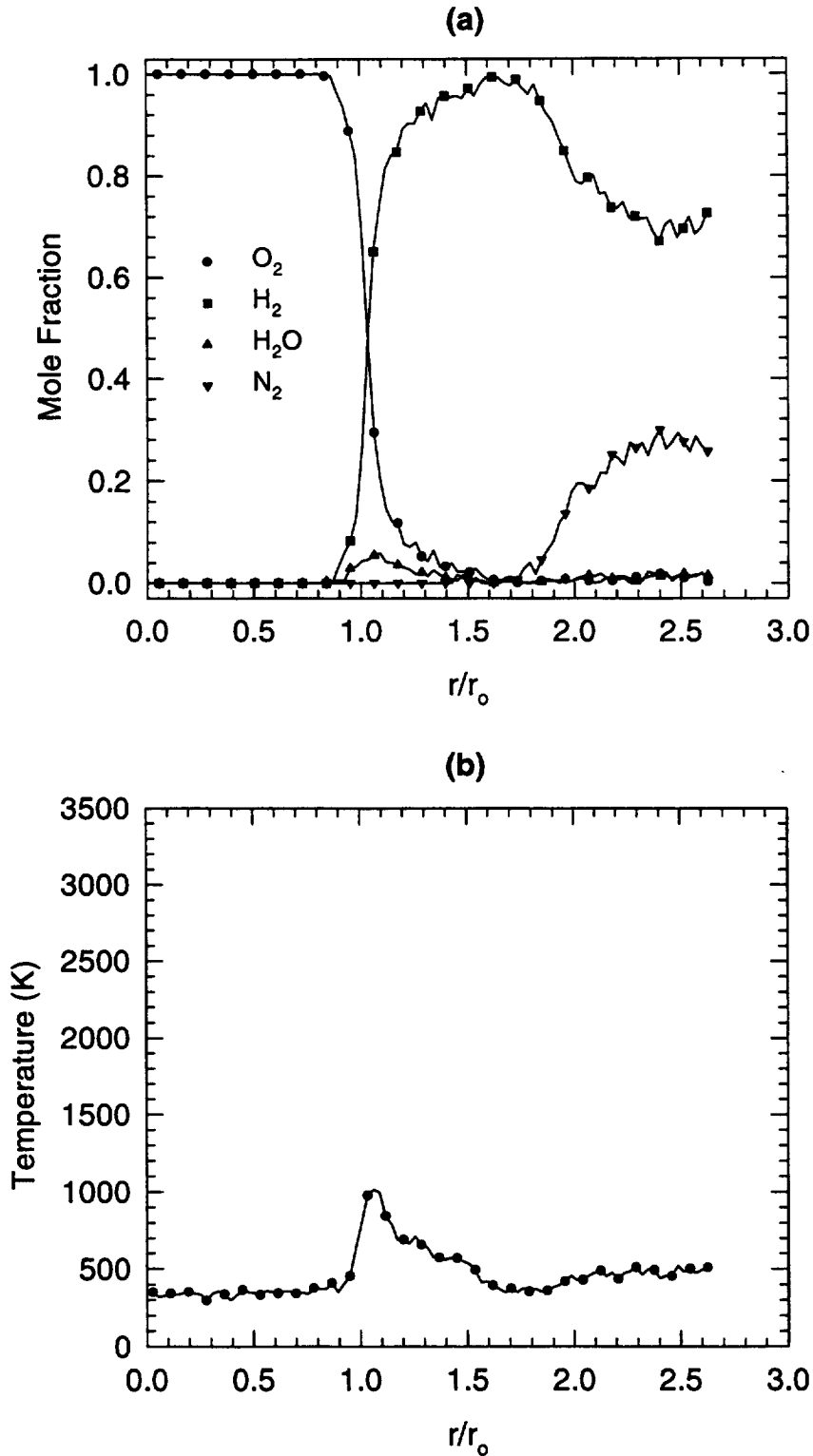
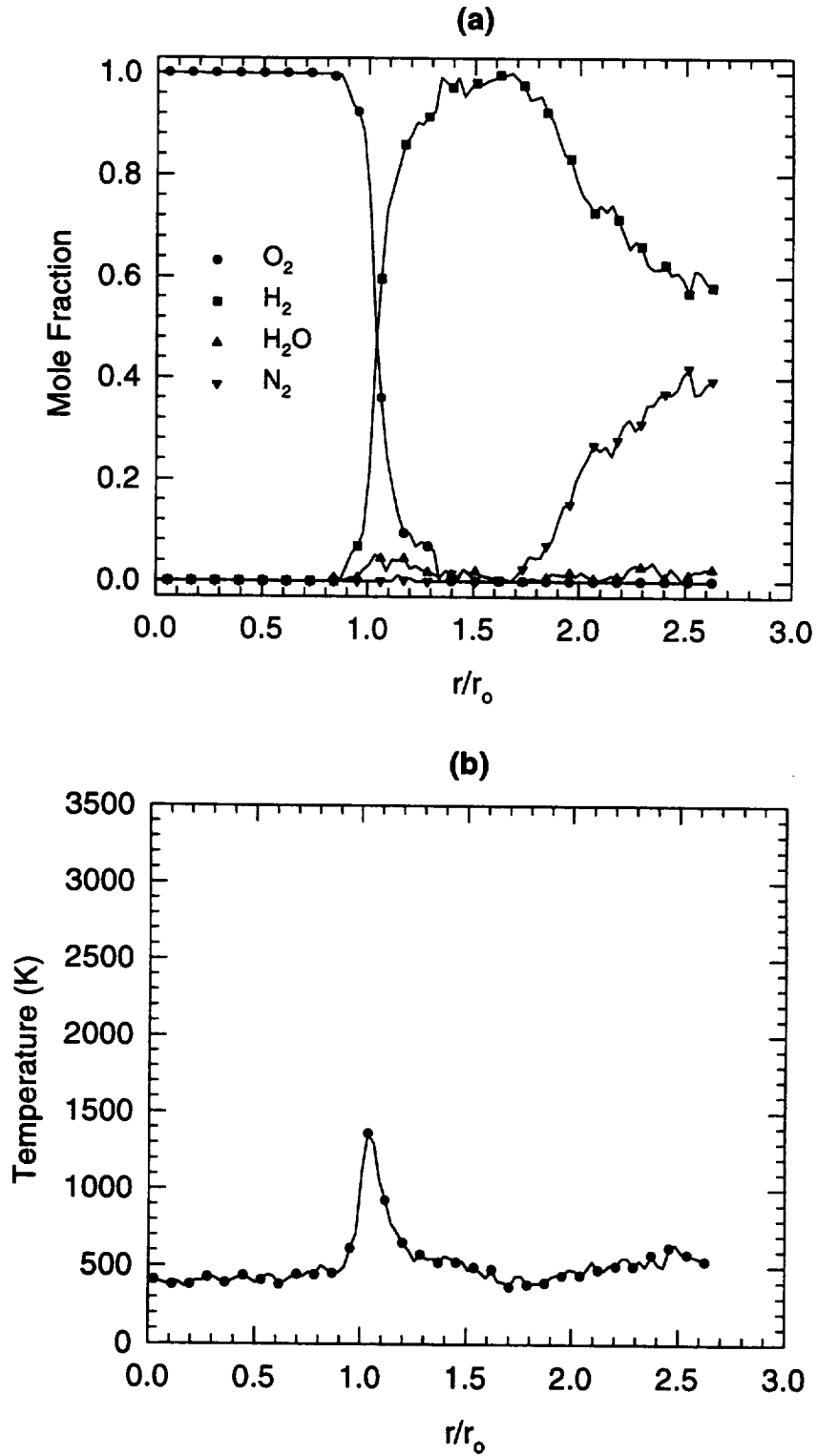


Fig. 4.15. Radial profiles of (a) species mole fraction and (b) temperature at an axial location of 0.5 mm downstream from the thick-walled shear coaxial injector tip.  $O/F = 4$ , momentum ratio = 0.746. The errors bars represent a  $\pm 1$  standard deviation precision uncertainty for the measurements.



**Fig. 4.16. Radial profiles of (a) species mole fraction and (b) temperature at an axial location of 0.5 mm downstream from the thick-walled shear coaxial injector tip. O/F = 14, momentum ratio = 0.061.**



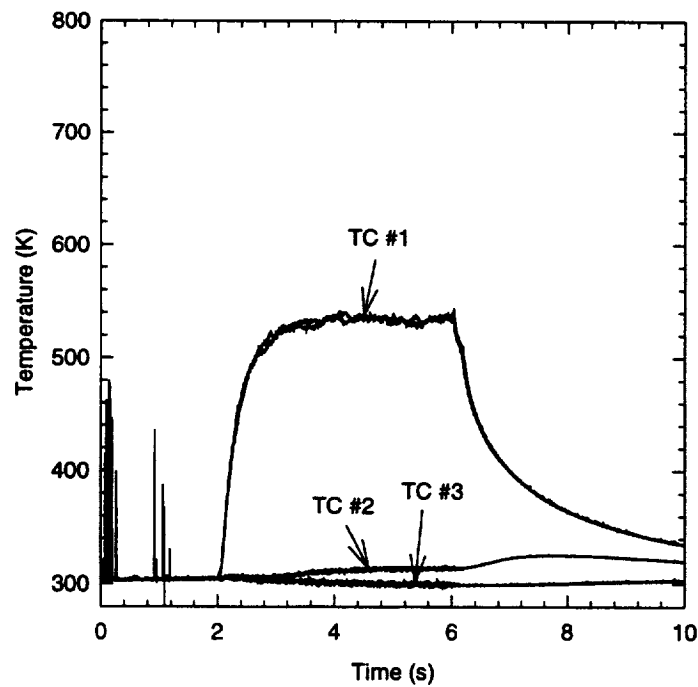
**Fig. 4.17. Radial profiles of (a) species mole fraction and (b) temperature at an axial location of 0.5 mm downstream from the thick-walled shear coaxial injector tip.  $O/F = 50$ , momentum ratio = 0.005.**

Fig. 4.15 for a 100% average mole fraction of  $\text{GO}_2$  was 2.7% at an average temperature of 300 K. The precision uncertainty in the extracted temperature measurement of 300 K was 2.9%. For an average temperature of 2871 K and an average  $\text{H}_2\text{O}$  mole fraction of 0.282, the uncertainty in the mole fraction and temperature measurement was 8.9% and 6.4%, respectively. The shot-noise limited uncertainty in a single-shot measurement for 100% mole fraction of  $\text{GO}_2$  at 1.4 MPa chamber pressure and 300 K temperature was 12.5%.

Comparison of the  $\text{GO}_2$  and  $\text{GH}_2$  species results displayed in Figs. 4.13-4.17 clearly shows that the flow pattern of the species in the injector base region depends on the relative momentums between the propellant flows. Since the results represent an average of an unsteady flame, the  $\text{GO}_2$  and  $\text{GH}_2$  profiles are shown to overlap. However, the trends in the resulting data show the dependence of the flame anchoring position on the momentum ratio. For the momentum ratio cases  $> 1$ , the  $\text{GO}_2$  profile drops to 0 near the  $\text{GH}_2$  side of the injector tip at  $r/r_0 \approx 1.6$ , where as, the  $\text{GH}_2$  profile decreases to 0 at  $r/r_0 \approx 1.3$ . These species profiles show that the  $\text{GO}_2$  flows into the injector base region and reacts with the  $\text{GH}_2$  flow near the injector tip corner adjacent to the higher momentum  $\text{GH}_2$  flow. The corresponding  $\text{H}_2\text{O}$  mole fraction and temperature peaks at  $r/r_0 \approx 1.3$ . As previously mentioned, the  $\text{H}_2\text{O}$  and temperature profiles are relatively broad, extending across the injector tip. For the momentum ratio cases  $< 1$ , the  $\text{GO}_2$  profile drops to 0 near the  $\text{GO}_2$  side of the injector tip at  $r/r_0 \approx 1.2$ , where as, the  $\text{GH}_2$  profile approaches 0 near the  $\text{GO}_2$  corner of the injector tip at  $r/r_0 = 1.0$ . The corresponding  $\text{H}_2\text{O}$  mole fraction and temperature profiles are shown to peak at  $r/r_0 \approx 1.1$ . As shown in Figs. 4.16 and 4.17 for the momentum ratio cases = 0.061 and 0.005, the  $\text{H}_2\text{O}$  mole fraction and temperature values are quite low which stems from averaging over a very thin fluctuating shear layer. Nevertheless, the overall results clearly indicate that the  $\text{GH}_2$  flows into the base region of the injector tip at momentum ratios  $< 1$  and reacts with the  $\text{GO}_2$  near the injector tip corner adjacent to the higher momentum  $\text{GO}_2$  flow. It should be noted that as the  $\text{GH}_2$  momentum decreases, the mole fraction of the  $\text{GN}_2$  purge in the outer flow region increases. In retrospect, these results show that the flame is stabilized on the injector tip corner adjacent to the higher momentum gas flow.

### 4.2.2 Injector Tip Temperature Measurements

Three different temperature measurements were obtained within the injector post wall during two rocket firings for each test case,  $O/F = 1, 2, 4, 14$  and  $50$ . The measurements as shown in Figs. 4.18-4.22 were taken with the thermocouples that were located at  $0$  (TC #1),  $6.35$  (TC #2) and  $12.7$  mm (TC #3) from the injector tip. The results from two rocket firings for each test case are superimposed to show the repeatability of the temperature measurements. The injector tip temperature measurements for the different  $O/F$  conditions reach steady-state conditions at different times during the  $4$  s test firing duration ( $2$  to  $6$  s time interval during  $10$  s long rocket firing sequence). However, all of the test cases show that steady-state was achieved within  $3.5$  s into the firing. The average and rms temperature values for each mixture ratio case are shown at steady state conditions in Table 4.2.



**Fig. 4.18.** Thermocouple temperature measurements within the  $GO_2$  post wall of the shear coaxial injector operating at an  $O/F = 1$ .

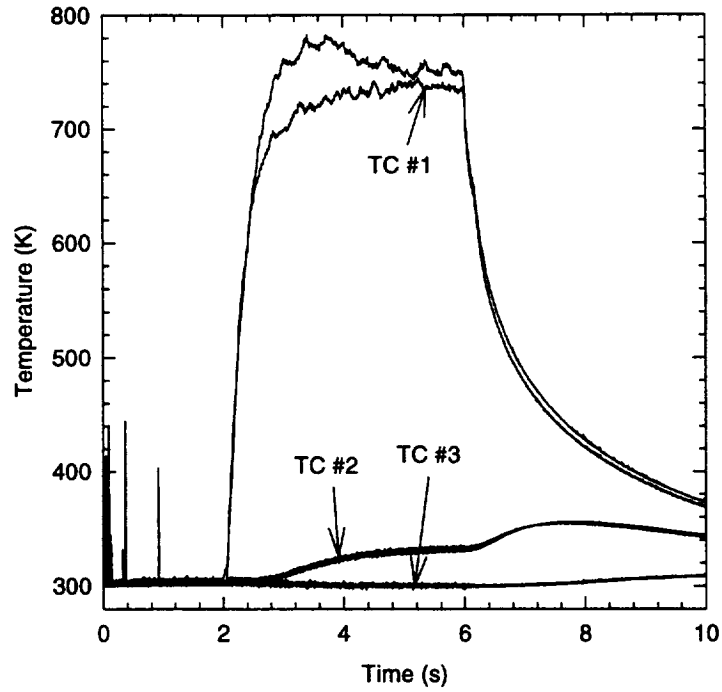


**Fig. 4.19. Thermocouple temperature measurements within the  $\text{GO}_2$  post wall of the shear coaxial injector operating at an  $O/F = 2$ .**

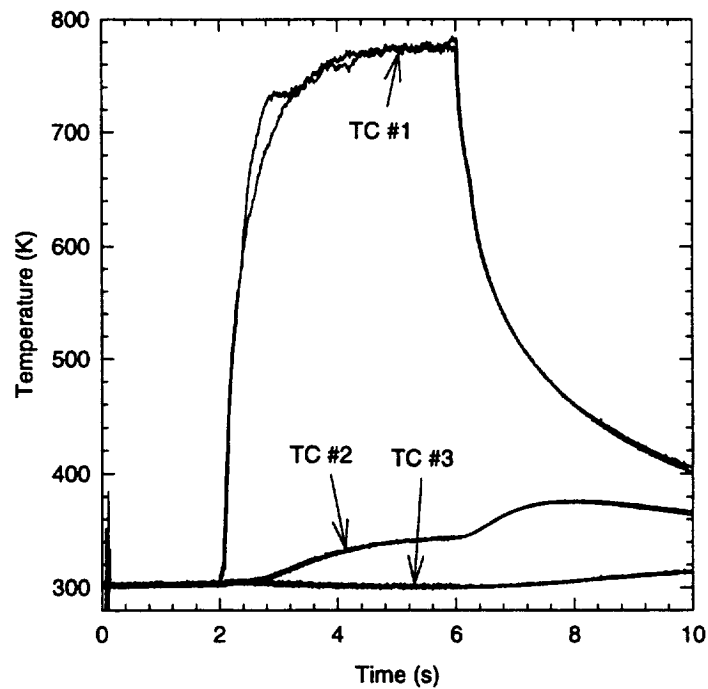


**Fig. 4.20. Thermocouple temperature measurements within the  $\text{GO}_2$  post wall of the shear coaxial injector operating at an  $O/F = 4$ .**

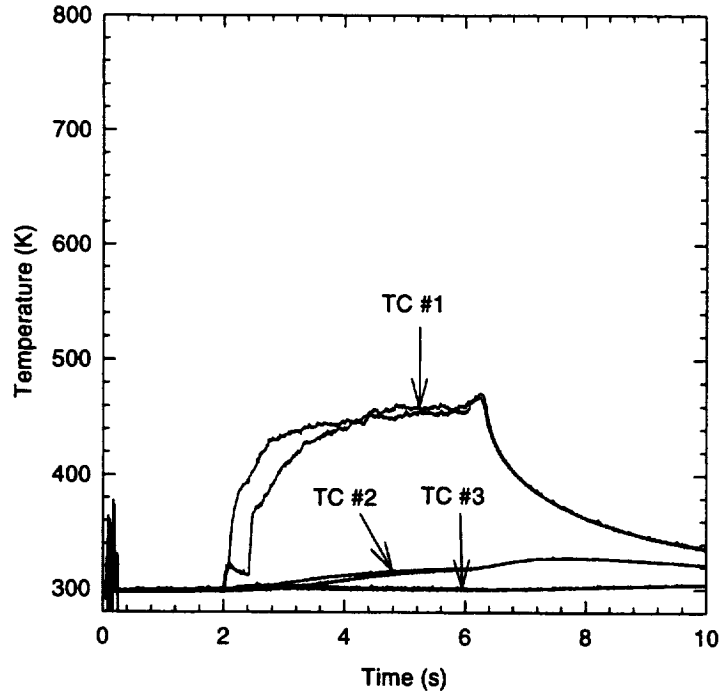


**Fig. 4.21. Thermocouple temperature measurements within the  $\text{GO}_2$  post wall of the shear coaxial injector operating at an  $\text{O/F} = 14$ .**

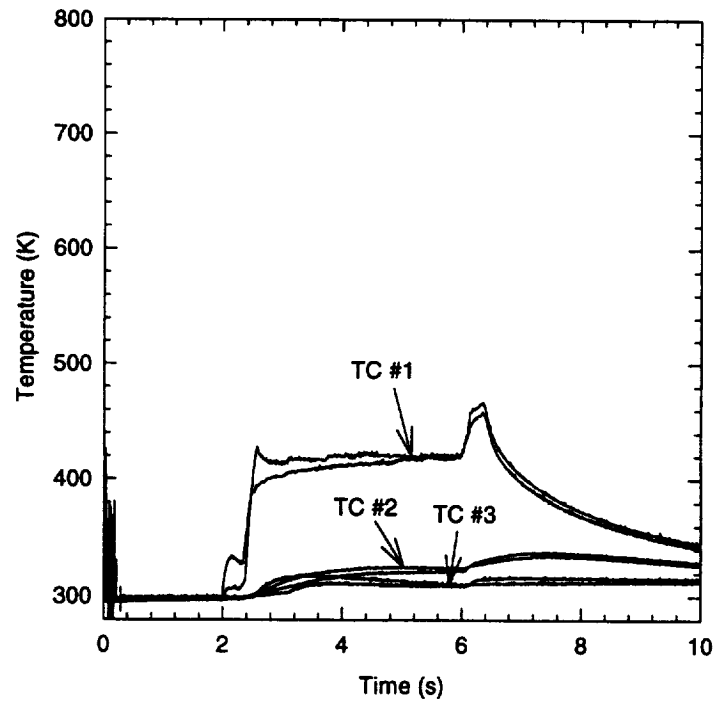


**Fig. 4.22. Thermocouple temperature measurements within the  $\text{GO}_2$  post wall of the shear coaxial injector operating at an  $\text{O/F} = 50$ .**

**Table 4.2. Steady-state temperature values of three different thermocouple measurements within injector post wall for O/F = 1, 2, 4, 14 and 50. Precision uncertainties in the measurements are indicated by  $\pm 1$  standard deviation values.**

O/F	TC #1 (°K)	TC #2 (°K)	TC #3 (°K)
1	535.5 $\pm$ 1.6	313.7 $\pm$ 0.9	300.1 $\pm$ 1.6
2	735.4 $\pm$ 1.8	333.3 $\pm$ 0.8	300.4 $\pm$ 0.9
4	778.0 $\pm$ 2.3	343.5 $\pm$ 0.8	300.3 $\pm$ 0.9
14	455.2 $\pm$ 1.2	317.4 $\pm$ 0.5	300.0 $\pm$ 0.6
50	420.7 $\pm$ 0.7	321.6 $\pm$ 0.4	309.4 $\pm$ 0.4

These results provide an appropriate data base from which to compare the predictions of injector face heat transfer. Combined with the flowfield and species concentration measurements, these results represent a major step forward in the development of a validation data set for a CFD-based rocket injector design methodology.

## **V INJECTOR FLOWFIELD CHARACTERIZATION FOR GAS/GAS INJECTOR TECHNOLOGY (GGIT) PROGRAM**

During the last two years of this project, the scope of the research work was redirected to experimentally evaluate the mixing and combustion characteristics of various injector concepts for gaseous propellants to support one of the engine concepts for the proposed Reusable Launch Vehicle (RLV) technology program. The full-flow engine concept includes full flow of both the fuel and the oxidizer through the preburners and consequently, gaseous propellant injection in the main chamber. At the time of the development sequence, the data base for gas-gas injectors was limited [18-23]. To fill this gap, NASA MSFC formed a Gas-Gas Injector Technology (GGIT) team which included NASA MSFC as the coordinating organization, Penn State University and NASA Lewis as the uni-element and multi-element testbeds, respectively, and Rocketdyne as the industrial partner. The scope of this program was changed to support GGIT team activities.

The plan of the GGIT team was to first identify a number of "team designed" gas/gas injector concepts. Penn State University and NASA Lewis would then conduct experiments to document the flowfield characteristics for both uni- and multi-element configurations. Based on the results of this first phase of experimentation, a second series of injector concepts would be investigated.

In the first phase of the program, the assembled team members selected and designed gas-gas injector concepts for uni-element and multi-element testing at Penn State and NASA Lewis. The team-selected injector configurations included the O-F-O triplet, F-O-F triplet and swirl coaxial elements. In addition, two Rocketdyne proprietary injector elements were also investigated.

Based on the results of this first phase of experimentation the team decided, for the second phase, to investigate the flowfield characteristics of various geometric variations of the shear coaxial injector. This second phase of experimentation also included geometric variations of one of the Rocketdyne proprietary injector elements.

In this section, the experiments are discussed in terms of chronological order, i.e., the first phase of experimentation is discussed first followed by the second phase. In the first phase, the injector design logic for the "team-selected" injector configurations is presented, followed by a discussion of the results. The discussion of the second phase of experimentation includes the

reasoning for picking the shear coaxial injector element for characterization, the design characteristics of the injector and the experimental results.

## 5.1 FIRST PHASE OF EXPERIMENTATION

The three injector concepts decided by the GGIT team were chosen based on performance, material compatibility (injector face heat transfer issues), stability, complexity, cost, durability, packaging and manifolding issues. In addition, as per Rocketdyne's suggestions, all three injector concepts were tied to Rocketdyne's specifications for the full scale rocket engine. The injector designs represented the "best" designs possible in terms of scaling issues and facility limitations.

Rocketdyne's specifications for the full scale rocket engine are summarized in Table 5.1. The propellant combination was oxygen/hydrogen for both the oxidizer and fuel preburners. The hot gaseous oxygen-rich and fuel-rich products from the preburners were to be introduced into the main chamber with the gas-gas injectors. The "optimum" geometries for the three chosen injector configurations were first designed for the full scale rocket conditions. This task carried out by NASA Marshall and Penn State personnel showed that the chosen injector configurations could be packaged and manifolded within Rocketdyne's specifications for the full scale engine conditions.

**Table 5.1. Rocketdyne's Specifications for Full Scale Rocket Engine**

Chamber pressure ( $P_C$ )	3000 psia
Nominal Mixture Ratio	6
OX Preburner Mixture Ratio	156.5
FUEL Preburner Mixture Ratio	0.52
OX-Rich Gas Injection Temperature	1110 R
FUEL-Rich Gas Injection Temperature	1100 R
OX Flow	260 lbm/s
FUEL Flow	43.33 lbm/s
Throat Diameter	$\approx 5.5$ in.
Contraction Ratio	2.5 to 4.5
Chamber Diameter	8.8 to 12 in.
FUEL $\Delta P/P_C$	10 to 15%
OX $\Delta P/P_C$	15 to 20%
Manifold/Dome Velocity Head	< 2% of Injector $\Delta P$

The chosen injector elements were then designed within the Penn State facility limitations. The Penn State and NASA Lewis experiments were conducted using room temperature  $\text{GO}_2$  and  $\text{GH}_2$  propellants at a chamber pressure of 1000 psia, and hence there were basic differences in fluid and flow properties between the experiments and full scale rocket conditions. The design logic for the three gas-gas injector configurations examined at Penn State in the uni-element rocket chamber are presented next. This description is followed by a summary of the experimental techniques employed for characterizing the combusting  $\text{GO}_2/\text{GH}_2$  flowfields.

### 5.1.1 Experimental Setup

The three “team” injector elements were designed for implementation in the optically-accessible rocket chamber described in Chapter 2. (see Fig. 2.1 for details).

#### 5.1.1.1 Flow Conditions

The following three injector geometries were designed for gaseous oxygen/gaseous hydrogen flow at a mixture ratio of six. The target chamber pressure was 1000 psia for oxygen and hydrogen flowrates of 0.25 lbm/s and 0.042 lbm/s, respectively.

#### 5.1.1.2 O-F-O Triplet Element

The basic schematic of the O-F-O triplet is shown in Fig. 5.1. The design of the injector considers the following geometric terms, diameter of OX orifice,  $d_o$ , diameter of FUEL orifice,  $d_f$ , impingement half-angle,  $\theta$ , and orifice spacing,  $s$ . In addition, the length to diameter ratio of the orifices is important in terms of flow development and packaging issues. These geometric parameters directly affect performance, face heat transfer issues and stability. Since the performance of the injector is related to gaseous propellant mixing, the matching of the propellant stream momentum is important. Previous work by Aerojet on gas-gas injectors [18] suggested that optimum mixing efficiency occurred when:

$$(2.3\dot{m}_F V_F) / (\dot{m}_O V_O \sin \theta) = 2 \quad \text{Equation (5.1)}$$

where  $\dot{m}$  and  $V$  are mass flowrate and velocity, and the subscripts O and F refer to oxidizer and fuel, respectively. Therefore, in terms of performance, the above equation was first used as a guideline for designing the individual O-F-O injector and full injector assembly layout for the full scale rocket specifications as suggested by Rocketdyne. This task was performed by personnel from NASA Marshall, Penn State and Rocketdyne. As a baseline for the O-F-O triplet, a  $\theta$  of  $30^\circ$

was chosen. Since the number of elements, element design, injector face packaging and flow manifolding are inherently interrelated, an iterative procedure was used to formulate the injector design for the full scale rocket specifications. At each step of the iterative procedure, the elements for the full scale conditions were designed such that the LHS of equation 5.1 was as close to the RHS within the flow (flowrate, injector pressure drop, etc.) specifications. The results of this endeavor showed that nominally 244 O-F-O triplet elements (optimized based on

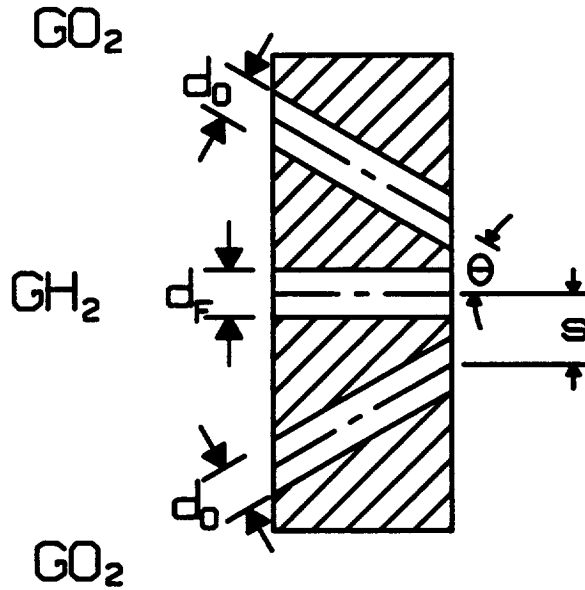


**Fig. 5.1. Schematic of O-F-O Triplet Injector for  $GO_2/GH_2$  Propellants.**

equation 5.1) could be packaged on a faceplate in either a "linear" or "ring" type arrangement within the proposed injector faceplate size and injector manifold pressure drop criteria. This design then represents the full scale design to which both the experimental results from the Penn State and NASA Lewis should be scaled.

The next step involved optimizing the single O-F-O injector design for the Penn State experimental conditions for  $GO_2/GH_2$  propellants. The Penn State design was for the same propellant O/F ratio of six at a  $GO_2$  mass flowrate of 0.25 lbm/s and 1000 psia chamber pressure. The injector designs for the PSU test conditions and full scale engine conditions are compared in Table 5.2. Although exact similitude between all the Penn State and full scale rocket conditions could not be realized because of different flowrate, chamber pressure and propellant properties, both injectors were optimized based on the Aerojet correlation (i.e. momentum ratio),[18] and hence the experimental results obtained should be scalable to full scale conditions. Note also that the chamber pressure and mass flowrate per element ratios between the two injector designs essentially cancel to yield injectors that are geometrically within 50% of each other.

The assembly drawing for the O-F-O triplet injector is shown in Fig. 5.2. The injector assembly consists of a  $GO_2$  manifold body, a  $GH_2$  post that feeds through the  $GO_2$  manifold body and screws to the injector faceplate. The  $GO_2$  manifold body is an existing piece of hardware (see Fig. 2.1) that is used for the O-F-O triplet.

**Table 5.2. O-F-O Triplet Design Considerations**

(#) Parameter	PSU Conditions	Rocketdyne Rocket Specifications	RATIO (Rocket/PSU)	Comments PSU/Rocket
(1) Chamber Pressure ( $P_C$ )	1000 psia	3000 psia	3.0	facility maximum/specified
(2) O/F	6	6	1.0	specified/specified
(3) Number of Elements	1	244	244	uni-element/244 elem. from packaging
(4) $\dot{m}_{OX}$ Total	0.25 lb/s	260 lb/s	1040.0	facility maximum/specified
(5) $\dot{m}_{OX}$ Per Element	0.25 lb/s	1.0656 lb/s	4.26	specified/from packaging
(6) OX Mol. Weight	32.0	30.65	0.96	specified/specified
(7) OX Gamma	1.4	1.31	0.93	specified/specified
(8) OX Temperature	540 R	1110 R	2.06	specified/specified
(9) OX Density	5.53 lb/ft <sup>3</sup>	7.73 lb/ft <sup>3</sup>	1.40	specified/specified
(10) OX Sound Speed	1084 ft/s	1533 ft/s	1.41	specified/specified
(11) $\dot{m}_{FUEL}$ Total	0.042 lb/s	43.33 lb/s	1040.0	specified/specified
(12) $\dot{m}_{FUEL}$ Per Element	0.042 lb/s	0.18 lb/s	4.26	specified/from packaging
(13) FUEL Mol. Weight	2.02	3.06	1.52	specified/specified
(14) FUEL Gamma	1.4	1.38	0.98	specified/specified
(15) FUEL Temperature	540 R	1100 R	2.04	specified/specified
(16) FUEL Density	0.35 lb/ft <sup>3</sup>	0.78 lb/ft <sup>3</sup>	2.23	specified/specified
(17) FUEL Sound Speed	4314 ft/s	4959 ft/s	1.15	specified/specified
(18) Impingement Half-Angle	30°	30°	1.0	design point/design point
(19) $d_{OX}$	0.0999 in.	0.1443 in.	1.44	rocket geometry ~ 50% bigger
(20) $d_{FUEL}$	0.1269 in.	0.1628 in.	1.28	rocket geometry ~ 50% bigger
(21) Impingement Distance from Faceplate ( $d_{imp}$ )	0.50 in.	0.72 in.	1.44	$5d_{OX}/5d_{OX}$
(22) Faceplate Thickness (l)	0.31 in.	0.4 in.	1.29	$l/d_{FUEL}$ same as for rocket/nominal
(23) OX $C_D$	0.85	0.85	1.0	assumed/assumed
(24) FUEL $C_D$	0.85	0.85	1.0	assumed/assumed
(25) OX Velocity	489 ft/s	715 ft/s	1.46	inj. velocities are within 50%
(26) FUEL Velocity	1603 ft/s	1857 ft/s	1.16	inj. velocities are within 50%
(27) FUEL/OX Vel. Ratio	3.28	2.60	0.79	velocity ratios are within 20%
(28) OX Mach #	0.45	0.47	1.04	Mach numbers are identical
(29) FUEL Mach #	0.37	0.37	1.0	Mach numbers are identical
(30) $\Delta P_{OX}/P_C$	0.15	0.15	1.0	injector pressure drops are identical
(31) $\Delta P_{FUEL}/P_C$	0.10	0.10	1.0	injector pressure drops are identical
(32) Momentum Ratio ( $m_F V_F / (m_O V_O \sin \theta)$ )	1.10	0.87	0.79	momentum ratios are nearly identical
(33) RHS of Aerojet Corr.	2.52	1.99	0.79	<b>BOTH INJECTORS ARE CLOSE TO AEROJET DESIGN CONDITIONS</b>

**5.1.1.3 F-O-F Triplet Element**

The basic schematic of the F-O-F triplet is shown in Fig. 5.3. The design of the injector considers the following geometric terms, diameter of OX orifice,  $d_o$ , diameter of FUEL orifice,  $d_f$ , impingement half-angle,  $\theta$ , and orifice spacing,  $s$ . In addition, the length to diameter ratio of the orifices is important in terms of flow development and packaging issues. These geometric parameters directly affect performance, face heat transfer issues and stability. Since the performance of the injector is related to gaseous propellant mixing, the matching of the

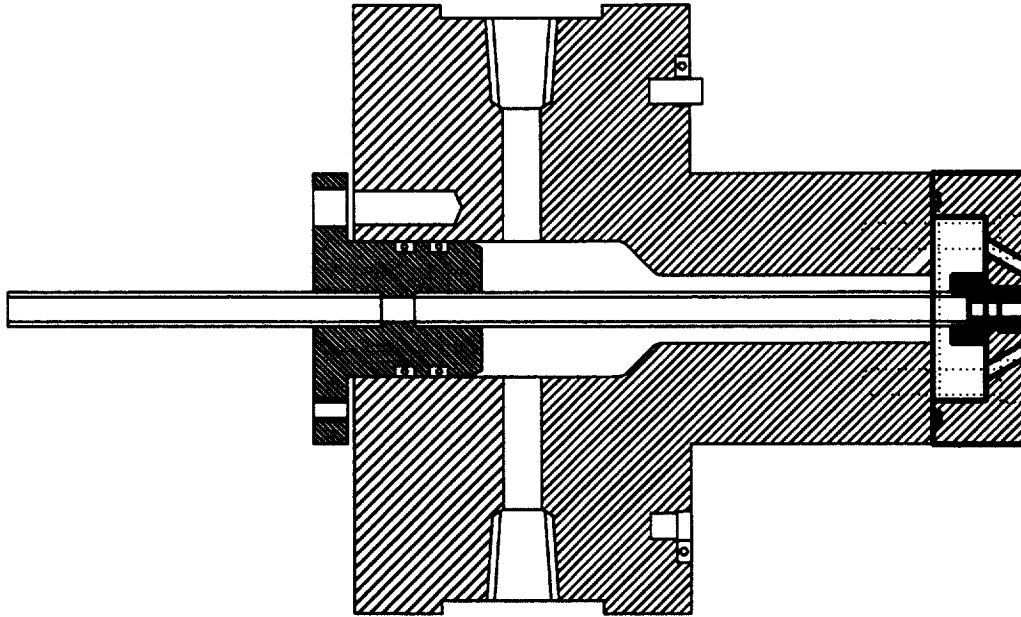


**Fig. 5.2. Assembly drawing for the O-F-O triplet injector. The injector assembly consists of a  $\text{GO}_2$  manifold body, a  $\text{GH}_2$  post that feeds through the  $\text{GO}_2$  manifold body and screws to the injector faceplate.**

propellant stream momentum is important. Previous work by Aerojet [18] on gas-gas injectors suggested that optimum mixing efficiency occurred when:

$$(2.3\dot{m}_o V_o) / (\dot{m}_f V_f \sin \theta) = 2 \quad \text{Equation (5.2)}$$

where  $\dot{m}$  and  $V$  are mass flowrate and velocity, and the subscripts O and F refer to oxidizer and fuel, respectively. Therefore, in terms of performance, the above equation was first used as a guideline for designing the individual F-O-F injector and full injector assembly layout for the full scale rocket specifications as suggested by Rocketdyne. This task was performed by NASA Marshall, Penn State and Rocketdyne personnel. As a baseline for the F-O-F triplet, a  $\theta$  of  $30^\circ$  was chosen. Since the number of elements, element design, injector face packaging and

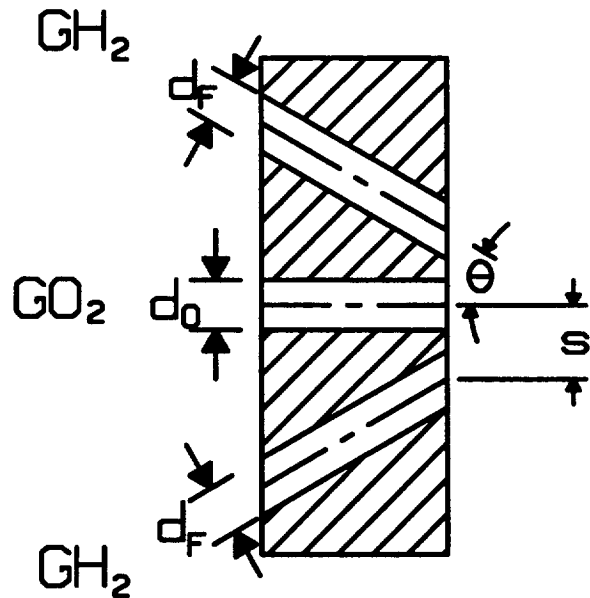


**Fig. 5.3 Schematic of F-O-F Triplet Injector for  $\text{GO}_2/\text{GH}_2$  Propellants.**

flow manifolding are inherently interrelated, an iterative procedure was used to formulate the injector design for the full scale rocket specifications. At each step of the iterative procedure, the elements for the full scale conditions were designed such that the LHS of equation 5.2 was as close to the RHS within the flow (flowrate, injector pressure drop, etc.) specifications. Unlike, the O-F-O triplet design, the F-O-F triplet could not be designed within the injector pressure drop criteria such that the LHS of equation 5.2 was about two (the best possible is about seven). The results of this endeavor showed that nominally 244 F-O-F triplet elements could be packaged on a faceplate in either a "linear" or "ring" type arrangement within the proposed injector faceplate size and injector manifold pressure drop criteria. This design then represents the full scale design to which both the experimental results from the Penn State and NASA Lewis should be scaled.

The next step involved optimizing the single F-O-F injector design for the Penn State experimental conditions for  $\text{GO}_2/\text{GH}_2$  propellants. The Penn State design was for the same propellant O/F ratio of six at a  $\text{GO}_2$  mass flowrate of 0.25 lbm/s and 1000 psia chamber pressure. The injector designs for the PSU test conditions and full scale engine conditions are compared in Table 5.3. Although exact similitude between all the Penn State and full scale rocket conditions could not be realized because of different flowrate, chamber pressure and propellant properties, both injectors were optimized based on the Aerojet correlation (i.e. momentum ratio) [18] and hence the experimental results obtained should be scalable to full scale conditions. Note also that the chamber pressure and mass flowrate per element ratios between the two injector designs essentially cancel to yield injectors that are geometrically within 50% of each other.

The assembly drawing for the F-O-F triplet injector is exactly the same as that for the O-F-O triplet arrangement shown in Fig. 5.2, except that the propellant flows are reversed.

#### 5.1.1.4 Swirl Coaxial Element

The basic schematic of the swirl coaxial injector is shown in Fig. 5.4. The design of the injector considers the following geometric terms, OX post diameter,  $d_o$ , FUEL annulus inner diameter,  $d_{Fi}$ , and FUEL annulus outer diameter,  $d_{Fo}$ . Based on Aerojet's gas-gas injector research[18], propellant mixing increases with increasing swirl angle. The inner flow can be swirled either with tangential vanes or with a swirl nut with tangential slots. However, the physical dimensions of the injector increases for greater swirl angles for both methods. For the present design, the inner propellant flow was swirled with the aid of a swirl nut with tangential

**Table 5.3. F-O-F Triplet Design Considerations**

(#) Parameter	PSU Conditions	Rocketdyne Rocket Specifications	RATIO (Rocket/PSU)	Comments PSU/Rocket
(1) Chamber Pressure ( $P_C$ )	1000 psia	3000 psia	3.0	facility maximum/specified
(2) O/F	6	6	1.0	specified/specified
(3) Number of Elements	1	244	244	uni-element/244 elem. from packaging
(4) $\dot{m}_{OX}$ Total	0.25 lb/s	260 lb/s	1040.0	facility maximum/specified
(5) $\dot{m}_{OX}$ Per Element	0.25 lb/s	1.0656 lb/s	4.26	specified/from packaging
(6) OX Mol. Weight	32.0	30.65	0.96	specified/specified
(7) OX Gamma	1.4	1.31	0.93	specified/specified
(8) OX Temperature	540 R	1110 R	2.06	specified/specified
(9) OX Density	5.53 lb/ft <sup>3</sup>	7.73 lb/ft <sup>3</sup>	1.40	specified/specified
(10) OX Sound Speed	1084 ft/s	1533 ft/s	1.41	specified/specified
(11) $\dot{m}_{FUEL}$ Total	0.042 lb/s	43.33 lb/s	1040.0	specified/specified
(12) $\dot{m}_{FUEL}$ Per Element	0.042 lb/s	0.18 lb/s	4.26	specified/from packaging
(13) FUEL Mol. Weight	2.02	3.06	1.52	specified/specified
(14) FUEL Gamma	1.4	1.38	0.98	specified/specified
(15) FUEL Temperature	540 R	1100 R	2.04	specified/specified
(16) FUEL Density	0.35 lb/ft <sup>3</sup>	0.78 lb/ft <sup>3</sup>	2.23	specified/specified
(17) FUEL Sound Speed	4314 ft/s	4959 ft/s	1.15	specified/specified
(18) Impingement Half-Angle	30°	30°	1.0	design point/design point
(19) $d_{OX}$	0.1413 in.	0.2040 in.	1.44	rocket geometry $\approx$ 50% bigger
(20) $d_{FUEL}$	0.076 in.	0.0976 in.	1.28	rocket geometry $\approx$ 50% bigger
(21) Impingement Distance from Faceplate ( $d_{imp}$ )	0.54 in.	0.75 in.	1.39	$5d_{OX}/5d_{OX}$
(22) Faceplate Thickness (l)	0.28 in.	0.4 in.	1.43	$l/d_{FUEL}$ same as for rocket/nominal
(23) OX $C_D$	0.85	0.85	1.0	assumed/assumed
(24) FUEL $C_D$	0.85	0.85	1.0	assumed/assumed
(25) OX Velocity	489 ft/s	715 ft/s	1.46	inj. velocities are within 50%
(26) FUEL Velocity	2230 ft/s	2583 ft/s	1.16	inj. velocities are within 50%
(27) FUEL/OX Vel. Ratio	4.56	3.61	0.79	velocity ratios are within 20%
(28) OX Mach #	0.45	0.47	1.04	Mach numbers are identical
(29) FUEL Mach #	0.52	0.52	1.0	Mach numbers are identical
(30) $\Delta P_{OX}/P_C$	0.15	0.15	1.0	injector pressure drops are identical
(31) $\Delta P_{FUEL}/P_C$	0.20	0.20	1.0	injector pressure drops are identical
(32) Momentum Ratio ( $m_O V_O$ ) / ( $m_F V_F \sin \theta$ )	2.63	3.32	1.26	momentum ratios are nearly identical
(33) RHS of Aerojet Corr.	6.05	7.64	1.26	BOTH INJECTORS ARE NOT CLOSE TO AEROJET DESIGN CONDITIONS

slots. Also, the mixing characteristics of the swirl coaxial injector is worst when the velocity ratio between fuel-to-oxidizer flow is  $\approx 11$  [18]. For velocity ratios greater of smaller than about 11, the mixing efficiency is reported to increase [18]. In terms of utilizing the swirl component of the inner flow (oxidizer) to promote mixing and propellant spreading, momentum considerations indicate that the swirl coaxial injector be operated at lower fuel-to-oxidizer velocity ratios.

The aforementioned guidelines were used to design the individual swirl coaxial injector and full injector assembly layout for the full scale rocket specifications with the same iterative

procedure used for designing the O-F-O and F-O-F triplet elements. The design methodology for swirl coaxial injectors described in Reference [18] was utilized for designing the injector. The results of this endeavor showed that nominally 270 swirl coaxial elements with a swirl angle of 75 degrees could be packaged on a faceplate in the "ring" type arrangement within the proposed injector faceplate size and injector manifold pressure drop criteria. This design then represents the full scale design to which both the experimental results from the Penn State and NASA Lewis should be scaled.

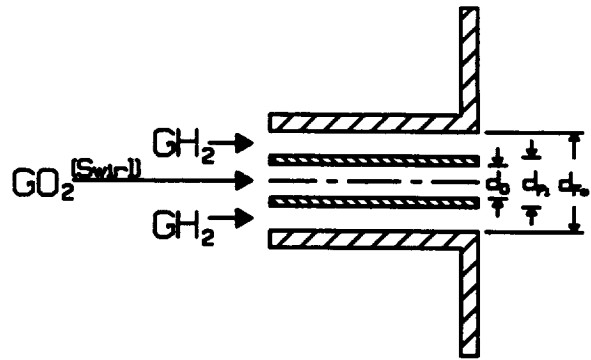


**Fig. 5.4. Schematic of Swirl Coaxial Injector for  $GO_2/GH_2$  Propellants.**

The next step involved optimizing the single swirl coaxial injector design for the Penn State experimental conditions for  $GO_2/GH_2$  propellants. The Penn State design was for the same propellant O/F ratio of six at a  $GO_2$  mass flowrate of 0.25 lbm/s and 1000 psia chamber pressure. The injector designs for the PSU test conditions and full scale engine conditions are compared in Table 5.4. Note that the chamber pressure and mass flowrate per element ratios between the two injector designs essentially cancel to yield injectors that are geometrically within 50% of each other. In addition to the 75 degree swirl angle geometry, the effect of swirl angle on combustion was assessed by experimenting at other swirl angles, viz. 60 and 90 degrees.

The design of the  $GO_2$  post for the swirl coaxial injector is shown in Fig. 5.5. The  $GO_2$

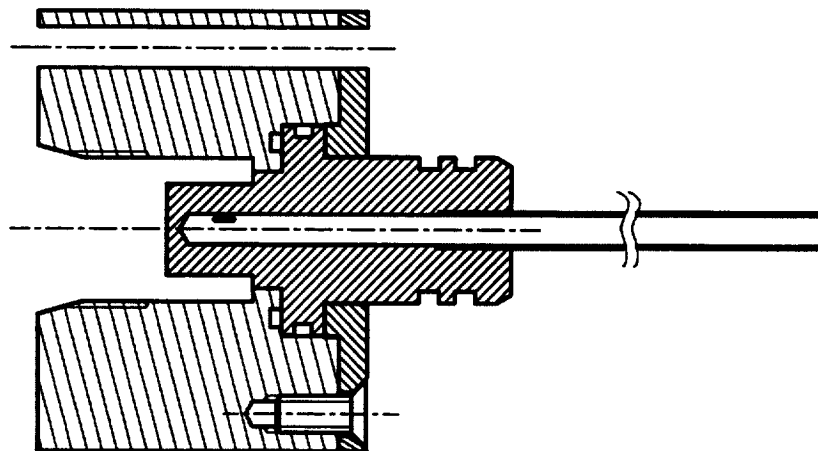


**Fig. 5.5.  $GO_2$  post design for swirl coaxial injector.  $GO_2$  post was designed to screw onto injector assembly shown in Fig. 2.1.**

**Table 5.4. Swirl Coaxial Injector Design Considerations**

(#) Parameter	PSU Conditions	Rocketdyne Rocket Specifications	RATIO (Rocket/PSU)	Comments PSU/Rocket
(1) Chamber Pressure ( $P_C$ )	1000 psia	3000 psia	3.0	facility maximum/specified
(2) O/F	6	6	1.0	specified/specified
(3) Number of Elements	1	270	270	uni-element/270 elem. from packaging
(4) $\dot{O}_X$ Total	0.25 lb/s	260 lb/s	1040.0	facility maximum/specified
(5) $\dot{O}_X$ Per Element	0.25 lb/s	0.963 lb/s	3.85	specified/from packaging
(6) OX Mol. Weight	32.0	30.65	0.96	specified/specified
(7) OX Gamma	1.4	1.31	0.93	specified/specified
(8) OX Temperature	540 R	1110 R	2.06	specified/specified
(9) OX Density	5.53 lb/ft <sup>3</sup>	7.73 lb/ft <sup>3</sup>	1.40	specified/specified
(10) OX Sound Speed	1084 ft/s	1533 ft/s	1.41	specified/specified
(11) $\dot{FUEL}$ Total	0.042 lb/s	43.33 lb/s	1040.0	specified/specified
(12) $\dot{FUEL}$ Per Element	0.042 lb/s	0.16 lb/s	3.85	specified/from packaging
(13) FUEL Mol. Weight	2.02	3.06	1.52	specified/specified
(14) FUEL Gamma	1.4	1.38	0.98	specified/specified
(15) FUEL Temperature	540 R	1100 R	2.04	specified/specified
(16) FUEL Density	0.35 lb/ft <sup>3</sup>	0.78 lb/ft <sup>3</sup>	2.23	specified/specified
(17) FUEL Sound Speed	4314 ft/s	4959 ft/s	1.15	specified/specified
(18) Full Swirl Cone Angle	75°	75°	1.0	design point/design point
(19) $d_{OX}$	0.2802 in.	0.3843 in.	1.37	rocket geometry = 40% bigger
(20) $d_{Fi}$	0.3302 in.	0.4343 in.	1.32	rocket geometry = 40% bigger
(21) $d_{Fo}$	0.3702 in.	0.4743 in.	1.28	rocket geometry = 40% bigger
(22) OX Post Wall Thickness	0.025 in.	0.025 in.	1.0	same OX post wall thickness fabrication limitation
(23) FUEL Annulus Gap Width	0.020 in.	0.020 in.	1.0	same FUEL annulus gap fabrication limitation
(24) OX $C_D$	0.1825	0.1825	1.0	calculated/calculated
(25) FUEL $C_D$	1.0	1.0	1.0	assumed/assumed
(26) OX Velocity	342 ft/s	501 ft/s	1.46	inj. velocities are within 50%
(27) FUEL Velocity	782 ft/s	1040 ft/s	1.33	inj. velocities are within 50%
(28) FUEL/OX Vel. Ratio	2.29	2.08	0.91	velocity ratios are within 10%
(29) Momentum Ratio ( $m_F V_F$ ) / ( $m_O V_O$ )	0.38	0.35	0.92	momentum ratios are nearly identical
(30) OX Mach #	0.32	0.33	1.03	Mach numbers are within 20%
(31) FUEL Mach #	0.18	0.21	1.17	Mach numbers are within 20%
(32) $\Delta P_{OX}/P_C$	0.20	0.20	1.0	injector pressure drops are identical
(33) $\Delta P_{FUEL}/P_C$	0.023	0.030	1.3	FUEL pressure drop may need to be increased with upstream orifice

post is designed to screw onto the injector assembly of the rocket chamber depicted in Fig. 2.1. The post design includes a swirl nut that feeds the oxidizer tangentially into the central tube from a swirl chamber. The screw-on face plate shown in the rocket assembly (see Fig. 2.1) defines the outer diameter of the  $GH_2$  fuel annulus, whereas the inner diameter of the  $GH_2$  fuel annulus is defined by the outer diameter of the  $GO_2$  post. The swirl injector was designed in this modular fashion such that swirl nut/ $GO_2$  tube assemblies for different swirl angles could be easily interchanged. A photograph of the three swirl injector elements is shown in Fig. 5.6. The design specifics of the three swirl coaxial injector elements are tabulated in Table 5.5.

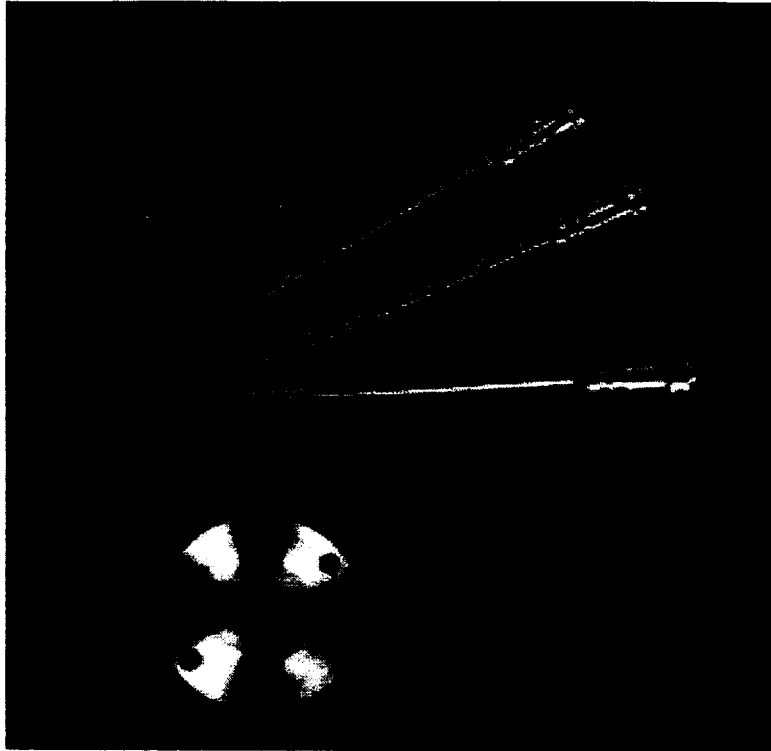


**Fig. 5.6. Photograph of the swirl coaxial injector. The three posts shown are for swirl angles of 60, 75 and 90 degrees. The photograph also shows the faceplate and two “nuts” that are used for varying the GH<sub>2</sub> annulus.**

### 5.1.2 Experimental Diagnostics

Raman spectroscopy was employed as the major diagnostic technique for characterizing the mixing and combustion characteristics of the flowfield. In addition the injector face was instrumented with a thermocouple for injector face temperature measurements during the rocket firings. The implementation of these two techniques are discussed next.

#### 5.1.2.1 Raman Spectrometry (Line)

The Raman spectroscopy technique was developed and applied for making line images of

**Table 5.5. Swirl Coaxial Injector Dimensions.**

	GO <sub>2</sub> post diameter (d <sub>O</sub> )	GH <sub>2</sub> annulus inner diameter (d <sub>F<sub>I</sub></sub> )	GH <sub>2</sub> annulus outer diameter (d <sub>F<sub>O</sub></sub> )
60° Swirl	0.210 in. (5.33 mm)	0.250 in. (6.35 mm)	0.290 in. (7.37 mm)
75° Swirl	0.277 in. (7.04 mm)	0.317 in. (8.05 mm)	0.357 in. (9.07 mm)
90° Swirl	0.370 in. (9.40 mm)	0.410 in. (10.4 mm)	0.450 in. (11.4 mm)

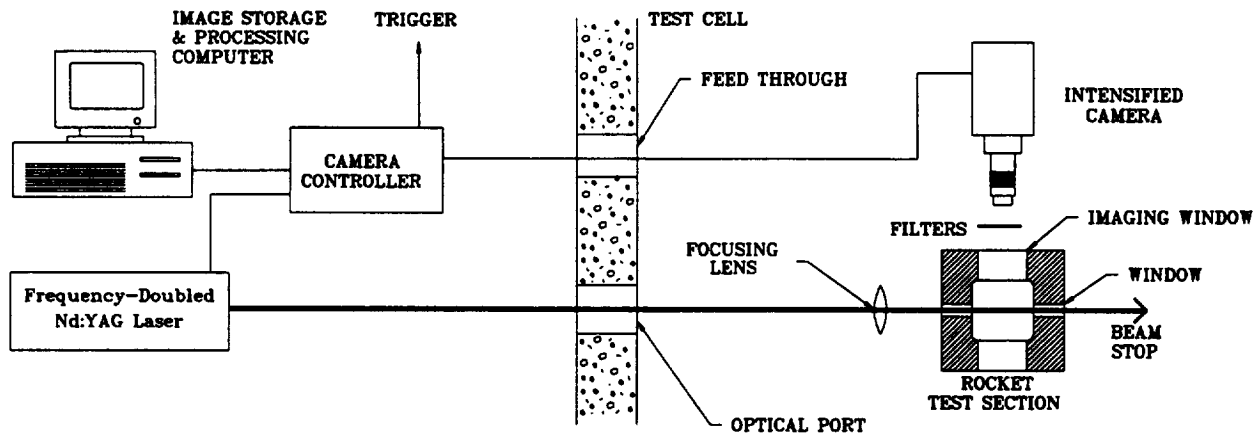


**Fig. 5.7. Experimental setup for Raman spectroscopy measurements.**

the species field in the combustion chamber. Various optical configurations can be used for applying the Raman spectroscopy technique [3,4]. Here an optical arrangement that stresses maximum collection of the weak Raman signal for making line images of the species field was developed. The experimental setup shown in Fig. 5.7 includes a frequency doubled Nd:YAG laser for Raman excitation and an intensified Charged Coulomb Device (CCD) camera for Raman signal detection. The frequency-doubled Nd:YAG laser delivers a pulse energy of 1 J at a wavelength of 532 nm. For the experiments reported here, the laser was operated to deliver 130 mJ per pulse (duration of 7 ns). The 10 mm diameter laser beam was focused using a 1500 mm lens to a waist of 0.3 mm downstream of the exit window. Inside the 25.4 mm (2 in.) cross section of the rocket chamber, the converging beam was nominally 1.3 mm in diameter. This optical arrangement prevented the quartz windows from being damaged by the high power laser beam. The full width at half maximum (FWHM) laser bandwidth is specified as less than  $0.003 \text{ cm}^{-1}$ .

The optics used on the receiving side are summarized in Table 5.6. The integrated slow scan intensified 16-bit CCD camera (14 bits were used) equipped with a f# 1.2, 50 mm focal length

**Table 5.6. Receiving Side Optical Characteristics.**

Camera Type	12 Bit Intensified CCD Camera
Camera Readout Rate	150 kHz
Camera Gate Width	5 ns
Camera Lens	50/1.2 with PK-12 Extension
Field of View	45.5 x 4 mm
GO <sub>2</sub> Interference Filter	Center Wavelength - 581.2 nm; Bandwidth - 8.5 nm
GH <sub>2</sub> Interference Filter	Center Wavelength - 681.0 nm; Bandwidth - 9.7 nm
H <sub>2</sub> O Interference Filter	Center Wavelength - 661.3 nm; Bandwidth - 9.7 nm
GN <sub>2</sub> Interference Filter	Center Wavelength - 608.0 nm; Bandwidth - 9.4 nm

lens, was aligned 90° to the laser beam (see Fig. 5.7). For image analysis, only a portion of the total image (area of 144 x 10 pixels corresponding to a line image field of view of 1.79 x 0.157 in. (45.5 x 4 mm)) corresponding to the laser beam region was utilized. This optical arrangement was iteratively reached and represents a near optimum configuration for signal strength with respect to equipment limitations. For the wavelength of the laser used here ( $\lambda=532$  nm), the center wavelength for the shifted Stokes Vibrational Q-branch signal from  $\text{GO}_2$ ,  $\text{GH}_2$ ,  $\text{GN}_2$  and  $\text{H}_2\text{O}$  species are 580, 681, 607 and 660 nm, respectively [3]. For each species measurement, a 10 nm (nominally; see Table 5.6 for specifics) bandpass filter centered at the aforementioned wavelengths was placed in front of the camera. In addition, for each species measurement, a high pass cutoff filter was placed in front of the camera to further isolate the Raman signal from the Rayleigh scattered light. Note that the choice of the interference filter bandwidth affects the temperature sensitivity of the Stokes bandwidth factor. For example, with Nd:YAG laser (532 nm) excitation for  $\text{GN}_2$  species, the temperature dependence of the Stokes bandwidth factor to interference filter bandwidth shows that a filter centered at 607.3 nm with a bandwidth of 5 nm effectively makes the species measurement temperature independent to within 5% [3]. Alternately, the Stokes bandwidth factor increases non-linearly by about 40% for the  $\text{GN}_2$  species temperature range from 300 to 3000K with a 10 nm bandwidth filter centered at 607.3 nm [3]. Clearly, for species field concentration measurements, the filters should be chosen to make the measurement temperature independent; otherwise careful filter calibration is necessary. For the experiments reported here, off-the-shelf low cost filters were chosen.

#### 5.1.2.2 Injector Face Thermocouple Instrumentation

Temperature measurements of the injector face (injector face plate is made of oxygen-free copper) were made for all injector elements. The temperature was measured with the aid of a type “K” thermocouple silver brazed at a location 0.425 in. from the injector centerline. The temperature measurements were sampled at 200 Hz.

#### **5.1.3 Results and Discussion**

Since the target pressure of 1000 psia was relatively high, initial experiments were first conducted at lower chamber pressures of 300, 500 and 700 psia. These initial experiments indicated extremely high heat transfer rates to the wall for both the O-F-O and F-O-F triplet injector elements (melting in the wall region was observed). However, although the heat transfer

rates for the swirl coaxial injector elements was high, they were not high enough to damage the rocket. Consequently, Raman spectroscopy measurements of the flowfield were made for only the swirl coaxial injector elements.

Temperature measurements of the injector face (injector face plate is made of oxygen-free copper) are shown in Fig. 5.8 for the three swirl coaxial injectors. The temperature was measured with the aid of a type "K" thermocouple silver brazed at a location 0.425 in. from the injector centerline. The temperature measurements sampled at 200 Hz for the 2 sec. duration rocket firings show that the injector face temperature is lowest for the 60° swirl injector, and nominally the same for the 75° and 90° GO<sub>2</sub>/GH<sub>2</sub> swirl angle injector elements. The high injector face temperatures indicate that the energy release for the swirl coaxial injector element is close to the face, and hence, the possible use of this type of injector for actual rocket engines will require injector face cooling schemes that can alleviate the excessive injector face heat transfer rates.

The first set of experiments at a nominal chamber pressure of 1000 psia indicated that due to the large difference in index of refraction between the high temperature GO<sub>2</sub>/GH<sub>2</sub>

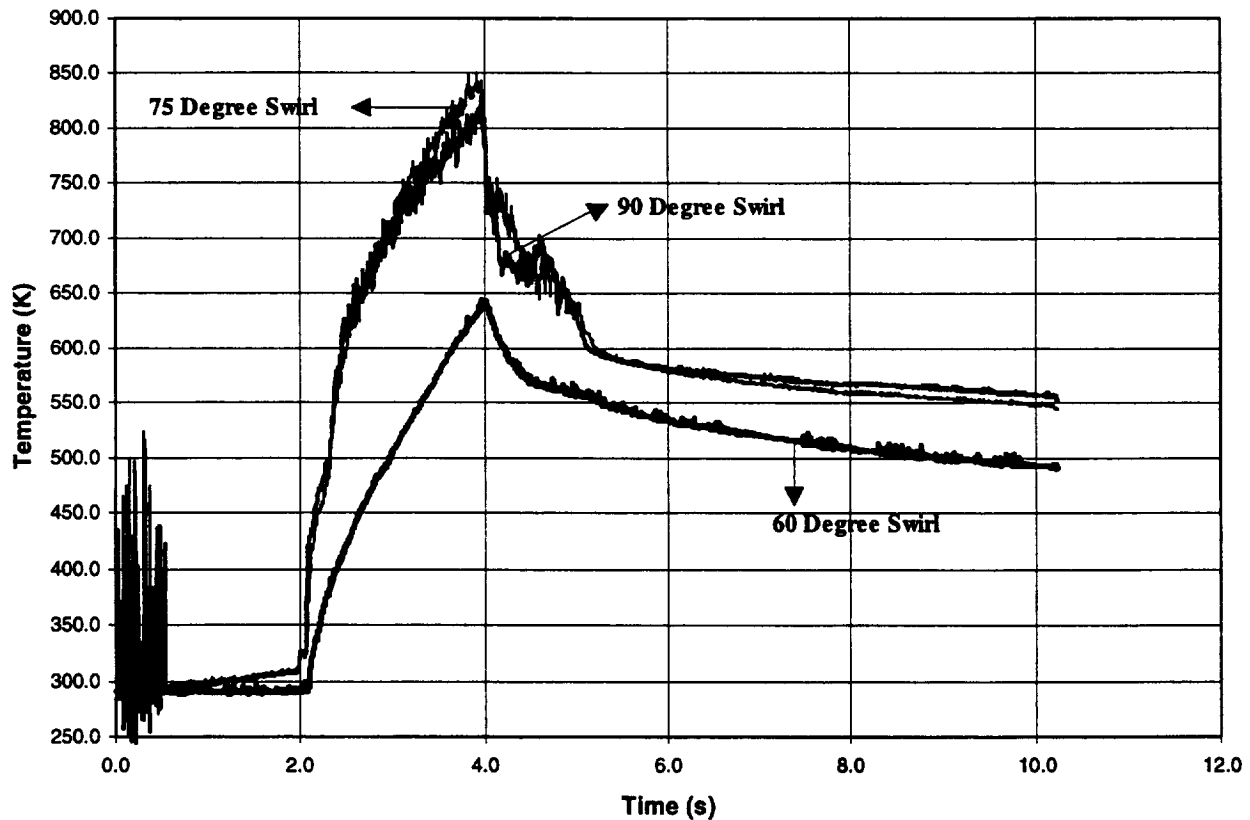


Fig. 5.8. Injector face temperature for the three swirl coaxial injectors. Thermocouple is located 0.425 in. from injector centerline.

combustion products and the cold(er) nitrogen flow employed for purging the window section, the laser beam steered/bloomed through the chamber cross-section and severely compromised the Raman experiments. Fortuitously, helium has an index of refraction close to that of the high temperature  $\text{GO}_2/\text{GH}_2$  combustion products. The experimental results presented next were obtained by using helium instead of nitrogen as the window purge gas. Unfortunately, helium does not have a Raman cross-section due to its monatomic structure, and hence its concentration can not be measured using Raman spectroscopy.

Radial line images of the species Raman signal at an axial location of 3.5 in. from the injector face for the three geometric variations ( $60^\circ$ ,  $75^\circ$ , and  $90^\circ$ ), of the swirl coaxial injector are shown in Figs. 5.9-5.11. In these three figures, both a representative instantaneous image and the averaged image (nominally 10-20 image average) for each measured species, viz.  $\text{GH}_2$ ,  $\text{GO}_2$  and  $\text{H}_2\text{O}$ , are shown. The instantaneous images highlight the highly turbulent nature of the combusting flowfield. Analysis of the instantaneous flow structure in the combusting flowfield was not possible because the current experimental setup only provided the Raman signal from only one species at one time. The averaged images were obtained by averaging the instantaneous images for each species and correcting for both the flame luminosity levels and background scattering. Note that the gray-scales for each species was scaled from minimum to maximum, and therefore the gray-scale should not be used to compare the relative Raman signal strength. The measurements showed that  $\text{GH}_2$  and  $\text{H}_2\text{O}$  were present at all radial locations at the 3.5 in. measurement location. Here, the Raman signal obtained for the  $\text{GO}_2$  measurement setup was “weak”. Furthermore, each instantaneous  $\text{GH}_2$  measurement (of both the vibrational and one of the rotational lines) always showed  $\text{GH}_2$  at all radial locations. Since oxygen and hydrogen cannot occupy the same location at the same time, this suggests that  $\text{GO}_2$  was not present at the 3.5 in. measurement location. The relatively weak signal measured using the  $\text{GO}_2$  measurement setup is believed to be from a rotational line (S-branch) of  $\text{GH}_2$  that can be detected if the gas temperature is high [3]. Hence, for all three geometric variations of the swirl injector, combustion was complete within 3.5 in. from the injector face.

To quantify the Raman spectroscopy measurements, the experimental setup was calibrated for  $\text{GO}_2$  and  $\text{GH}_2$  species at standard temperature and pressure conditions. The experimental setup was also calibrated *in-situ* for  $\text{H}_2\text{O}$  using a steam/ $\text{GN}_2$  flow. The calibrations of the major species provided a basis for extracting the radial profiles of species mole fraction from the corrected

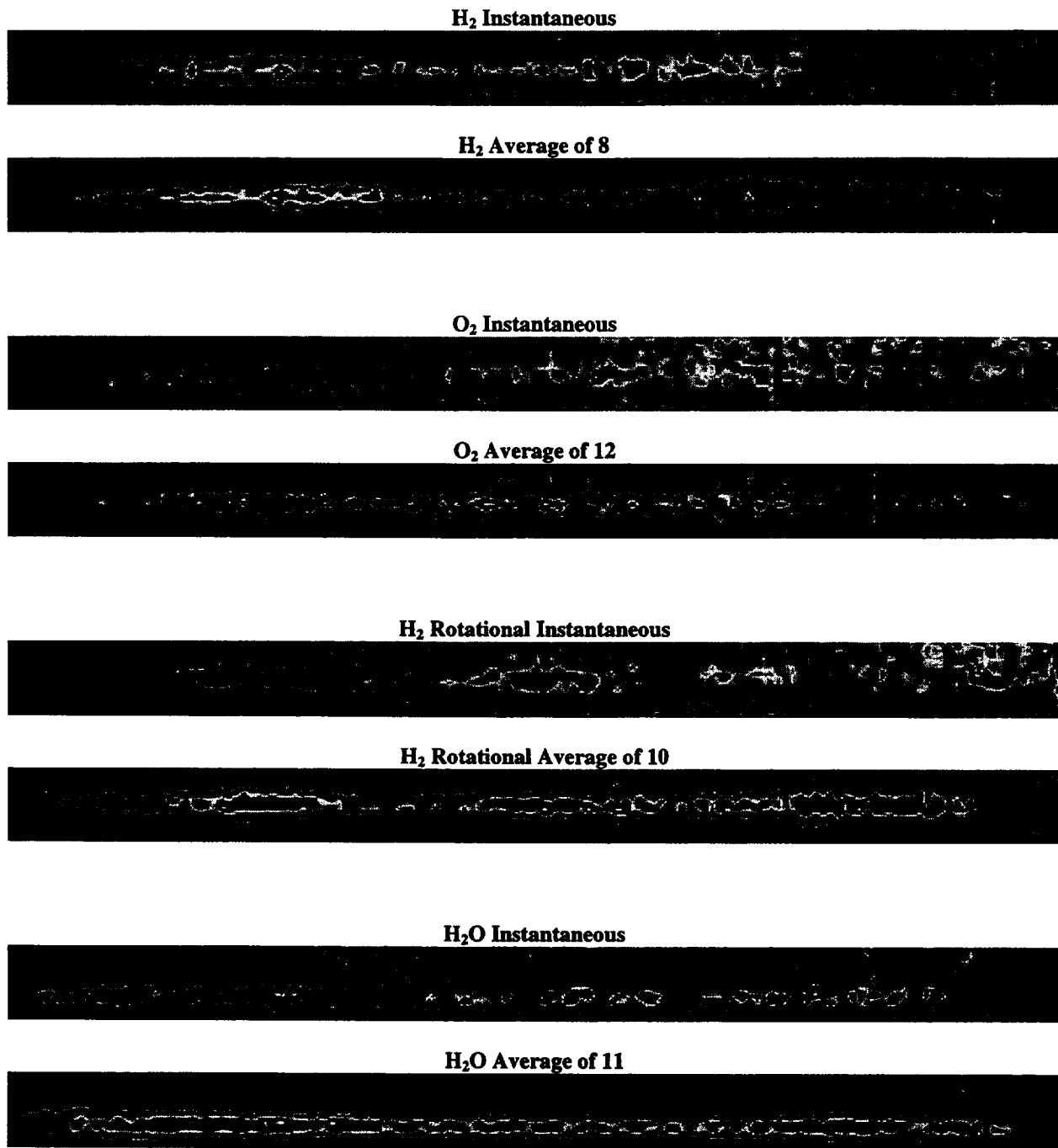


Fig. 5.9. Raman line images of major species for the  $\text{GO}_2/\text{GH}_2$   $60^\circ$  swirl coaxial injector. Radial species profiles are for an axial measurement location of 3.5 in. from injector face at a chamber pressure of 993 psia.. For each species, instantaneous and average images are shown. Note that the  $\text{GO}_2$  signal is not from  $\text{GO}_2$  but is argued to be from a rotational line of  $\text{GH}_2$  that is within the bandwidth of the  $\text{GO}_2$  filter.

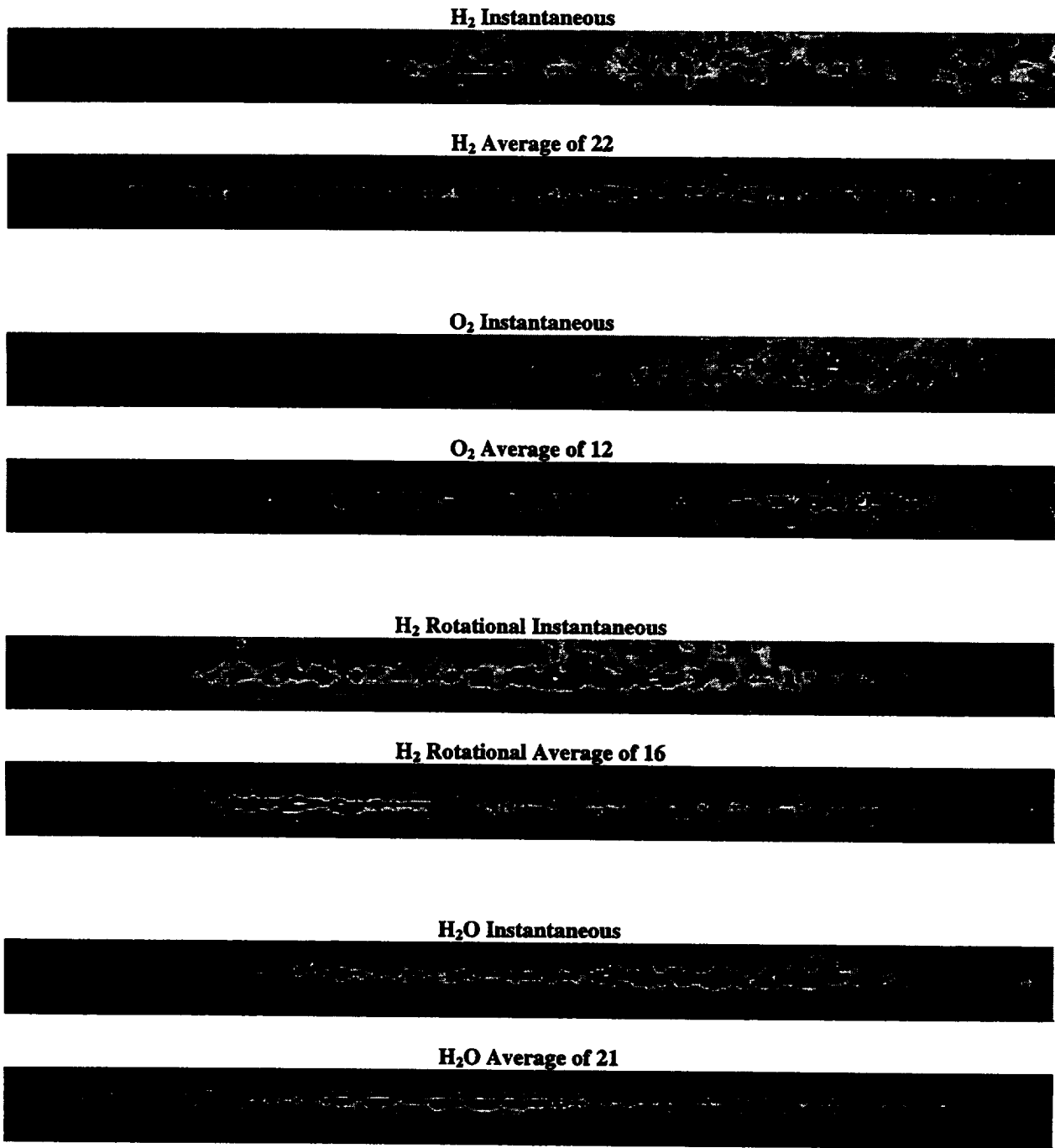
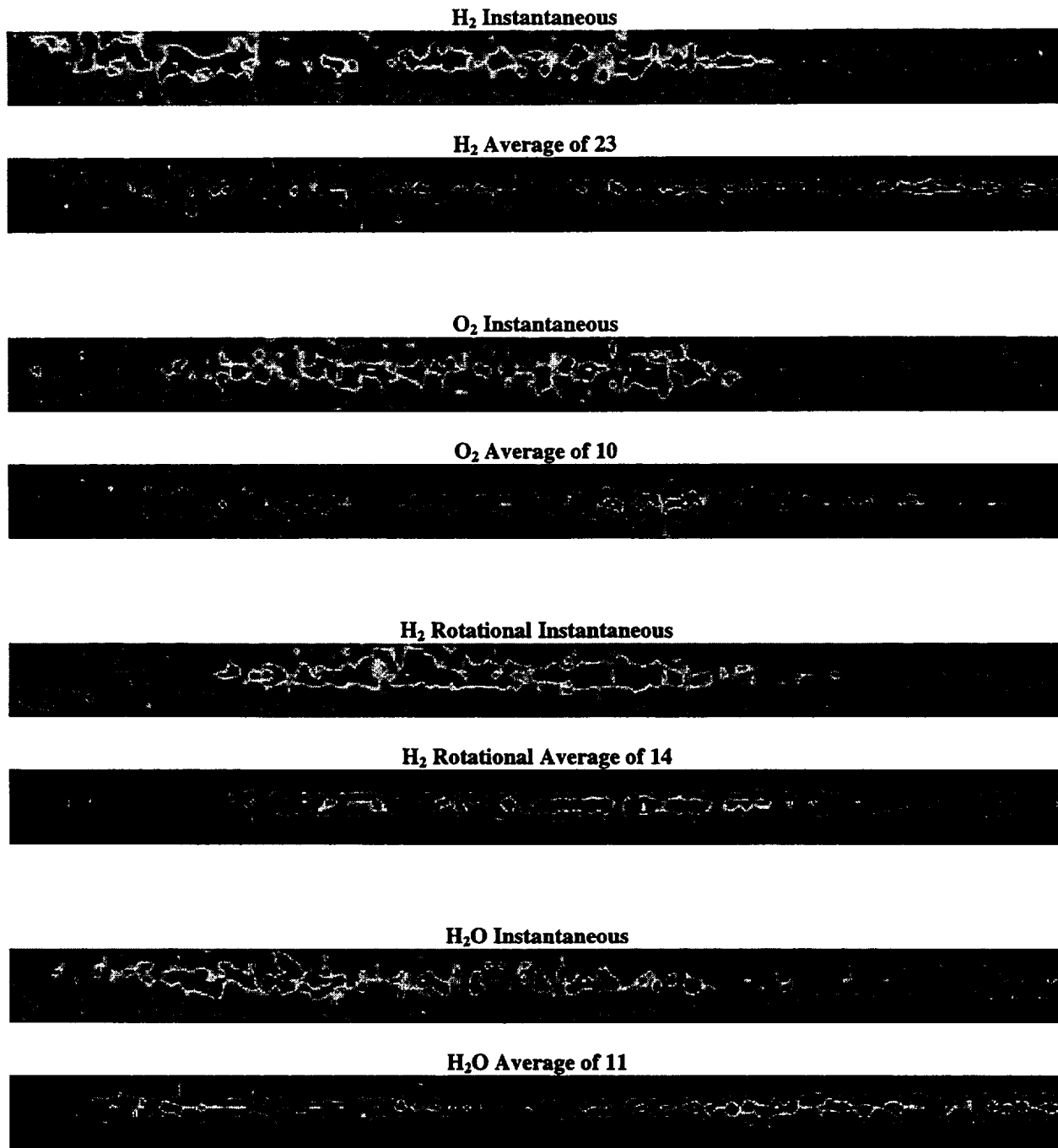
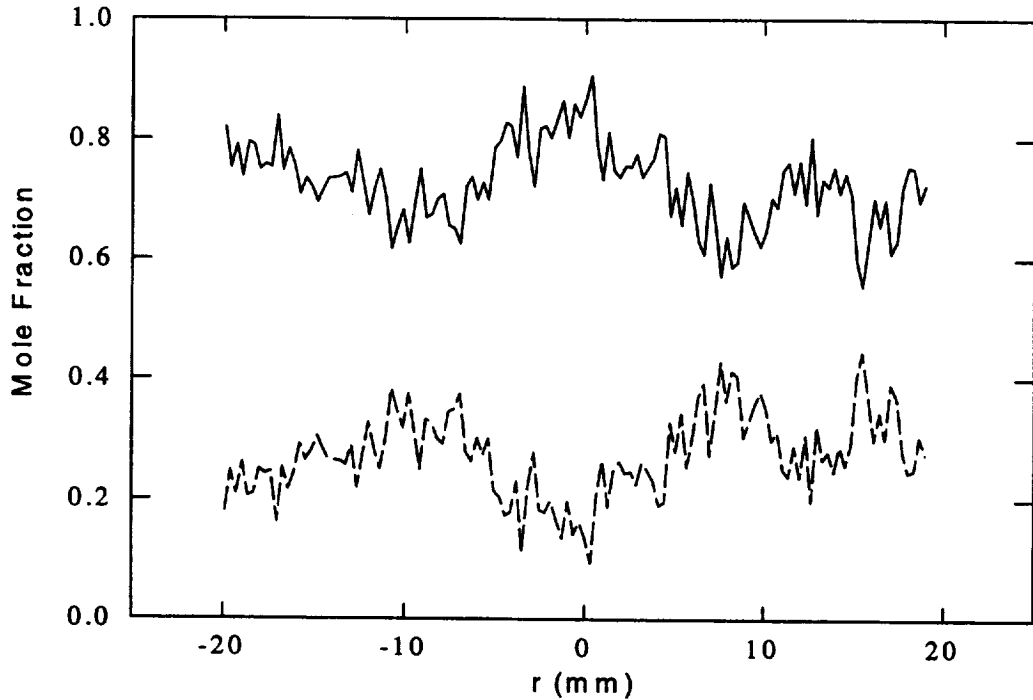


Fig. 5.10. Raman line images of major species for the  $\text{GO}_2/\text{GH}_2$  75° swirl coaxial injector. Radial species profiles are for an axial measurement location of 3.5 in. from injector face at a chamber pressure of 1039 psia.. For each species, instantaneous and average images are shown. Note that the  $\text{GO}_2$  signal is not from  $\text{GO}_2$  but is argued to be from a rotational line of  $\text{GH}_2$  that is within the bandwidth of the  $\text{GO}_2$  filter.



**Fig. 5.11. Raman line images of major species for the GO<sub>2</sub>/GH<sub>2</sub> 90° swirl coaxial injector. Radial species profiles are for an axial measurement location of 3.5 in. from injector face at a chamber pressure of 995 psia.. For each species, instantaneous and average images are shown. Note that the GO<sub>2</sub> signal is not from GO<sub>2</sub> but is argued to be from a rotational line of GH<sub>2</sub> that is within the bandwidth of the GO<sub>2</sub> filter.**



**Fig. 5.12.** Average  $\text{GH}_2$  and  $\text{H}_2\text{O}$  mole fraction radial profiles at an axial measurement location of 3.5 in. from injector face for  $60^\circ$  swirl injector. Mole fraction results are obtained from the Raman line images shown in. Fig. 5.9.  $P_c=993$  psia.

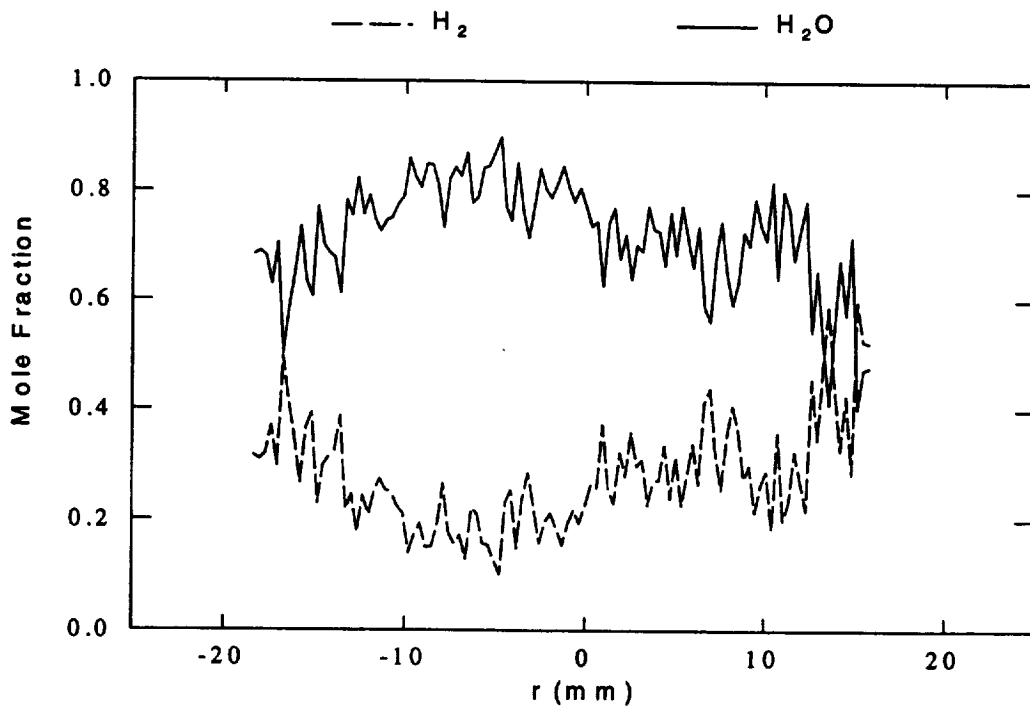


**Fig. 5.13.** Average  $\text{GH}_2$  and  $\text{H}_2\text{O}$  mole fraction radial profiles at an axial measurement location of 3.5 in. from injector face for  $75^\circ$  swirl injector. Mole fraction results are obtained from the Raman line images shown in. Fig. 5.10.  $P_c=1039$  psia.

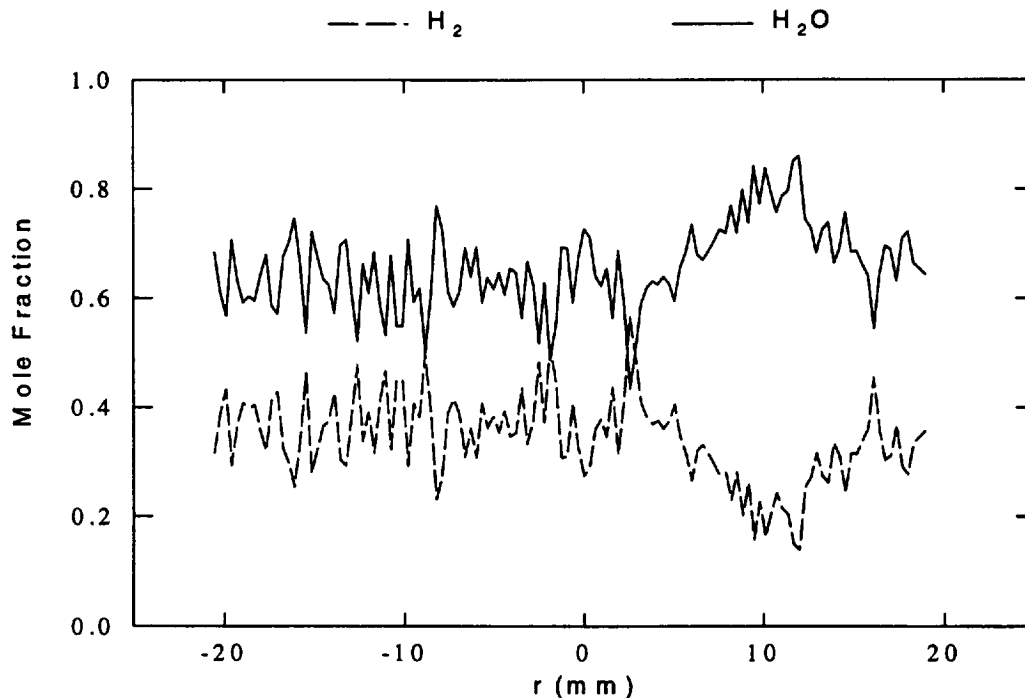


**Fig. 5.14. Average  $\text{GH}_2$  and  $\text{H}_2\text{O}$  mole fraction radial profiles at an axial measurement location of 3.5 in. from injector face for  $90^\circ$  swirl injector. Mole fraction results are obtained from the Raman line images shown in Fig. 5.11.  $P_c=995$  psia.**

average Raman images described earlier, as shown in Figs. 5.12-5.14 for the tested swirl coaxial injectors. The species mole fraction results are semi-quantitative since the Stokes bandwidth factor for the filters used for the experiment was temperature dependent. The results showed that all three species were nearly uniformly distributed in the radial direction indicating that combustion was complete or near-completion. Clearly, these measurements show that the swirl coaxial injector element is an efficient injector in terms of its mixing, combustion and performance characteristics. However, from the Raman measurements at one axial location, viz. 3.5 in. from the injector face, the superiority of one geometric variation over the others can not be quantified. The injector face temperature measurements indicated that increased  $\text{GO}_2$  swirl levels promote mixing and combustion, and hence it is expected that, in contrast to the  $60^\circ$  swirl injector, combustion is complete closer to the injector face for the  $90^\circ$  swirl injector. In any case, the results indicate that the generic swirl injector is an efficient injector, and actual implementation of this type of injector will require trade off studies between injector face temperature requirements and mixing/combustion efficiency limits, i.e. necessary chamber length to achieve complete combustion.

## **5.2 SECOND PHASE OF EXPERIMENTATION**

The first set of experiments for the swirl coaxial injector showed that although mixing and combustion was complete close to the injector face, the face heat flux was very high. Based on these results involving the swirl coaxial injector element, the GGIT team decided to investigate the shear coaxial injector element for the second phase of experimentation. The experiments conducted for this phase again investigated the mixing and combustion characteristics of the injector with the aid of Raman spectroscopy.

### **5.2.1 Experimental Setup**

The GGIT team decided that the flowfield characteristics for various geometrically different shear coaxial injector elements needed to be studied for the second phase of experimentation. Four geometric variations of the shear coaxial injector elements were designed for implementation in the optically-accessible rocket chamber described in Chapter 2. (see Fig. 2.1 for details).

#### **5.2.1.1 Flow Conditions**

The shear coaxial injector element geometries were designed for gaseous oxygen/gaseous hydrogen flow at a mixture ratio of six. The target chamber pressure was 1000 psia for oxygen and hydrogen flowrates of 0.25 lbm/s and 0.042 lbm/s, respectively.

#### **5.2.1.2 Shear Coaxial Elements**

The design phase of the shear coaxial injector elements involved vigorous discussions between all GGIT team members. The discussion led to the decision that four shear coaxial injector elements with gaseous hydrogen to gaseous oxygen velocity ratios between 4 and 8 needed to be designed and fabricated. The common parameters for all four geometric variations of the injector element are summarized in Table 5.7. Based on these common parameters, four shear coaxial injector elements were designed and fabricated. The specifics of each design are presented in Table 5.8.

### **5.2.2 Raman Spectroscopy Setup**

Raman spectroscopy was employed as the major diagnostic technique for characterizing the mixing and combustion characteristics of the flowfield. During the time period between the first and second phases of experimentation, the technique had been further refined. Specifically,

**Table 5.7. Common Parameters For All Shear Coaxial Injectors**

Chamber Pressure	1000 psia
GO <sub>2</sub> mass flowrate	0.1134 kg/s (0.25 lbm/s)
GH <sub>2</sub> mass flowrate	0.0189 kg/s (0.0417 lbm/s)
GO <sub>2</sub> /GH <sub>2</sub> mass flow ratio	6
Temperature of GO <sub>2</sub>	300 K
Temperature of GH <sub>2</sub>	300 K
Density of GO <sub>2</sub>	91 kg/m <sup>3</sup> (5.68 lb/ft <sup>3</sup> )
Density of GH <sub>2</sub>	5.37 kg/m <sup>3</sup> (0.335 lb/ft <sup>3</sup> )
C <sub>d</sub> of GO <sub>2</sub> flow	0.85
C <sub>d</sub> of GH <sub>2</sub> flow	0.92

in contrast to the earlier implementation of the technique with filters for each species, the technique now employed a spectrometer. The major gain with this new setup was due to the possibility of *simultaneously* measuring all major species.

A schematic of the improved Raman system is shown in Fig. 5.15. A Q-switched, frequency doubled Nd:YAG laser operating at 5 Hz was used as the 532 nm excitation source. The laser power output was measured to be about 300 mJ/pulse. The laser pulse polarization was rotated from the vertical to horizontal direction via two mirrors immediately following the laser. This allowed the collection optics to be in the correct polarization orientation. The laser beam was passed through the window section that separates the test cell from the instrument cell and reflected by two mirrors to position it in line with the rocket window section. The laser beam was focused to a 500 μm diameter at the center of the rocket cross section by an f=0.75 m

**Table 5.8. Shear Coaxial Injector Designs**

	Injector # 1	Injector # 2	Injector # 3 (Baseline)	Injector # 4
Inner diameter of GO <sub>2</sub> post (in.)	0.173	0.173	0.173	0.173
Inner diameter of GH <sub>2</sub> annulus (in.)	0.203	0.203	0.203	0.203
Outer diameter of GH <sub>2</sub> annulus (in.)	0.227	0.231	0.235	0.249
Velocity of GO <sub>2</sub> (ft/s)	270	270	270	270
Velocity of GO <sub>2</sub> (m/s)	82	82	82	82
Velocity of GH <sub>2</sub> (ft/s)	2208	1875	1626	1096
Velocity of GH <sub>2</sub> (m/s)	673	572	496	334
GH <sub>2</sub> /GO <sub>2</sub> velocity ratio	<b>8.19</b>	<b>6.96</b>	<b>6.03</b>	<b>4.07</b>
Pressure drop of GO <sub>2</sub> (psid)	61.7	61.7	61.7	61.7
Pressure drop of GH <sub>2</sub> (psid)	208.4	150.3	113.0	51.4

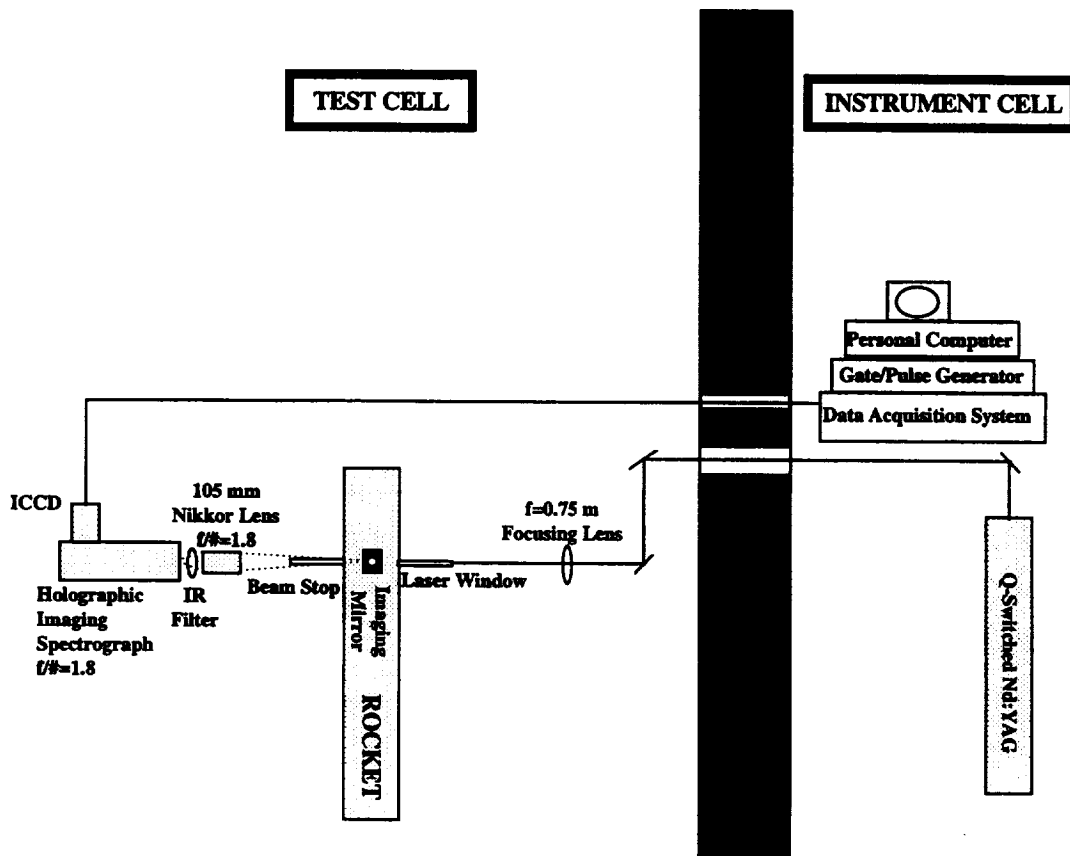


**Fig. 5.15. Schematic of improved Raman set-up with spectrometer for simultaneous measurement of all major species.**

focusing lens. A linewise Raman image of the flame front was projected by a 3 in. diameter mirror placed above the rocket window section. The image was gathered and focused by an  $f/\#$  1.8, 105 mm Nikkor lens. An  $f/\#$  1.8 Kaiser Optic holographic imaging spectrograph in conjunction with an intensified charge-coupled device (ICCD, 576x384 pixel) camera was used to capture the Raman signals of major combustion species ( $H_2$ ,  $O_2$ ,  $H_2O$ ). The system allowed simultaneous multi-species multi-point Raman measurements. The slit width of  $500\ \mu\text{m}$  and binning of four pixels in the radial dimension, corresponding to the 384 pixel direction, and of six pixels in the wavelength dimension, corresponding to the 576 pixel direction were used. The Raman signal-to-noise ratio was increased by discriminating against the Rayleigh interference by using of a notch filter centered at 532 nm (FWHM  $\approx$  18 nm) placed inside the spectrograph. The intense flame interference was reduced 50% by using a linear dichroic sheet polarizer aligned with the Raman signal polarization.

### 5.2.3 Results and Discussion

The averaged and background luminosity corrected Raman signals at the axial measurement location of 5 in. from the injector face for the four geometric variations (see Tables 5.7 and 5.8 for details), of the shear coaxial injector are shown in Figs. 5.16. In these measurements, the abscissa represents wavelength of light, whereas the ordinate represents radial location. The central ordinate location corresponds to the axis of the shear coaxial injector element. The wavelength locations of oxygen, hydrogen and water vapor are indicated in one of the results. The averaged images were obtained by averaging multiple instantaneous images for each flow condition and correcting for both the flame luminosity levels and background scattering. Note that the scale for each of the results is consistent, and therefore, the levels can be compared between the different results. The measurements showed that  $\text{GO}_2$  always prevails in the central part of the flowfield. Comparison of the results for the four gaseous hydrogen to gaseous oxygen velocity ratio cases shows that the least amount of oxygen is present for the highest velocity ratio

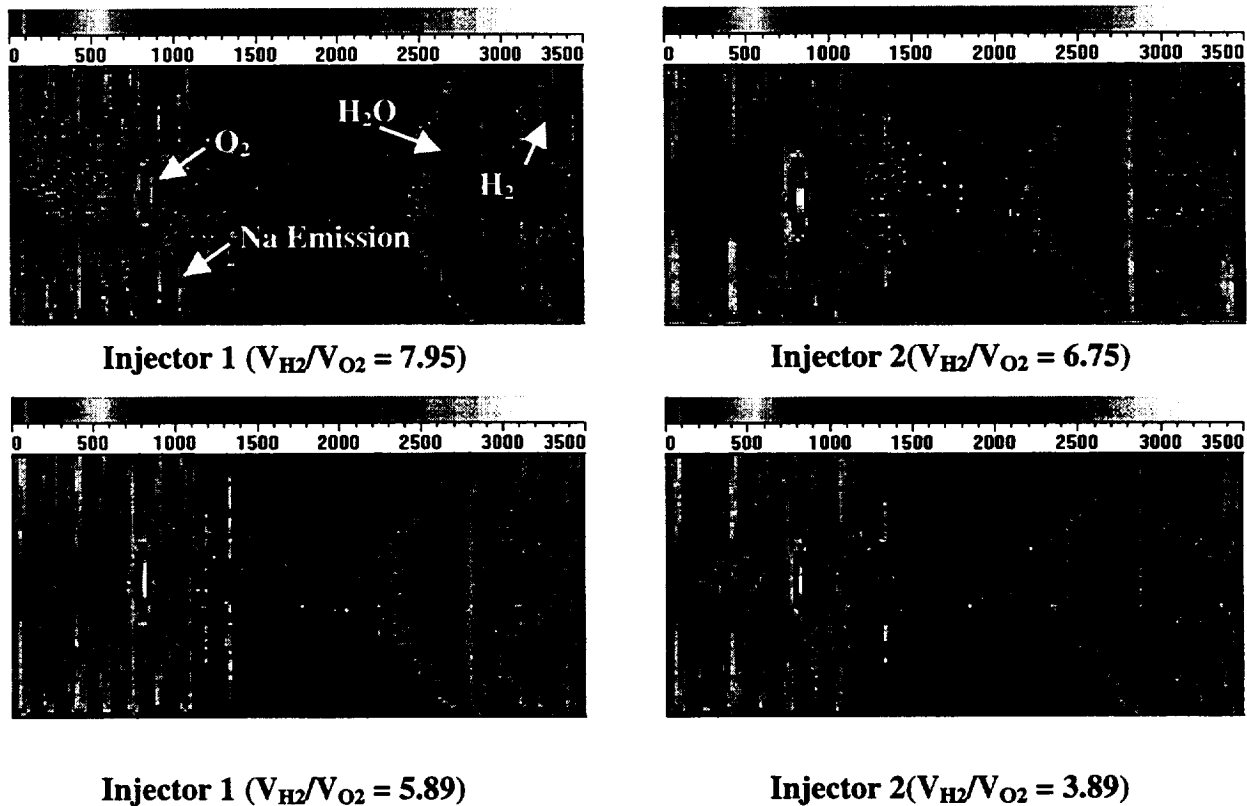


**Fig. 5.16.** Comparison of flame background corrected averaged Raman species measurements for four geometric variations of the shear coaxial injector. For target flow conditions, see Tables 5.7 and 5.8.

case (velocity ratio of 8). This is consistent with the realization that mixing, and consequently combustion, increases with increasing hydrogen to oxygen velocity ratio. The results also indicate the presence of  $H_2$  and  $H_2O$  away from the central region of the flowfield. Complementary face temperature measurements (not shown here) indicate a moderate temperature increase of about 100 K for all studied shear coaxial injector geometries. These results clearly indicate that the mixing and combustion processes for the shear coaxial injector in an uni-element configuration are relatively gradual.

## VI LIQUID OXYGEN/GASEOUS HYDROGEN SHEAR COAXIAL INJECTOR STUDIES

The steady state combustion process in a bi-propellant liquid rocket engine includes liquid propellant injection, atomization, vaporization, mixing with its counterpart propellant that is either injected in gas phase or is vaporized in a similar manner, and finally, combustion. The process starts with the injection and subsequent atomization of the liquid propellant, and this mechanism in turn defines the flowfield and combustion characteristics in the rocket chamber. The fluid injection and atomization process involves the use of a manifold of injectors, with the type of injector usually dictated by propellant type and combustion stability considerations. Historically, for the liquid oxygen (LOX)/gaseous hydrogen (GH<sub>2</sub>) propellant combination, the element of choice has been the shear coaxial injector, although recently the swirl coaxial injector has been proposed as an alternative/advancement because of its enhanced atomization characteristics. The shear coaxial injector has been successfully used in the J-2, RL10A-1 and Space Shuttle Main Engine (SSME) [24] and the swirl coaxial injector has been used in the RL10A-3 [24] and is also proposed for next generation launch vehicles [25].

Understanding the physics of the atomization process for a particular injector is critical for understanding the subsequent dynamics of vaporization, mixing and combustion. For the case of the shear coaxial injector, the current phenomenological model views atomization to occur through a mechanism involving the stripping of drops from a liquid core (e.g., liquid oxygen) surrounded by a high velocity shearing gas flow (e.g., hydrogen). The number and size of the drops is viewed to be determined by a combination of aerodynamic instability wave growth and the turbulent structure of the liquid core [26,27]. Although qualitatively this phenomenological view appears reasonable, there are few direct measurements to provide a quantitative representation of the important atomization processes and the resulting drop field present in the combustor. This level of understanding can only be obtained by experiments that detail both the evolving drop size/velocity fields and the gas phase velocity field under combusting conditions, and theoretical models based on first principles that corroborate the measurements.

Currently, the data base for drop size/velocity fields under combusting conditions is minimal. Consequently, atomization models for predicting initial drop size distributions, which are incorporated in computational fluid dynamics (CFD) codes for predicting the steady state

combustion phenomena, are either based on analytical treatments such as linear stability theory or extrapolations of parametric correlations of drop size obtained for cold flow conditions [28-30]. A data base of drop size distribution data for combusting conditions is therefore critical for verifying/refuting both atomization models and the practice of extrapolating drop size correlations obtained for cold flow conditions to predict drop size for combusting conditions. It is important to realize that the physical parameter space in terms of pressure, temperature, Reynolds number and Weber number for typical cold flow experiments is significantly different from that found for combusting conditions. Finally, a drop size distribution data base for combusting conditions could be used for developing correlations that are directly input into CFD codes.

The number of experiments designed in the past to address this void in drop size data for combusting conditions is minimal because of the general lack of diagnostic techniques capable of probing the harsh environment in a liquid propellant rocket chamber, the safety aspects that have to be strictly adhered to in handling propellants that range from hypergolic to cryogenic fluids and the expensive nature of these experiments. To the authors' knowledge, the experiments reported by George [31,32] and Ingebo [33] are the only programs that have attempted to address the need for drop size data under combusting conditions.

George measured drop sizes using holographic images of the spray formed from a uni-element like-on-like impinging doublet injector in a transparent side-walled thrust chamber. The propellant combination was gaseous  $N_2O_4$  oxidizer injected through holes on the face plate and liquid  $N_2H_4$  fuel injected through a doublet injector to form the drop cloud. George [31,32] also conducted complementary cold flow experiments using water and nitrogen as simulants and his comparisons of the two sets of drop size measurements showed significant differences between the measured drop sizes for the two conditions. Clearly, it is very difficult to match all the important parameters between cold flow and hot-fire conditions. Thus, the differences observed in the studies by George [31,32] for these differing environments is not surprising. Ingebo's [33] experiment involved using ultra high speed microphotography to record a combusting LOX/ethanol spray in a chamber. The LOX and ethanol were injected through a like doublet element and two rows of holes in the injector faceplate, respectively. From the microphotographs, Ingebo [33] measured the size of ethanol drops. Since cold flow experiments have traditionally been used to derive drop size correlations used in rocket engine design, there is a need for hot-fire experiments under rocket

chamber conditions to establish the proper scaling, if one exists, between cold flow and hot-fire results.

In the last decade, phase Doppler interferometry [34-35] has advanced to a stage where temporally-averaged drop size distributions as a function of spatial position can be obtained in harsh environments. Researchers have used this technique for measuring drop size and velocity in sprays ranging from oil burner to diesel applications [36]. This technique has also been used to characterize the drop field in sprays formed by rocket injectors for cold flow conditions, where simulants are used instead of actual propellants (for example, Refs. 37-40). In addition, Goix et al. [41] have recently used this technique for measuring drop size in a methanol/air flame from a coaxial injector.

The present effort is geared towards systematically mapping the drop size field downstream of a shear coaxial injector in a rocket chamber that combusts gaseous hydrogen with liquid oxygen. Measurements of LOX drop size under combusting conditions made using the phase Doppler particle interferometry technique are presented. These LOX drop sizing experiments are also complemented by a set of qualitative Mie scattering experiments that were conducted to elucidate the overall fluid dynamic nature of the flowfield.

## **6.1 EXPERIMENTAL SETUP**

The rocket chamber used for these experiments is the same one as described in Chapter 2. A shear coaxial injector element was utilized for the set of experiments described here. Note that the geometry of this shear coaxial injector element differs from the one used for the gaseous oxygen/hydrogen experiments discussed in the last chapter.

### **6.1.1 Injector Geometry**

The schematic of the shear coaxial injector used for the LOX/GH<sub>2</sub> experiments is shown in Fig. 6.1. The inner diameter of the LOX post ( $d$ ) was 3.43 mm (0.135 in.). The LOX post was not recessed with respect to the injector face. The inner diameter of the fuel annulus was 4.19 mm (0.165 in.) and the outer diameter was 7.11 mm (0.28 in.).

### **6.1.2 Flow Conditions**

Experiments were conducted at the same flowrate but at two chamber pressure conditions. The detailed flow conditions are presented in Table 6.1. The setting/monitoring of the flowrate of

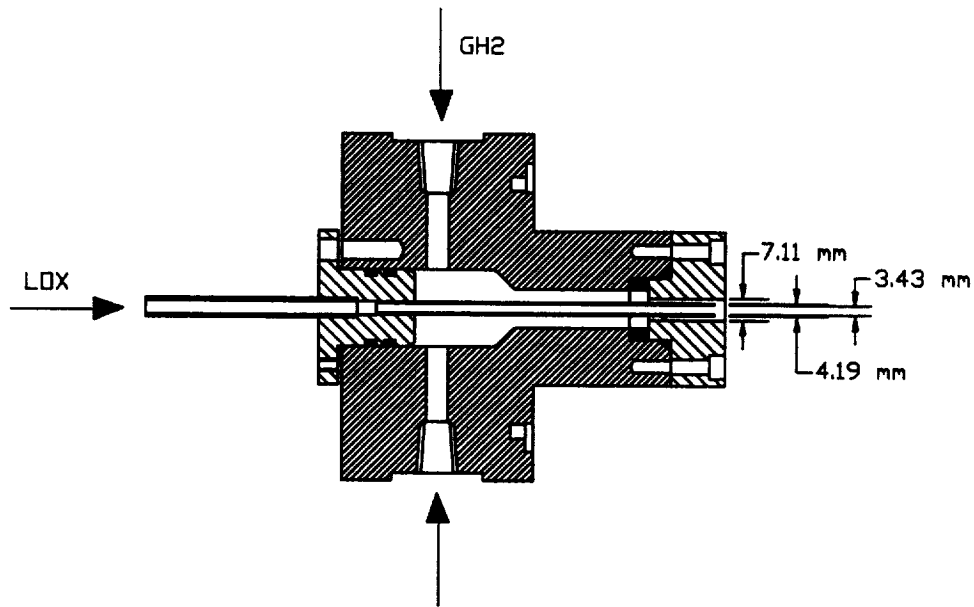


**Fig. 6.1. Schematic of the shear coaxial injector for LOX/GH<sub>2</sub> experiments.**

the gaseous (GH<sub>2</sub>) and liquid (LOX) propellants was accomplished with the aid of a critical orifice and a cavitating venturi, respectively, that were instrumented at both upstream and downstream locations with pressure transducers and thermocouples. The duration of a test run was 4.0 seconds. The chosen test duration represented a compromise between the time required to achieve steady-

**Table 6.1. Flow Conditions for LOX/GH<sub>2</sub> Experiments.**

	CASE 1	CASE 2
LO <sub>2</sub> Mass Flowrate	0.168 kg/s (0.37 lbm/s)	0.168 kg/s (0.37 lbm/s)
GH <sub>2</sub> Mass Flowrate	0.034 kg/s (0.074 lbm/s)	0.034 kg/s (0.074 lbm/s)
Chamber Pressure	1.86 MPa (270 psia)	2.79 MPa (405 psia)
LO <sub>2</sub> Injection Velocity	18 m/s (59 ft/s)	18 m/s (59 ft/s)
GH <sub>2</sub> Injection Velocity	840 m/s (2760 ft/s)	562 m/s (1840 ft/s)
O/F Ratio	5	5
GH <sub>2</sub> /LO <sub>2</sub> Velocity Ratio	47	31
GH <sub>2</sub> /LO <sub>2</sub> Momentum Ratio	9.3	6.1
LOX Reynolds Number	$5.7 \times 10^5$	$5.7 \times 10^5$
Weber Number	$4.4 \times 10^5$	$2.8 \times 10^5$
Chamber Mach Number	0.06	0.04
Mean Chamber Velocity	100 m/s (327 ft/s)	64 m/s (210 ft/s)

state chamber pressure and quartz window survivability. For the tests, it conservatively took less than 0.5 seconds for the chamber pressure to stabilize.

## **6.2 EXPERIMENTAL DIAGNOSTICS**

Two optical techniques were utilized for characterizing the flowfield for the LOX/GH<sub>2</sub> experiments. The first technique utilized was Mie scattering for qualitative interrogation of the flowfield, whereas the second technique was phase Doppler interferometry for LOX drop size and velocity measurements. The details of these two techniques are presented next.

### **6.2.1 Drop Mie Scattering**

The LOX flow field was visually characterized using a laser sheet technique. These experiments provided information on the fluid dynamics of the LOX core breakup process. A laser sheet (width nominally less than 0.02 in. (0.5 mm)) formed from the continuous wave beam of an argon-ion laser ( $\lambda=514.5$  nm) was introduced through one of the slot windows. The laser power for the tests was set between 0.8 and 1.2 W. A Princeton Instruments intensified Charged Coupled Device (CCD) camera equipped with a 1 nm bandpass filter centered at 514.5 nm was used to record the scattered light from the LOX during combustion through one of the circular windows. The bandpass filter was used to reject light from the luminous flame. Images of the flame front taken with and without the laser sheet indicated that with the 1 nm bandpass filter, the light from the luminous flame collected by the camera was less than 5% of the laser light scattered by the LOX. Images of the light scattered by the LOX were taken at 3  $\mu$ s camera gate time at a repetition rate of about three images per second. The nominal inlet velocity of the LOX jet into the chamber was about 20 m/s and hence, it is evident that the first gate time of 3  $\mu$ s realizes instantaneous images.

### **6.2.2 Phase Doppler Interferometry**

The Phase Doppler Particle Analyzer (PDPA) is a commercially available instrument capable of measuring liquid drop size and velocity based on phase Doppler interferometric theory [34,35]. The PDPA instrument was used to measure LOX drop size and velocity in the above described rocket chamber under combusting conditions. The PDPA is a point measurement technique that has been used extensively over the last decade by several researchers (for example, Refs. 34-42). The PDPA instrument extends the basic principles of the conventional dual beam

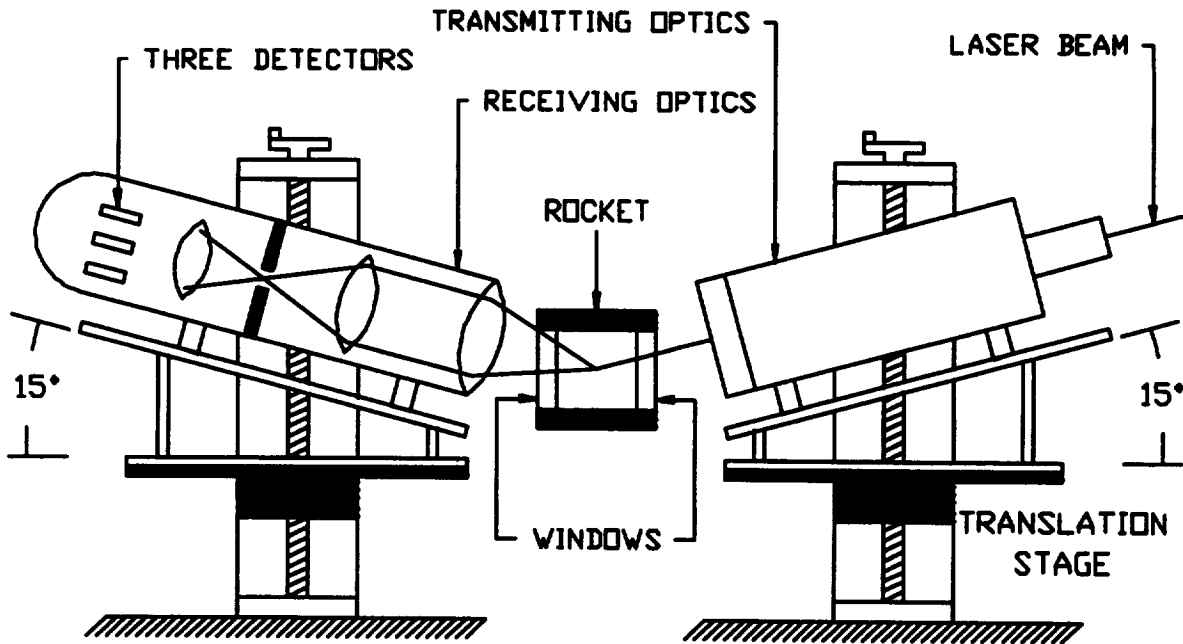


Fig. 6.2. Setup for phase Doppler interferometry.

laser Doppler velocimeter to obtain particle size in addition to velocity. An argon-ion laser beam is split into two equal intensity beams and focused to an intersection to form a probe volume as shown in Fig. 6.2. For the present experiment, the receiver system was located at a  $30^\circ$  off axis angle from the forward propagation vector of the laser beam to best exploit the characteristics of the interference pattern of the refractive LOX drops. This was achieved by inclining both the transmitting and receiving optics at a  $15^\circ$  angle, thus resulting in a net  $30^\circ$  off-axis angle. A 10 nm bandpass filter centered around 514.5 nm was placed in front of the collection optics to reject light from the luminous flame. Note that the collection optics of the receiving system coupled with the transmitting optics define the probe volume characteristics. In addition to the collection optics, the receiving system consists of three detectors at appropriate separations that independently measure the burst signal generated by drops traversing the probe volume, albeit with a phase shift. The velocity of the particle is then extracted from the temporal frequency of the burst signal, whereas the particle size is calculated from the measured phase shift between any two detectors and the *a priori* calculated linearity between the detector separation and the phase angle. The index of refraction of the liquid drop being measured enters into this analysis, and is 1.221 for LOX [43].

### 6.3 RESULTS AND DISCUSSION

Instantaneous images (gate time of 3  $\mu$ s) of the light scattered from the LOX in the near injector region for flow conditions corresponding to Case 1, Table 6.1 are shown in Fig. 6.3. In these images, the flow is from left to right with the laser sheet illuminating the spray field from top to bottom. From left to right, the images are for zero to two inches, two to four inches and five to seven inches downstream of the injector face. The gain of the camera and the power level of the laser were adjusted to exploit the entire dynamic range of the camera (12 bit; maximum level of 4096). Hence the dark spots evident in the images represent locations where the pixels were saturated.

The first image corresponding to the first two inches downstream of the injector face shows that the LOX region is confined to a narrow circumferential region. It is not exactly clear as to whether the image is of an intact LOX core. There are noticeably coherent "sinusoidal" LOX structures in the image that are separated by small dark regions. It is not clear whether the dark regions represent a break in the structures or simply indicate that the structures are out of the plane of the laser sheet. The middle image corresponding to two to four inches downstream of the injector face shows that with downstream distance, the width of the LOX region increases and seems to be manifested by streamwise ligament like structures surrounded by a "grainy" structure which could be construed as LOX drops. Other images at the same flow conditions (not included here) show similar structures. The "grainy" structure surrounding the central region at the two to four inch downstream location is prevalent for all obtained images, a feature that is more pronounced than for any of the images at the zero to two inch location. However, there is no clear indication of a well defined breakup length (i.e. with a small standard deviation) which suggests that

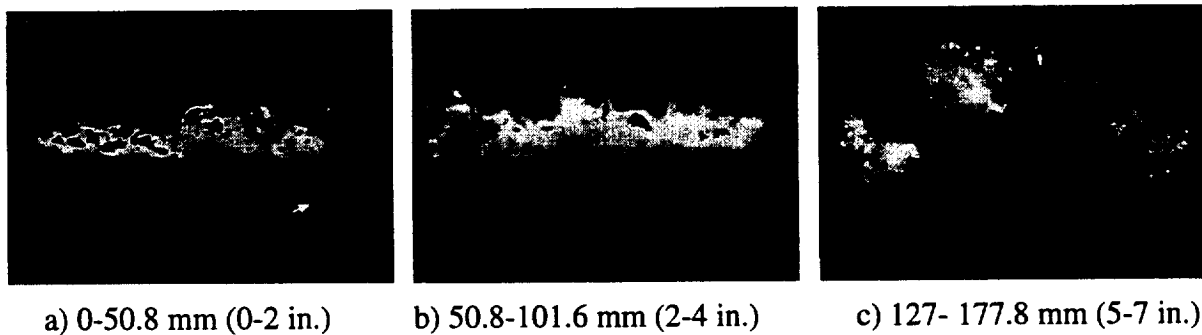


**Fig. 6.3. Instantaneous images (3ms) of the developing LOX flowfield downstream of the shear coaxial injector in the optically accessible rocket chamber. Images correspond to Case 1, Table 6.1. Flow direction is from left to right.**

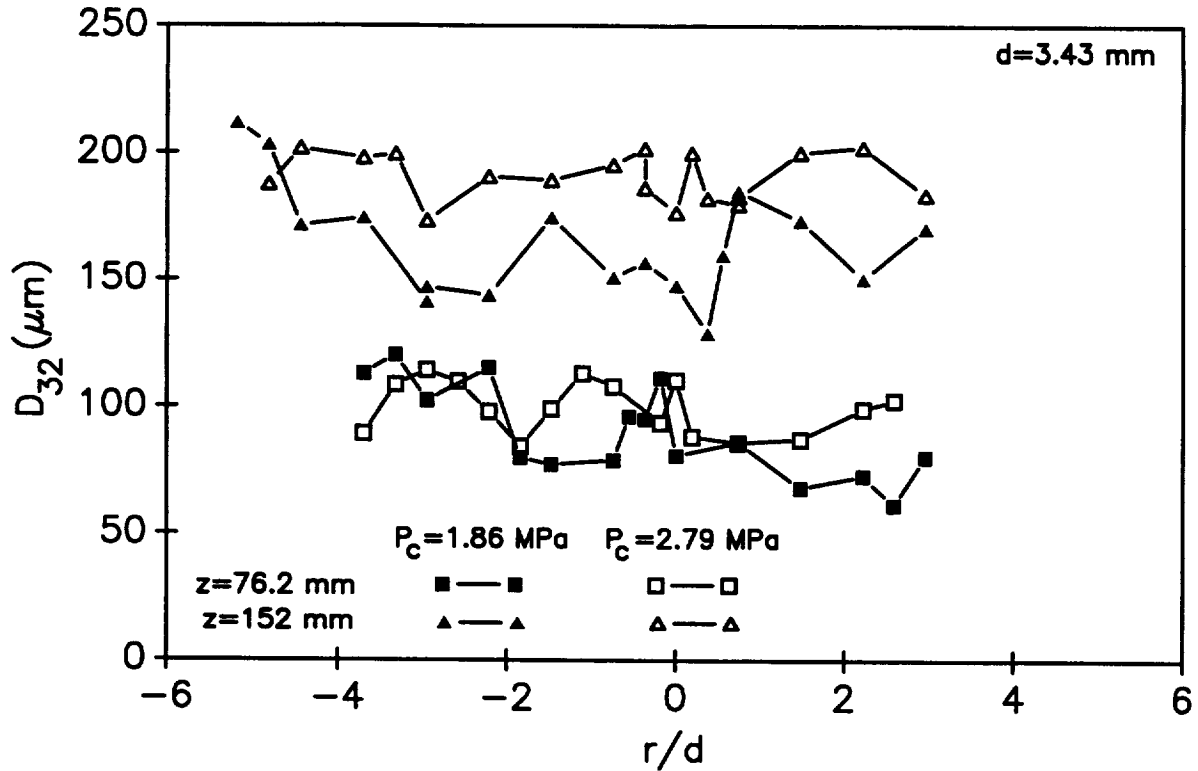


**Fig. 6.4. Radial variation of Sauter mean diameter ( $D_{32}$ ) for test cases 1 and 2, Table 6.1. Axial measurement locations are indicated in the figure.**

the "physical" model for the atomization process is simplistic and at best, qualitative. Further downstream at the five to seven inch location, the image is manifested by what appears to be clouds of ligaments/drops travelling in the streamwise direction in a sinusoidal manner.

Drop size measurements were made in the flowfield described above using the phase Doppler interferometric technique. The commercially available PDPA instrument [33,34] was used to map the radial profiles of drop size and velocity at two axial locations, viz. 76.2 and 152.4 mm (3 and 6 in.) from the injector face corresponding to the middle locations of the middle and last images shown in Fig. 6.3, respectively. Note that each point represents measurements corresponding to a 4 second duration rocket firing. The radial profiles of measured Sauter mean diameter and mean drop velocity at the two axial measurement locations corresponding to the two chamber pressure conditions of test cases 1 and 2 of Table 6.1 are shown in Figs. 6.4 and 6.5, respectively. In the two figures, the radial dimension is non-dimensionalized with respect to the LOX post inner diameter.

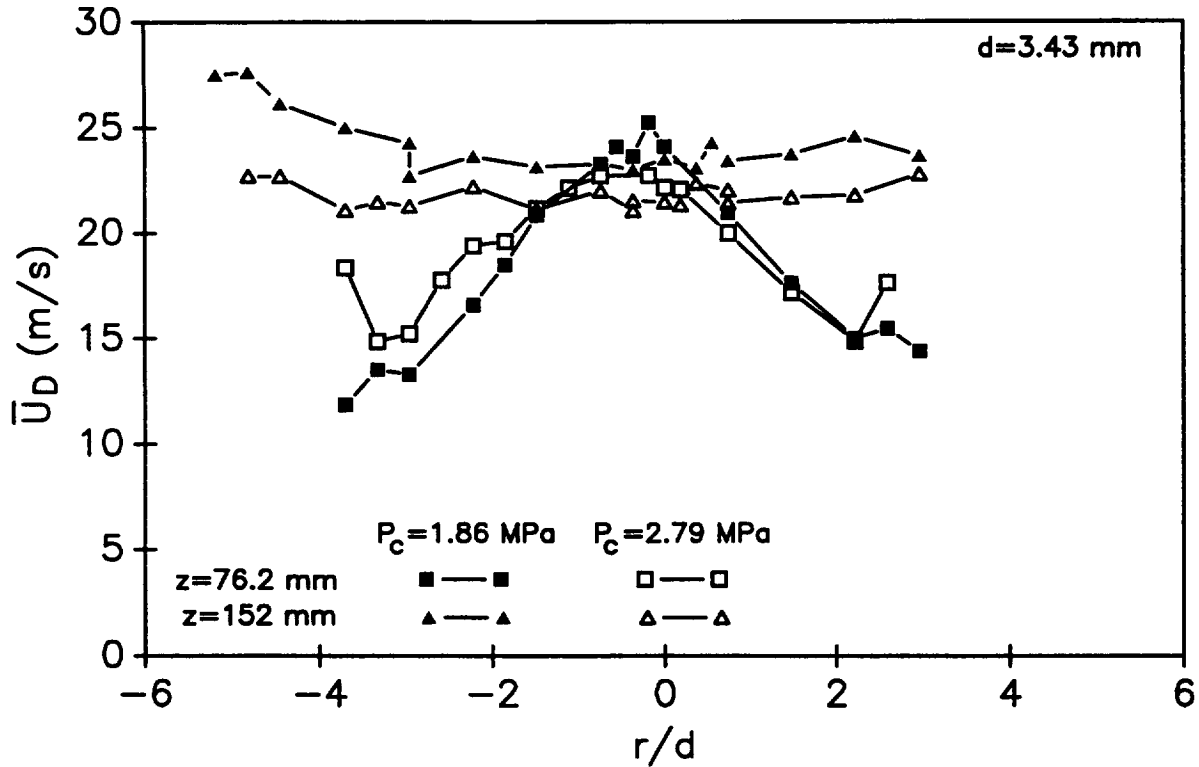


Fig. 6.5. Radial variation of mean drop velocity for test cases 1 and 2, Table 6.1. Axial measurement locations are indicated in the figure.

The drop size measurements depicted in Fig. 6.4 show that the measured Sauter mean diameter does not change significantly with radial location for a given flow condition. For both cases 1 and 2, larger drops are present at the further downstream location. This observation does not point towards drop coagulation; it suggests that the higher velocity of the co-flowing  $\text{GH}_2$  velocity near the injector face produces smaller drops. Further downstream, the  $\text{GH}_2$  velocity decelerates, thus producing larger drops. It is noted that the drop validation rate of the PDPA instrument was low in the center region of the flowfield, and improved with radial location. This suggests that the central region of the flowfield has large unatomized LOX structures that the instrument is incapable of measuring. Finally, in comparing the drop size measurements between the two chamber pressure cases, it is evident that the lower momentum ratio corresponding to the higher chamber pressure case contributes to a spray field with larger drop sizes.

The mean drop velocities plotted in Fig. 6.5 show that for both chamber pressure conditions, at the closer measurement location, the velocity peaks at the centerline and decreases

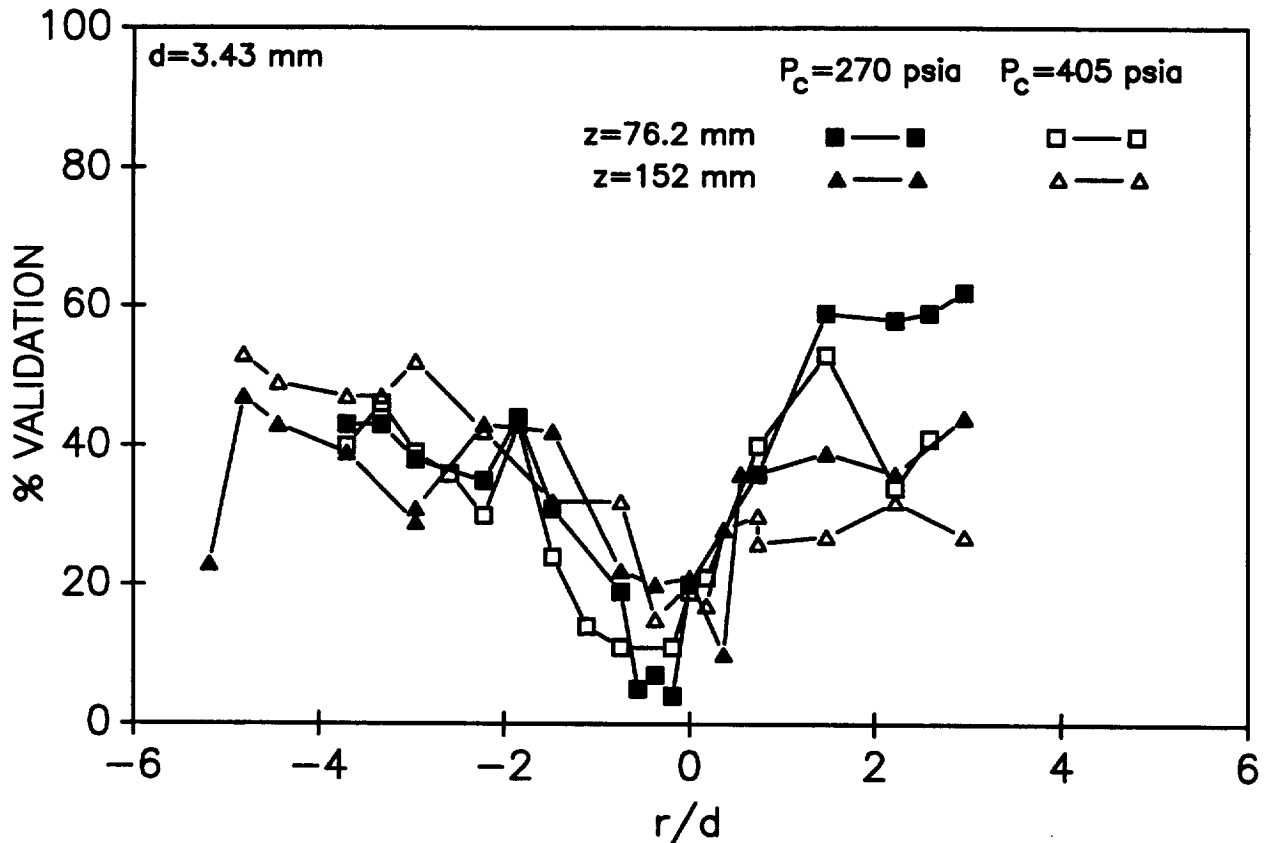
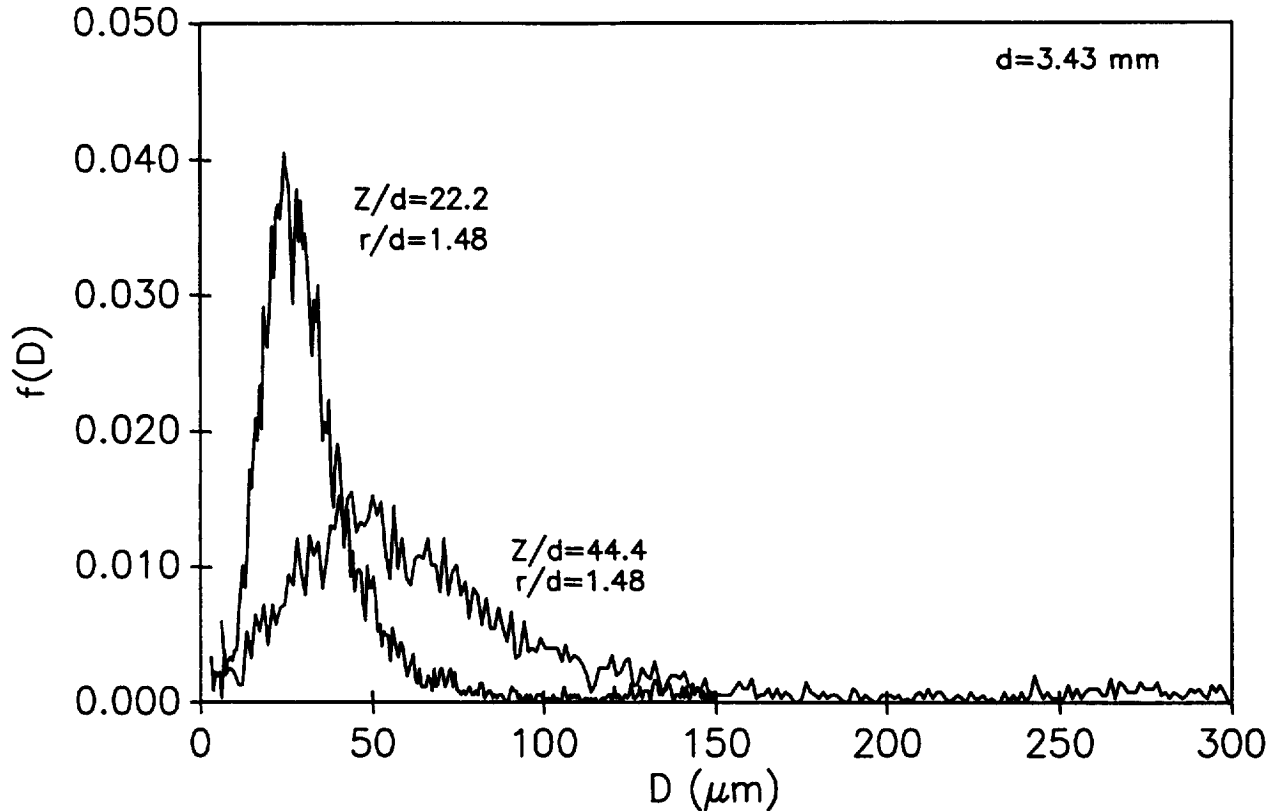


Fig. 6.6. Radial variation of percent validation for test cases 1 and 2, Table 6.1. Axial measurement locations are indicated in the figure.

with radial location. Further downstream, the mean drop velocity does not show significant radial variation. The mean velocity of only the small drops, presumably corresponding to the gas phase velocity, is slightly higher than the mean drop velocity shown in Fig. 6.5 but significantly lower than the calculated mean chamber velocity (see Table 6.1) suggesting that the combustion process is far from complete. Drop size and velocity measurements further downstream are necessary to completely document the evolving flowfield.

The corresponding percent validations for the measurements are plotted in a similar manner in Fig. 6.6. The percent validation number represents the percentage of drops that was accepted by the instrument as being spherical drops. The PDPA instrument rejects measurements based on drop asphericity, signal to noise limits and both velocity and size dynamic range limits. The results show that for all flow conditions and measurement locations, the percent validation is low in the center region of the flowfield. With radial distance from the centerline, the percent validation is seen to increase. This percent validation trend with radial distance is consistent with the observations noted from the qualitative Mie scattering results. In the center region of the



**Fig. 6.7. Probability density functions of LOX drop size at two measurement locations for test case 1, Table 6.1. Axial and radial measurement locations are indicated in the figure.**

flowfield, the LOX persists either as a contiguous jet or as a dense drop cloud that cannot be properly characterized by the drop measurement technique employed here. Away from the center region of the flowfield, the increase in percent validation indicates that here spherical LOX drops are present.

Further information is gained by inspecting the probability density functions (pdfs) of the drop size measurements. The drop size pdfs at an  $r/d$  of 1.48, (where the percent validation is relatively high) for the two axial measurement locations are contrasted in Fig. 6.7 for the flow conditions corresponding to Case 1, Table 6.1. The pdfs show that larger drops are present at the axial location further from the injector face. This does not suggest that the LOX drops coalesce with downstream distance. In contrast, it suggests that the LOX drops that breakup from the LOX core get bigger with axial distance. This phenomenon is thought to arise because the axial velocity of the high speed co-annular gaseous hydrogen flow decelerates rapidly with axial distance, and consequently, larger drops are present further from the injector face.

## 6.4 SUMMARY

Drop size and velocity were measured using phase Doppler interferometry in a uni-element (shear coaxial injector) rocket chamber under combusting conditions for the liquid oxygen (LOX)/gaseous hydrogen ( $\text{GH}_2$ ) propellant combination. These quantitative measurements are complemented by qualitative measurements of the LOX flow structure in the combusting flowfield. The drop size measurements showed low validation rates in the central part of the flowfield where Mie scattering images showed the presence of large un-atomized LOX structures. These two sets of measurements indicate that spherical drops do not represent the initial predominate structure for the atomizing liquid in the central part of the flowfield. This observation has potential important impacts regarding modeling of atomization processes for coaxial shear injector elements. Nevertheless, the present results point to the importance of studying atomization processes under hot-fire conditions if truly relevant understanding of spray phenomena under combusting conditions is to be achieved. The present study represents one of the few such studies and points to the need for more studies addressing both mechanistic and diagnostic issues raised by the present work.

## VII REFERENCES

- [1] Gordon, S. and McBride, B. J., "Computer Program for Calculation of Complex Chemical Equilibrium Compositions, Rocket Performance, Incident and Reflected Shocks, and Chapman-Jouguet Detonations," NASA SP-273 Interim Revision N78-17724, March, 1976.
- [2] Witze, P.O. and Baritaud, T. A., "Particle Seeding for Mie Scattering Measurements in Combusting Flows," Sandia Report SAND85-8912, 1986.
- [3] Eckbreth, A. C., Bonczyk, P. A. and Verdieck, J. F., "Combustion Diagnostics By Laser Raman and Fluorescence Techniques," *Prog. Energy Combust. Sci.*, 5, 1979, p. 253.
- [4] Eckbreth, A. C., Laser Diagnostics for Combustion Temperature and Species, Abacus Press, Tunbridge Wells, Kent and Cambridge, MA, 1988.
- [5] Allen, M. G., Parker, T. E., Reinecke, W. G., Legner, H. H., Foutter, R. R., Rawlins, W. T. and Davis, S. J., "Fluorescence Imaging of OH and NO in a Model Supersonic Combustor," *AIAA Journal*, Vol. 31, No. 3, March, 1993, pp. 505-512.
- [6] Seitzman, J. M., Üngüt, A., Paul, P. H. and Hanson, R. K., "Imaging and Characterization of OH Structures in a Turbulent Nonpremixed Flame," *Twenty-Third Symposium (International) on Combustion*, The Combustion Institute, Pittsburgh, PA, 1990, pp. 637-644.
- [7] Seitzman, J. M. and Hanson, R. K., "Comparison of Excitation Techniques for Quantitative Fluorescence Imaging of Reacting Flows," *AIAA Journal*, Vol. 31, No. 3, March, 1993, pp. 513-519.
- [8] Schlichting, H., Boundary Layer Theory, McGraw Hill Publishing Company, New York, New York, 1979.
- [9] Kennedy, I. M. and Kent, J. H., "Measurements of a Conserved Scalar in Turbulent Jet Diffusion Flames," *Seventeenth Symposium (International) on Combustion*, The Combustion Institute, Pittsburgh, PA, 1979, pp. 279-287.
- [10] Stárner, S. H. and Bilger, R. W., "Measurement of Scalar-Velocity Correlations in a Turbulent Diffusion Flame," *Eighteenth Symposium (International) on Combustion*, The Combustion Institute, Pittsburgh, PA, 1981, pp. 921-930.

- [11] Stårner, S. H. and Bilger, R. W., "Joint Measurements of Velocity and Scalars in a Turbulent Diffusion Flame with Moderate Swirl," *Twenty-First Symposium (International) on Combustion*, The Combustion Institute, Pittsburgh, PA, 1986, pp. 1569-1577.
- [12] Stepowski, D. and Cabot, G., "Laser Mie Scattering Measurements of Mean Mixture Fraction Density and Temperature by Conditional Seeding in a Turbulent Diffusion Flame," *Twenty-Second Symposium (International) on Combustion*, The Combustion Institute, Pittsburgh, PA, 1988, pp. 619-625.
- [13] Ebrahimi, I. and Kleine, R., "The Nozzle Fluid Concentration Fluctuation Field in Round Turbulent Free Jets and Jet Diffusion Flames," *Sixteenth Symposium (International) on Combustion*, The Combustion Institute, Pittsburgh, PA, 1976, pp. 1711-1723.
- [14] FLUENT Computer Program from Fluent Inc.
- [15] Moser, M. D., Merenich, J. J., Pal, S., and Santoro, R. J., "OH-Radical Imaging and Velocity Field Measurements in a Gaseous Hydrogen/Oxygen Rocket," AIAA 93-2036, *AIAA/SAE/ASME/ASEE 29th Joint Propulsion Conference and Exhibit*, Monterey, CA, June 28-30, 1993.
- [16] Stepowski, D., "Laser Measurements of Scalars in Turbulent Diffusion Flame," *Prog. Energy Combust. Sci.*, Vol. 18, 1992, pp. 463-491.
- [17] Foust, M. J., Deshpande, M., Pal, S., Ni, T., Merkle, C. L., and Santoro, R. J., "Experimental and Analytical Characterization of a Shear Coaxial Combusting  $\text{GO}_2/\text{GH}_2$  Flowfield," AIAA 96-0646, *34<sup>th</sup> Aerospace Sciences Meeting and Exhibit*, Reno, NV, January 15-18, 1996.
- [18] Calhoon, D., Ito, J. and Kors, D., "Investigation of gaseous Propellant Combustion and Associated Injector-Chamber Design Guidelines," Aerojet Liquid Rocket Company, NASA CR-121234, Contract NAS3-13379, July 1973.
- [19] Anon., Rocketdyne Interim Report "Advanced Engine Aerospike Experimental Program," Rockwell International, Rocketdyne Division, NASA Contract NAS8-20349, 1968.
- [20] Anon., Rocketdyne Final Report, " $\text{O}_2/\text{H}_2$  Advanced Manuevering Propulsion Technology Program," Rockwell International, Rocketdyne Division, Report No. AFRPL-TR-76-05, 1976.

- [21] Anon., Rocketdyne Final Report "Hydrogen/Oxygen APS Engines Program," Rockwell International, Rocketdyne Division, NASA CR-120805, 1973.
- [22] Foust, M., Pal, S., and Santoro, R. J., "Gaseous Propellant Rocket Studies Using Raman Spectroscopy," AIAA 96-2766, 32<sup>nd</sup> AIAA/ASME/SAE/ASEE Joint Propulsion Conference, Lake Buena Vista, FL, July 1-3, 1996.
- [23] Moser, M. D., Pal, S., and Santoro, R. J., "Laser Light Scattering Measurements in GO<sub>2</sub>/GH<sub>2</sub> Uni-Element Rocket Chamber," AIAA 95-0137, 33<sup>rd</sup> Aerospace Sciences Meeting and Exhibit, Reno, NV, January 9-1, 1995.
- [24] *Liquid Rocket Engine Injectors*, NASA SP-8089, 1976.
- [25] Hulka, J., Schneider, J. A. and Dexter, C. E., "Performance and Stability of a Booster Class LOX/H<sub>2</sub> Swirl Coaxial Element Injector," AIAA-91-1877, AIAA/SAE/ASME 27th Joint Propulsion Conference, Sacramento, CA, June 24-26, 1991.
- [26] Wu, P.-K. and Faeth, G. M., "Aerodynamic Effects on Primary Breakup of Turbulent Liquids," *Atomization and Sprays*, vol. 3, no. 3, pp. 265-289, 1993.
- [27] Wu, P.-K., Tseng, L.-K. and Faeth, G. M., "Primary Breakup in Gas/Liquid Mixing Layers for Turbulent Liquids," *Atomization and Sprays*, vol. 2, no. 3, pp. 295-317, 1992.
- [28] Sutton, R. D., Schuman, M. D. and Chadwick, W. D., Operating Manual for Coaxial Injection Combustion Model, NASA CR-129031, 1974.
- [29] Schuman, M. D. and Beshore, D. G., Standardized Distributed Energy Release (SDER) Computer Program Final Report, AFRPL-TR-78-7, 1978.
- [30] Muss, J. A., Nguyen, T. V. and Johnson, C. W., User's Manual for Rocket Combustor Interactive Design (ROCCID) and Analysis Computer Program, Volume 1 - User's Manual, NASA Contractor Report 1087109, May, 1991.
- [31] George, D. J., "Rocket Injector Hot Firing and Cold Flow Spray Fields," AIAA/SAE 9th Propulsion Conference, Las Vegas, NV, November 5-7, 1973.
- [32] George, D. J., "Droplet Size Distribution Functions for Rocket Combustor Spray Field," 11th JANNAF Combustion Meeting, Pasadena, CA, September 9-13, 1974.
- [33] Ingebo, R. D., Photomicrographic Tracking of Ethanol Drops in a Rocket Chamber Burning Ethanol and Liquid Oxygen, NASA TN D-290, 1960.

- [34] Bachalo, W. D. and Houser, M. J., "Phase/Doppler Spray Analyzer for Simultaneous Measurements of Drop Size and Velocity Distribution," *Optical Engineering*, vol. 23, pp. 583-590, 1984.
- [35] Ibrahim, K. M., Werthimer, G. D. and Bachalo, W. D., "Signal Processing Considerations for Laser Doppler and Phase Doppler Applications," *The Fifth International Symposium on the Application of Laser Techniques of Fluid Mechanics*, Lisbon, Portugal, July 9-12, 1990.
- [36] Liquid Particle Size Measurement Techniques, 2nd volume, E. D. Hirleman, W. D. Bachalo and P. G. Felton (eds.), ASTM, Philadelphia, 1990.
- [37] Vassallo, P. Ashgriz, N. and Boorady, F. A., "Effect of Flow Rate on the Spray Characteristics of Impinging Water Jets," *Journal of Propulsion and Power*, vol. 8, no. 5, pp. 980-986, Sept-Oct. 1992.
- [38] Zaller, M. M. and Klem, M. D., Coaxial Injector Spray Characterization Using Water/Air as Simulants, NASA-TM-105322, November, 1991.
- [39] Eroglu, H. Chigier, N. A., "Initial Drop Size and Velocity Distributions for Airblast Coaxial Atomisers," *Journal of Fluids Engineering*, vol. 113, pp. 453-459, 1991.
- [40] Hardalupas, Y., McDonald, H. and Whitelaw, J. H., Two Fluid Mixing, Advanced Earth-to-Orbit Propulsion Technology, NASA Conference Publication 3174, vol. II, 1992.
- [41] Goix, P. J. Cessou, A., Stepwoski D. and Edwards, C. F., "Structure of a Methanol/Air Coaxial Reacting Spray near the Stabilization Region by OH Fluorescence Imaging and Two-Component Phase-Doppler Interferometry," 1992 Spring Meeting of the Western States Section, The Combustion Institute, Oregon State University, March, 1992.
- [42] Ryan, H. M., Pal, S., Lee W. and Santoro, R. J., "Drop Distribution Effects on Planer Laser Imaging of Sprays," *Atomization and Sprays*, vol. 2, no. 2, pp. 155-177, 1992.
- [43] Handbook of Chemistry and Physics, R. C. Weast (ed.), 67th edition, 1986.

## VIII PUBLISHED PAPERS

- [1] Pal, S., Moser, M. D., Ryan, H. M., Foust, M. J. and Santoro, R. J., "Flowfield Characteristics in a Liquid Propellant Rocket," 29th AIAA/ASME/SAE/ASEE Joint Propulsion Conference and Exhibit, Paper No. AIAA 93-1882, Monterey, CA, June 28-30, 1993.
- [2] Moser, M. D., Merenich, J. J., Pal, S. and Santoro, R. J., "OH-Radical Imaging and Velocity Field Measurements in a Gaseous Hydrogen/Oxygen Rocket," 29th AIAA/ASME/SAE/ASEE Joint Propulsion Conference and Exhibit, Paper No. AIAA 93-2036, Monterey, CA, June 28-30, 1993.
- [3] Moser, M. D., Pal, S. and Santoro, R. J., "Uni-Element Rocket Studies," Conference on Advanced Earth-to-Orbit Propulsion Technology, Huntsville, AL, May 17-19, 1994.
- [4] Beisler, M., Pal, S., Moser, M. D. and Santoro, R. J., "Shear Coaxial Injector Atomization in a LOX/GH<sub>2</sub> Propellant Rocket," 30th AIAA/SAE/ASME/ASEE Joint Propulsion Conference and Exhibit, Indianapolis, Paper No. AIAA 94-2775, Indianapolis, IN, June 27-29, 1994.
- [5] Moser, M. D., Pal, S. and Santoro, R. J., "Laser Light Scattering Measurements in a GO<sub>2</sub>/GH<sub>2</sub> Uni-Element Rocket Chamber," 33rd AIAA AeroSpace Sciences Meeting, Paper No. AIAA 95-0137, Reno, NV, January 9-12, 1995.
- [6] Rahman, S. A., Pal, S. and Santoro, R. J., "Swirl Coaxial Atomization; Cold Flow and Hot-Fire Experiments," 33rd AIAA AeroSpace Sciences Meeting, Paper No. AIAA 95-0381, Reno, NV, January 9-12, 1995.
- [7] Haidn, O. J., Vogel, A., Mayer, W., Pal, S., Gökalp, I. and Chauveau, C., "Experimental Investigation of Liquid Propellant Spray Combustion," Liquid Rocket Combustion Devices: Proceedings of the Second International Symposium on Liquid Rocket Propulsion, ONERA-Chatillon, France, June 19-21, 1995.
- [8] Pal, S., Foust, M. J., Ni, T. and Santoro, R. J., "Uni-Element Studies of Gas/Gas Injectors for Rocket Combustors," JANNAF CS/PSH/EPTS/SPIRITS Joint Meeting, Huntsville, AL, October 23-27, 1995.

- [9] Foust, M. J., Deshpande, M., Pal, S., Ni, T., Merkle, C. L. and Santoro, R. J., "Experimental and Analytical Characterization of a Shear Coaxial Combusting  $\text{GO}_2/\text{GH}_2$  Flowfield," 34th Aerospace Science Meeting and Exhibit, Paper No. AIAA 96-0646, Reno NV, January 15-18, 1996.
- [10] Pal, S., Moser, M. D., Ryan, H. M., Foust, M. J. and Santoro, R. J., "Shear Coaxial Injector Atomization Phenomena for Combusting and Non-Combusting Conditions," Atomization and Sprays, vol. 6, 1996, pp. 227-244.
- [11] Foust, M. J., Pal, S. and Santoro, R. J., "Gaseous Propellant Rocket Studies using Raman Spectroscopy, " 32nd AIAA/SAE/ASME/ASEE Joint Propulsion Conference and Exhibit, Paper No. AIAA 96-2766, Lake Buena Vista FL, July 1-3, 1996.
- [12] Foust, M. J., Deshpande, M., Pal, S., Ni, T., Merkle, C. L. and Santoro, R. J., "Experimental and Analytical Characterization of a Shear Coaxial Combusting  $\text{GO}_2/\text{GH}_2$  Flowfield," accepted for publication in the Journal of Propulsion and Power.

## IX MEETINGS

- [1] Moser, M. D., Pal, S., Santoro, R. J. and Merkle, C. L., "An Experimental Study of Characteristic Combustion-Driven Flows for CFD Validation," Propulsion Engineering Research Center, Penn State, Fourth Annual Symposium, September 9-10, 1992, Marshall Space Flight Center, Huntsville, AL.
- [2] Pal, S., Moser, M. D., Ryan, H. M., Foust, M. J. and Santoro, R. J., "Drop Size Measurements in a LOX/GH<sub>2</sub> Propellant Rocket," Joint Technical Meeting, The Central and Eastern States Sections of the Combustion Institute, March 15-17, 1993, New Orleans, LA.
- [3] Pal, S., Moser, M. D., Ryan, H. M. and Santoro, R. J., "Flowfield Characterization in a LOX/GH<sub>2</sub> Propellant Rocket," Eleventh Workshop for Computational Fluid Dynamic Applications in Rocket Propulsion, April 20-22, 1993, Marshall Space Flight Center, Huntsville, AL.
- [4] Pal, S., Moser, M. D., Ryan, H. M., Foust, M. J. and Santoro, R. J., "Flowfield Characteristics in a Liquid Propellant Rocket," 29th AIAA/ASME/SAE/ASEE Joint Propulsion Conference and Exhibit, Monterey, CA, June 28-30, 1993.
- [5] Moser, M. D., Merenich, J. J., Pal, S. and Santoro, R. J., "OH-Radical Imaging and Velocity Field Measurements in a Gaseous Hydrogen/Oxygen Rocket," 29th AIAA/ASME/SAE/ASEE Joint Propulsion Conference and Exhibit, Monterey, CA, June 28-30, 1993.
- [6] Pal, S., Merenich, J. J., Moser, M. D. and Santoro, R. J., "An Experimental Study of Characteristic Combustion-Driven Flows for CFD Validation," Propulsion Engineering Research Center, Penn State, Fifth Annual Symposium, The Pennsylvania State University, September 8-9, 1993, University Park, PA.
- [7] Merenich, J. J., Pal, S., Moser, M. D. and Santoro, R. J., "Velocity Field Measurements in a Gaseous Hydrogen/Oxygen Rocket," Fall Technical Meeting, The Eastern States Section of the Combustion Institute, October 25-27, 1993, Princeton, NJ.
- [8] Moser, M. D., Pal, S. and Santoro, R. J., "Flowfield Characterization in a GO<sub>2</sub>/GH<sub>2</sub> Propellant Rocket," Twelfth Workshop for Computational Fluid Dynamic Applications in Rocket Propulsion, April 19-21, 1994, Marshall Space Flight Center, Huntsville, AL.

- [9] Moser, M. D, Pal, S. and Santoro, R. J., "Uni-Element Rocket Studies," Conference on Advanced Earth-to-Orbit Propulsion Technology, Huntsville, AL, May 17-19, 1994.
- [10] Beisler, M., Pal, S., Moser, M. D. and Santoro, R. J., "Shear Coaxial Injector Atomization in a LOX/GH<sub>2</sub> Propellant Rocket," 30th AIAA/SAE/ASME/ASEE Joint Propulsion Conference and Exhibit, Indianapolis, Indianapolis, IN, June 27-29, 1994.
- [11] Moser, M. D., Pal, S. and Santoro, R. J., "Density and Mixture Fraction Measurements in a GO<sub>2</sub>/GH<sub>2</sub> Uni-element Rocket Chamber," Propulsion Engineering Research Center, Penn State, Sixth Annual Symposium, September 13-14, 1994, NASA Lewis Research Center, Cleveland, OH.
- [12] Moser, M. D., Pal, S. and Santoro, R. J., "Laser Light Scattering Measurements in a GO<sub>2</sub>/GH<sub>2</sub> Uni-Element Rocket Chamber," 33rd AIAA AeroSpace Sciences Meeting, Reno, NV, January 9-12, 1995.
- [13] Rahman, S. A., Pal, S. and Santoro, R. J., "Swirl Coaxial Atomization; Cold Flow and Hot-Fire Experiments," 33rd AIAA AeroSpace Sciences Meeting, Reno, NV, January 9-12, 1995.
- [14] Haidn, O. J., Vogel, A., Mayer, W., Pal, S., Gökalp, I. and Chauveau, C., "Experimental Investigation of Liquid Propellant Spray Combustion," Liquid Rocket Combustion Devices: Second International Symposium on Liquid Rocket Propulsion, ONERA-Chatillon, France, June 19-21, 1995.
- [15] Pal, S., Foust, M. J., Ni, T. and Santoro, R. J., "Uni-Element Studies of Gas/Gas Injectors for Rocket Combustors," JANNAF CS/PSH/EPTS/SPIRITS Joint Meeting, Huntsville, AL, October 23-27, 1995.
- [16] Foust, M. J., Deshpande, M., Pal, S., Ni, T., Merkle, C. L. and Santoro, R. J., "Experimental and Analytical Characterization of a Shear Coaxial Combusting GO<sub>2</sub>/GH<sub>2</sub> Flowfield," 34th Aerospace Science Meeting and Exhibit, Reno NV, January 15-18, 1996.
- [17] Foust, M. J., Deshpande, M., Pal, S., Ni, T., Merkle, C. L. and Santoro, R. J., "Experimental and Analytical Characterization of a Shear Coaxial Combusting GO<sub>2</sub>/GH<sub>2</sub> Flowfield," Workshop for Fluid Dynamic Applications in Rocket Propulsion and Launch Vehicle Technology, April 23-25, 1996, Marshall Space Flight Center, Huntsville, AL.

- [18] Foust, M. J., Pal, S. and Santoro, R. J., "Gaseous Propellant Rocket Studies using Raman Spectroscopy, " 32nd AIAA/SAE/ASME/ASEE Joint Propulsion Conference and Exhibit, Lake Buena Vista FL, July 1-3, 1996.
- [19] Foust, M., Deshpande, M., Pal, S., Merkle, C. L. and Santoro, R. J., "Experimental and Analytical Characterization of Gas/Gas Injectors," Propulsion Engineering Research Center, Penn State, Eight Annual Symposium, The Pennsylvania State University, October 30-31, 1996, University Park, PA.

## **X PERSONNEL**

**Robert J. Santoro, Professor of Mechanical Engineering, Principal Investigator**

**Sibtosh Pal, Senior Research Associate, Department of Mechanical Engineering**

**Michael Foust, Ph.D. Degree Graduate Student, Department of Mechanical Engineering**

**Marlow Moser, Ph.D. Degree Graduate Student, Department of Mechanical Engineering**

**John Merenich, MS Degree Graduate Student, Department of Mechanical Engineering**

**Michele Beisler, MS Degree Graduate Student, Department of Mechanical Engineering**

**Larry Schaaf, Senior Research Technician, Department of Mechanical Engineering**

## XI AWARDS

### **Prof. Robert J. Santoro**

Group Achievement Award, Gas-Gas Injector Characterization Program Team, from National Aeronautics and Space Administration, July 8, 1996.

### **Dr. Sibtossh Pal**

Group Achievement Award, Gas-Gas Injector Characterization Program Team, from National Aeronautics and Space Administration, July 8, 1996.

### **Dr. Michael Foust**

Group Achievement Award, Gas-Gas Injector Characterization Program Team, from National Aeronautics and Space Administration, July 8, 1996.

### **Mr. Larry Schaaf**

Group Achievement Award, Gas-Gas Injector Characterization Program Team, from National Aeronautics and Space Administration, July 8, 1996.



# Report Documentation Page

1. Report No. NAS8-38862-2	2. Government Accession No.	3. Recipient's Catalog No.	
4. Title and Subtitle AN EXPERIMENTAL STUDY OF CHARACTERISTIC COMBUSTION-DRIVEN FLOW FOR CFD VALIDATION		5. Report Date 10/7/97	6. Performing Organization Code
		8. Performing Organization Report No.	
7. Author(s) R. J. Santoro		10. Work Unit No.	
		11. Contract or Grant No. NAS8-38862	
9. Performing Organization Name and Address The Pennsylvania State University Propulsion Engineering Research Center University Park, PA 16802		13. Type of Report and Period Covered FINAL TECHNICAL REPORT 4/16/91-9/30/96	
		14. Sponsoring Agency Code	
12. Sponsoring Agency Name and Address George C. Marshall Space Flight Center National Aeronautics and Space Administration Marshall Space Flight Center, AL 35812		15. Supplementary Notes	
16. Abstract A series of uni-element rocket injector studies were completed to provide benchmark quality data needed to validate computational fluid dynamic models. A shear coaxial injector geometry was selected as the primary injector for study using gaseous hydrogen/oxygen and gaseous hydrogen/liquid oxygen propellants. Emphasis was placed on the use of non-intrusive diagnostic techniques to characterize the flowfields inside an optically-accessible rocket chamber. Measurements of the velocity and species fields were obtained using laser velocimetry and Raman spectroscopy, respectively. Qualitative flame shape information was also obtained using laser-induced fluorescence excited from OH radicals and laser light scattering studies of aluminum oxide particle seeded combustions flows. The gaseous hydrogen/liquid oxygen propellant studies for the shear coaxial injector focused on breakup mechanisms associated with the liquid oxygen jet under sub-critical pressure conditions. Laser sheet illumination techniques were used to visualize the core region of the jet and a Phase Doppler Particle Analyzer was utilized for drop velocity, size and size distribution characterization. The results of these studies indicated that the shear coaxial geometry configuration was a relatively poor injector in terms of mixing. The oxygen core was observed to extend well downstream of the injector and a significant fraction of the mixing occurred in the near nozzle region where measurements were not possible to obtain. Detailed velocity and species measurements were obtained to allow CFD model validation and this set of benchmark data represents the most comprehensive data set available to date. As an extension of the investigation, a series of gas/gas injector studies were conducted in support of the X-33 Reusable Launch Vehicle program. A Gas/Gas Injector Technology team was formed consisting of the Marshall Space Flight Center, the NASA Lewis Research Center, Rocketdyne and Penn State. Injector geometries studied under this task included shear and swirl coaxial configurations as well as an impinging jet injector.			
17. Key Words (Suggested by Author(s)) CFD Validation, Optical Diagnostics, Rocket Chamber Measurements		18. Distribution Statement UNCLASSIFIED, UNLIMITED	
19. Security Classif. (of this report) UNCLASSIFIED, UNLIMITED	20. Security Classif. (of this page) UNCLASSIFIED, UNLIMITED	21. No. of pages 119	22. Price